# SINGLE PARTICLE STUDIES OF PULVERIZED COAL OXY-COMBUSTION

by

Ethan S. Hecht

A dissertation submitted to the faculty of
The University of Utah
in partial fulfillment of the requirements for the degree of

Doctor of Philosophy

Department of Chemical Engineering

The University of Utah

May 2013

Copyright © Ethan S. Hecht 2013

All Rights Reserved

# The University of Utah Graduate School

## STATEMENT OF DISSERTATION APPROVAL

The dissertation of **Ethan S. Hecht**

has been approved by the following supervisory committee members:

| | | |
|---|---|---|
| **JoAnn S. Lighty** | , Chair | **Jan 4, 2013** Date Approved |
| **Christopher R. Shaddix** | , Member | **Jan 4, 2013** Date Approved |
| **Jost O. Wendt** | , Member | **Jan 4, 2013** Date Approved |
| **Philip J. Smith** | , Member | **Jan 4, 2013** Date Approved |
| **James C. Sutherland** | , Member | **Jan 4, 2013** Date Approved |

and by **JoAnn S. Lighty**, Chair of the Department of **Chemical Engineering**

and by Donna M. White, Interim Dean of The Graduate School.

# ABSTRACT

Modeling and experimental studies of the oxy-combustion behavior of pulverized coal chars are detailed in this work. During oxy-combustion, nitrogen is separated from oxygen before the introduction of oxygen, recycled flue-gas, and fuel into a coal boiler. The nearly pure $CO_2$ effluent (after condensation of $H_2O$) can be captured through condensation, and then utilized or stored, preventing the climate changing impacts of this greenhouse gas. Although oxy-combustion has been considered and studied for over a decade, there are still misunderstood aspects of the science that this research aims to clarify through modeling and experimental studies.

First, a detailed model of a single char particle is presented. The detailed model is employed to assess the impact of $CO_2$ and steam gasification reactions on the oxy-combustion of coal chars. The detailed model indicates that gasification reactions reduce the predicted char particle temperature significantly. Lower temperatures reduce the radiant emission and rate of char oxidation, but the char carbon consumption rate actually increases by approximately 10%, since the gasification reactions are consuming carbon (in addition to the oxygen). Gasification reactions account for about 20% of the carbon consumption in low oxygen conditions, and about 30% of the carbon consumption under oxygen enriched conditions.

Secondly, typical pulverized coal char combustion modeling assumptions are described and two simplified models are compared to the detailed model. The single-film model, wherein gas-phase reactions are ignored yields accurate results, with particle temperature predictions accurate to within 270 K, and carbon consumption rate predictions accurate to within 16%.

Finally, an entrained flow reactor (EFR) was used to make measurements of single-particle temperatures under a wide range of conditions for three coal chars. The environments ranged from 24-60% $O_2$, 10-14% $H_2O$, with $N_2$ or $CO_2$ serving as the diluent. Collected chars were also analyzed for burnout and surface area. Kinetic parameters were found for the simplified model to fit the experimental data, for each of the coal chars,

over the wide range of environments studied. The model described herein and these kinetic parameters can be used in more complex CFD codes to accurately predict the oxy-combustion behavior of coal chars.

# CONTENTS

# LIST OF FIGURES

# LIST OF TABLES

# ACKNOWLEDGEMENTS

There are many people and organizations to whom I am grateful for their support. I would first like to thank my advisor, Prof. JoAnn Lighty, and Dr. Chris Shaddix, for realizing what a perfect candidate I was for this project, and seeing the potential for such a synergistic relationship between myself, the University of Utah, and Sandia National Labs. My time and tuition was funded through the Sandia National Laboratories Doctoral Studies program, and additional funding was provided by both the National Energy Technology Laboratory's Power Systems Advanced Research Program, managed by Dr. Robert Romanosky, through Sandia, and the University of Utah, Institute for Clean and Secure Energy Clean Coal program, as Award Number DE-NT0005015, managed by David Lang.

In addition to recommending and suggesting my work on this project, I also appreciate the guidance and scientific insights provided by Prof. JoAnn Lighty and Dr. Chris Shaddix, as well as my other committee members, Prof. Jost Wendt, Prof. Phil Smith, and Prof. James Sutherland. I am grateful to Stephanie 'Skipper' Coates and Cristina Jaramillo for performing many of the TGA experiments that I would not have had time to run on my own. Dana Overacker did a great job of keeping the labs at the U in order and supplies stocked.

Finally, I would like to thank my wife, Jennifer, for her emotional support and encouragement to pursue a Ph.D., even though it meant we had to spend time apart.

# CHAPTER 1

# INTRODUCTION

Coal is a heterogeneous rock of vegetable origin that contains large amounts of carbon (65-95%), some hydrogen, oxygen, sulfur, and nitrogen, along with mineral matter that remains as ash postcombustion. A contiguous layer of coal, or seam, will have a fairly uniform composition and the combustion kinetics can be characterized with limited error. Coals from different seams, however, can range widely in composition and combustion characteristics. Coals are classified by rank, which is an indication of reactivity. If one plots the atomic hydrogen to carbon ratio as a function of the atomic oxygen to carbon ratio on a Van Krevelen diagram, different groupings appear. A Van Krevelen diagram is shown in Fig. 1.1, with more ordered carbons, or higher rank coals on the bottom left of the chart, and less ordered carbons with larger amounts of oxygen and hydrogen towards the upper right corner of the chart. The highest rank coals are classified as anthracite, then bituminous, sub-bituminous and the lowest rank, lignite. As shown on the chart, biomass is of comparable rank to lignite coal. High rank coals contain and release the most energy during combustion, but are also more difficult to ignite and burn to completion.

*On Stones* by Theophrastus provides written evidence of lignite coal combustion by the Greeks as early as 200 BC [1]. Electric power generation from coal combustion on a commercial scale began with a plant built by Thomas Edison in 1882 [2]. Today, coal is still an abundant resource with 860 billion tons of proved recoverable reserves in the world in 2008, around 27% of which is in the United States [3]. In 2009, coal was responsible for about 27% of the world energy supply, almost 41% of the global electricity supply, but was also responsible for 43% of the world $CO_2$ emissions [4]. With the abundance and current usage of coal, it is likely to be an important part of energy generation for many years to come. Over the past few decades, climate change concerns have prompted the development of regulations and technologies to reduce carbon dioxide emissions.

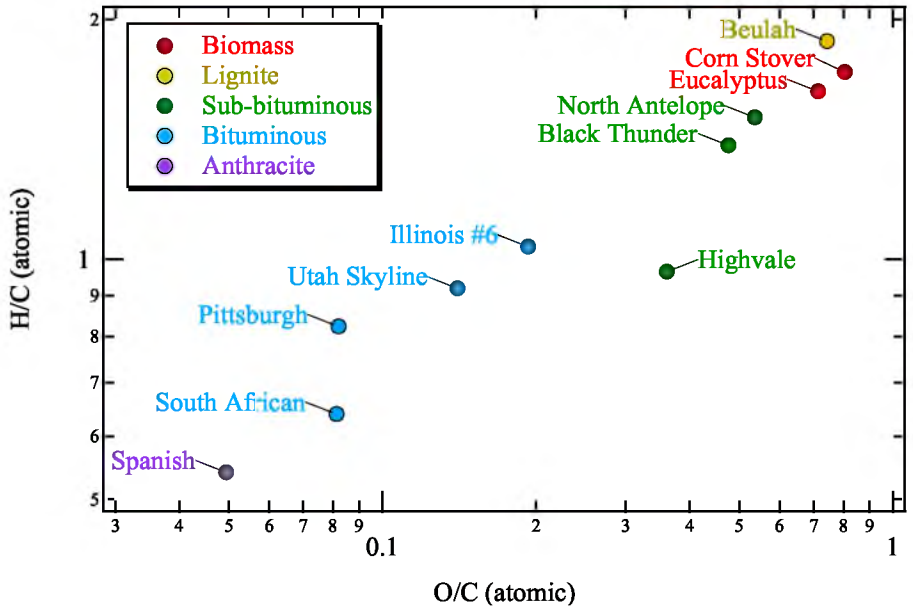


**Figure 1.1**. Van Krevelen diagram for biomass through anthracite coal. Labels are either the mine name, country of origin, or composition for biomass.

Coal combustion, accounting for such a large share of $CO_2$ emissions, will require cost-effective technology to capture this combustion product and make it available for utilization and/or storage as the regulations become more stringent. There are several strategies that allow $CO_2$ to be captured from coal combustion. The first is precombustion $CO_2$ capture. In the integrated gasification combined cycle (IGCC) system, the fuel is first gasified to syngas and then the water gas shift reaction converts the fuel to $H_2$, capturing the $CO_2$ along the way. The $H_2$ is then used as the fuel for a gas turbine. postcombustion capture is also possible. The second strategy for coal combustion while capturing $CO_2$ is amine stripping, which can be used to condense dilute $CO_2$ after conventional combustion. The third approach is oxy-combustion with flue-gas recirculation, where oxygen is separated from the air before combustion and then mixed with a portion of the flue-gas (primarily consisting of $CO_2$ and steam) before injection into a coal boiler. Flue-gas recirculation is required to moderate the combustion temperature and prevent excessive furnace slagging. This method generates a highly-concentrated $CO_2$ effluent that can be readily compressed and utilized or stored. Some research has found this to be a more efficient strategy than conventional combustion with tail-end $CO_2$ capture by amine stripping [5, 6]. While IGCC has the potential for slightly higher efficiencies and lower capital costs than newly-built oxy-combustion facilities with carbon capture, this technology is not available for retrofit on the extensive infrastructure that exists for conventional pulverized coal combustion. In

a recent review, Chen et al. [6] summarize studies on capital cost and generating efficiencies of different strategies of coal combustion with carbon capture. They find that oxy-fuel combustion is slightly more efficient than postcombustion capture and has a much lower capital cost as a retrofit technology. Pressurized oxy-combustion is estimated to offer even higher efficiencies than atmospheric pressure combustion [6, 7], but would be limited to newly built coal boilers.

In addition to the greater efficiency of oxy-combustion than conventional combustion with amine stripping, Chen et al. [6] also report that lower $NO_x$ emissions are attributed to less thermal and prompt $NO_x$ formation. Reduced $NO_x$ is attributed to the reduced partial pressure of $N_2$, the effect of $CO_2$ as a getter for radicals, and the reburning of NO as the flue-gas is recycled. Unfortunately, higher concentrations of $SO_x$ are also observed, due to lower volumes of total emissions, with the same volume of $SO_x$ as would be present in traditional combustion. Increased $SO_x$ could cause corrosion in the furnace. Increased CO emissions as compared to conventional combustion are also possible, due to $CO_2$ dissociation.

In this work, the combustion characteristics of pulverized coal particles are considered, with a characteristic dimension less than 200 $\mu$m. At the beginning of the combustion process, a coal particle is rapidly heated and moisture and loosely bound volatile components are released. These gas phase volatiles combust rapidly, producing bright emissions from the soot generated [8]. The heating rate and oxygen concentration, in addition to coal rank and composition affect both the amount of volatile matter released and the resulting char pore structure [9]. As the oxygen concentration increases (for a given diluent), the size of the soot cloud, the ignition delay, and the volatile combustion time decrease [8]. This work is not concerned with the kinetics or mechanisms of devolatilization.

The focus of this work is on the processes that occur after devolatilization, when the resulting porous carbon and ash, or char, particles continue to burn. Char combustion kinetics are much slower than gas phase combustion, and the burn-out characteristics are important in coal fired boiler design, so a high-quality ash that is a commodity rather than waste stream is generated [10]. Pulverized coal char combustion is not necessarily only limited by kinetics, but can also have mass-transfer limitations, both in the gas-phase and within the porous particle, making data analysis and modeling more complex. Coal combustion literature describes three different zones: Zone I is combustion when there are no mass-transfer limitations, with reactions occurring throughout the pores of the particle; Zone II is combustion when there are both mass-transfer and kinetic limitations; and Zone III is combustion where mass-transfer in the boundary layer limits the reaction rates, and

the combustion only occurs on the surface of the particle. Pulverized coal combustion typically occurs under Zone II conditions, requiring a description of boundary-layer mass-transfer, heterogeneous kinetics, and mass-transfer within the pores of the particle. Because pulverized coal particles are small, the slip velocity between the gas and particle is also small. The gas layer can be thought of as being stagnant with respect to the particles, and therefore one-dimensional, assuming that the particles are spherically symmetrical.

The kinetics of coal chars reacting with oxygen have been studied extensively [9, 11–13], but the reactions of chars with $CO_2$ and $H_2O$ are often neglected due to high activation energies and low concentrations of reactants (in the bulk gas). During oxy-combustion with flue-gas recycle, there are much higher concentrations of $CO_2$ in the bulk gas, and the potential for much higher concentrations of $H_2O$, depending on the extent to which the flue-gas is dried before recycle. Furthermore, different oxygen feed strategies during oxy-combustion may be necessary to achieve flame stability and since pure oxygen must be available for the oxy-combustion process, there is the potential to have higher concentrations of oxygen, either in the primary and secondary streams, or as oxygen lances in various locations in the coal burner. Exothermic oxidation reactions in regions with high oxygen concentrations will cause high coal char temperatures, overcoming high activation energies. Therefore, there is a much greater potential for gasification reactions to have an impact on coal combustion kinetics under oxy-fired conditions. There has been some speculation that the gasification reactions may enhance the char burning rate in oxy-fuel combustion [14–16]. In a previous study, our group at Sandia found that the overall consumption rate of a char particle reacting at a temperature near the gas temperature (i.e. at low $O_2$ concentration in the surrounding gas) is slightly increased by the $CO_2$ gasification reaction, but when the particle is reacting at a temperature considerably higher than the ambient gas temperature (i.e. an $O_2$-enriched environment), the $CO_2$ gasification reaction decreases the overall carbon removal rate, again by a small amount [17].

Under air-fired conditions, nearly 80% of the gas is $N_2$. Replacing $N_2$ with $CO_2$ and increased levels of steam under oxy-combustion conditions affects the gas-phase properties, as shown in Fig. 1.2. A reduction in burning rate of char particles is attributed to the lower rate of oxygen diffusion through $CO_2$ in the particle boundary layer [18–20]. Ignition delay and volatile combustion times are also found to increase slightly when $CO_2$ replaces $N_2$ [8, 20–22]. Flame stability problems are also reported due to the lower adiabatic flame temperature, flame propagation speed [23], and delayed ignition in $CO_2$. In addition, both $CO_2$ and $H_2O$ are radiantly active gas species, altering heat transfer between the particles

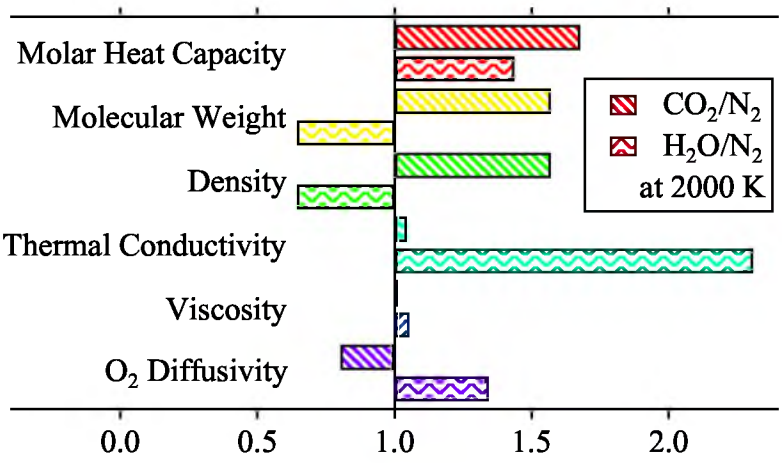


**Figure 1.2**. Ratio of $CO_2$ to $N_2$ properties at 2000 K.

and the boiler surfaces. Differences in density and viscosity between $CO_2$ and $N_2$ could also affect the coal delivery, which is conventionally carried by preheated air [6].

Differences on the combustion temperatures and burnout profiles in the presence of $CO_2$ (and to a lesser extent $H_2O$) rather than $N_2$ are discussed in the literature. Dhaneswar and Pisupati [24] report that for a given residence time, the presence of $CO_2$ as a diluent, rather than $N_2$, leads to a higher conversion for low rank coals, but a lower conversion for high rank coals. This is attributed to the higher reactivities and combustion temperatures of low ranked coals. Hu et al. [25] find that the presence of $CO_2$ rather than $N_2$ leads to a higher conversion, but the presence of both $H_2O$ and $CO_2$ rather than $N_2$ leads to a lower conversion. Brix et al. [26] find that under pure kinetic control, the burnout time in both $CO_2$ and $N_2$ diluents are roughly equal, but when mass transfer provides resistance, conversion occurs faster in the $N_2$ diluent.

Although modern computers have large memory capacities and fast processor speeds at low cost, it is still not possible to include full chemistry, resolve boundary-layer and intraparticle gas transport for millions of char particles in a flow field the size of a pulverized coal boiler. The range of length scales is too vast. Simplifications must be made in tracking particles and in domain discretization. The state-of-the-art large eddy simulation (LES) code ARCHES developed at the University of Utah uses a direct quadrature method of moments (DQMOM) [27] formulation to implement a population balance on reacting char particles. Mass-transfer coefficients and Arrhenius laws describing apparent char kinetics are used to calculate reaction times and temperatures. The aim of this work is to improve kinetic fits and the physical description currently provided by the single particle submodel

for char combustion to more accurately predict temperature and burnout profiles. The improved physical description of the combustion process will still require simplifications to allow efficient implementation in an LES code, such as eliminating the need to resolve the microscopic length scales in the boundary layer and within a particle, and reducing the chemistry complexity.

The research objective is to provide a validated single-particle combustion submodel for the ARCHES LES code. This submodel will need to include enough physics to describe the combustion of coal char in oxy- and air-fired environments, but make enough simplifications so that the LES performance is not limited. The work will be divided into three parts. First, detailed modeling of single particles with and without the $CO_2$ and $H_2O$ gasification reactions will highlight the impact of gasification reactions on the oxy-combustion of coal. Secondly, simplified models for single-particle combustion will be proposed and compared to the detailed model. This will elucidate the errors ascribed to the modeling simplifications, and allow for error estimation on the simplified models. Finally, a wide range of experiments designed to elucidate the significance of the gasification reactions and evaluate kinetic parameters will be presented. This work will focus on determining the kinetics of oxidation and gasification reactions. A validated submodel for single-particles will have broad appeal in the coal combustion community. It will be directly applicable to the ARCHES LES code, and will help alleviate shortcomings in in current experimental data analysis techniques. In the review by Chen et al. [6], fundamental research needs include the determining the oxy-combustion characteristics of different coal types, and the development of models for subprocesses designed specifically for oxy-combustion (as opposed to air combustion), which are directly addressed in this research. Results from this study will also help advance coal combustion science and improve the understanding of the coal combustion process.

# CHAPTER 2

# MODEL DESCRIPTION

## 2.1 SKIPPY Model Description

SKIPPY (Surface Kinetics in Porous Particles) is a code that describes a steady-state spherical, reacting porous particle and its reacting boundary layer. The spherical domain is assumed to be one-dimensional in the radial direction. The equations solved by SKIPPY are similar to those in the PREMIX code [29], but the code allows for additional heterogeneous reactions. The code also employs different boundary conditions than PREMIX and appropriately describes the gas transport in the pores of the particle. Homogeneous and heterogeneous reaction rates are calculated by subroutines from the CHEMKIN II [30] and SURFACE CHEMKIN [31] packages, respectively. Specific heat capacities and specific enthalpies are also computed with CHEMKIN II subroutines [30]; the TRANSPORT [32] package is used to calculate diffusion coefficients and thermal conductivities.

### 2.1.1 Governing Equations

Unlike a premixed flame, heterogeneous reactions can add mass to the gas phase, so conservation of mass requires

$$\frac{d\dot{m}}{dr} = \sum_{k=1}^{K_g} \dot{s}_k W_k \sigma_r A, \tag{2.1}$$

where $r$ is the radial spatial coordinate [m]; $\dot{m} = \rho u A$, the mass flow rate [kg/s]; $\rho$, the gas density [kg/m$^3$]; $u$, the mass-averaged velocity [m/s]; $\dot{s}_k$, the molar rate of production per unit area by surface reactions of the $k^{\text{th}}$ species [mol/m$^2$·s] (with $K_g$ gas-phase species); $W_k$,

---

Reprinted with permission from Ref. [28]. Coauthors: Christopher R. Shaddix, Manfred Geier, Alejandro Molina, and Brian S. Haynes.

the molar weight of the $k^{\text{th}}$ species [kg/mol]; $\sigma_r$, the specific surface area for heterogeneous reactions [$m^2/m^3$]; and $A = 4\pi r^2$, the area normal to the direction of the flow [$m^2$]. The perfect gas equation is used to calculate the gas density,

$$\rho = \frac{p\overline{W}}{RT}, \tag{2.2}$$

where $p$ is the pressure [Pa]; $R$, the universal gas constant [J/mol·K]; $T$, the temperature [K]; and $\overline{W}$, the mean molecular weight [kg/mol]. Heterogeneous reactions do not occur outside the particle; from a modeling point of view, one way of writing this is that the area available for surface reactions, $\sigma_r = 0$ for $r > r_p$ (where $r_p$ is the radius of the particle [m]). This reduces the continuity equation to $d\dot{m}/dr = 0$ for $r > r_p$.

Outside the particle ($r > r_p$), chemical reactions cause only small spatial variations in the mass-averaged velocity that are, for that reason, neglected in the momentum balance. Within the porous particle, Darcy's Law (or the Hagen-Poiseuille equation, corrected for the nonlinear flow path) is used to describe the flow. The momentum equation is thus given by

$$\frac{dp}{dr} = -\frac{\dot{m}}{\rho A}\frac{8\mu}{r_{pore}^2}\frac{\tau}{\phi} \tag{2.3}$$

where $\mu$ is the mixture averaged viscosity [Pa·s]; $\phi$, the porosity, or void fraction; $\tau$, the tortuosity; and $r_{pore}$, the average pore radius [m]. Outside the porous particle ($r > r_p$), the tortuosity is zero, reducing the momentum balance to $dp/dr = 0$.

Changes in the gas-phase mass fractions, $Y_k$, are caused by convection, diffusion, heterogeneous reactions (for $r \leq r_p$), and homogeneous reactions. The equation of species mass conservation is

$$\frac{1}{A}\frac{d}{dr}(\dot{m} + \rho V_k A)Y_k = \dot{s}_k W_k \sigma_r + \dot{\omega}_k W_k \phi, \quad \text{for } k = 1, ..., K_g, \tag{2.4}$$

where $V_k$ is the diffusion velocity of the $k^{\text{th}}$ species [m/s], and $\dot{\omega}_k$ is the molar rate of production per unit volume by gas-phase reactions of the $k^{\text{th}}$ species [$mol/m^3 \cdot s$]. Note that this equation is valid throughout the entire spatial domain as outside the porous particle ($r > r_p$), $\sigma_r$ equals 0 and the void fraction, $\phi$ equals 1.

A multicomponent description of diffusion is used by SKIPPY to calculate the diffusion velocities. The Fickian diffusion coefficients are required, calculated by inverting the $[\beta]$ matrix where

$$\begin{aligned} \beta_{ii} &= \frac{x_i}{\mathcal{D}_{iK_g}} + \sum_{\substack{k=1 \\ i \neq k}}^{K_g} \frac{Y_k}{\mathcal{D}_{ik}}, \\ \beta_{ij} &= \frac{x_i}{\mathcal{D}_{iK_g}} - \frac{Y_i}{\mathcal{D}_{ij}}, \end{aligned} \qquad \text{for } i, j = 1, ..., K_g - 1 \tag{2.5}$$

where $x_i$ is the mole fraction of species $i$ and $\mathcal{D}_{ij}$ is the binary diffusion coefficient between species $i$ and species $j$, [m$^2$/s]. Within the pores of the particle ($r \leq r_p$), the Fickian diffusion coefficients, $[D] = [\beta]^{-1}$ are corrected for the nonlinear path of pore diffusion by the ratio of the void fraction to tortuosity: $D_{ij,r<r_p} = D_{ij}\phi/\tau$. The diffusion velocity of each species can then be calculated (in the entire domain) as

$$V_k = -\frac{W_k}{W}\sum_{i=1}^{K_g-1} D_{ik}\frac{dx_i}{dr}, \quad \text{for } k = 1, ..., K_g - 1, \tag{2.6}$$

$$V_{K_g} = -\sum_{k=1}^{Kg-1} V_k. \tag{2.7}$$

A thermal energy balance (neglecting gas radiation) yields

$$\frac{1}{A}\frac{d}{dr}\sum_{k=1}^{K_g}(\dot{m} + \rho V_k A)Y_k h_k + \frac{1}{A}\frac{d}{dr}\left(-\lambda_t A\frac{dT}{dr}\right) = \sum_{k=K_s^f}^{K_b^l} \dot{s}_k h_k W_k \sigma_r, \tag{2.8}$$

where $h_k$ is the specific enthalpy of the $k^{\text{th}}$ species [J/kg]; $\lambda_t = \lambda\phi + \lambda_p(1-\phi)$, the total thermal conductivity [W/m·K]; $\lambda$, the mixture-averaged gas thermal conductivity [W/m·K]; $\lambda_p$, the thermal conductivity of the solid particle [W/m·K]; $K_s^f$, the first surface species; and $K_b^l$, the last bulk species. Note that the source term on the right-hand side of the equation contains only the surface and bulk species. The enthalpy flow term on the left-hand side of the equation accounts for gas-phase and heterogeneous reactions of the gaseous species; the additional source term on the right-hand side of the equation accounts for the release of energy as solid species are converted to gas, and bulk species to surface species.

As the code produces a steady-state solution, the net-production rate of surface species must be zero, i.e.

$$\dot{s}_k = 0, \quad \text{for } k = K_s^f, ..., K_s^l, \tag{2.9}$$

where $K_s^l$ is the last surface species.

### 2.1.2 Discretization and Boundary Conditions

A finite volume approach is taken to represent and solve the system of coupled differential equations that describe the reacting particle and boundary layer. This results in a system of algebraic equations that are solved using the hybrid damped Newton's method and

time-marching scheme described in the next section. As an example, conservation of mass (Eq. 2.1) is written as

$$\frac{\dot{m}_{j+1} - \dot{m}_{j-1}}{2} = \sum_{k=1}^{K_g} \dot{s}_{k,j} W_k \sigma_r \frac{4}{3}\pi \left[ \left( \frac{r_j + r_{j+1}}{2} \right)^3 - \left( \frac{r_{j-1} + r_j}{2} \right)^3 \right], \tag{2.10}$$

where the subscript $j$ is a reference to a discrete point. At the particle surface, radiation to the surroundings must be included in the energy balance. The discretized energy balance at the particle surface (Eq. 2.8), with the additional radiation term included, is

$$\left( \sum_{k=1}^{K_g} (\dot{m} + \rho V_k A) Y_k h_k \right)_{j_p} - \left( \sum_{k=1}^{K_g} (\dot{m} + \rho V_k A) Y_k h_k \right)_{j_p - 1}$$
$$- \lambda_{j_p} 4\pi \left( \frac{r_{j_p-1} + r_p}{2} \right)^2 \frac{T_{j_p+1} - T_{j_p}}{r_{j_p+1} - r_p} + \lambda_{t,j_p-1} 4\pi \left( \frac{r_p + r_{j_p+1}}{2} \right)^2 \frac{T_{j_p} - T_{j_p-1}}{r_p - r_{j_p-1}}$$
$$+ \epsilon\sigma 4\pi r_p^2 (T_{j_p}^4 - T_w^4) = \sum_{k=K_s^f}^{K_b^l} \dot{s}_{k,j_p} h_{k,j_p} W_k A_{rxn}, \tag{2.11}$$

where $\epsilon$ is the emissivity of the reacting particle; $\sigma$, the Stefan-Boltzmann constant [W/m$^2$·K$^4$]; $T_w$ is the temperature of the wall, or surface to which the particle is radiating [K]; the index $j_p$ marks the location where $r = r_p$; and the surface area available for reaction is given by

$$A_{rxn} = \sigma_r \frac{4\pi}{3} \left[ r_p^3 - \left( \frac{r_{j_p-1} + r_p}{2} \right)^3 \right] + (1 - \phi) 4\pi r_p^2. \tag{2.12}$$

At a large radius, the temperature, pressure, and species mass fractions are specified as those of the bulk gas, and there are no gradients in mass flow. Care must be taken by the user to define a radius that is large enough that gradients in all of the dependent variables at the infinite boundary are sufficiently small to ensure that the boundary layer is not constrained by the extent of the domain. In general, a domain radius 100 times the particle radius is sufficient for the simulation of reacting pulverized coal particles. Alternatively, if one wants to constrain the size of the boundary layer, for example to reflect the imposition of turbulent mixing of the surrounding flow, then the chemical composition of the bounding flow needs to be carefully chosen to reflect the influence of combustion intermediates (such as CO and NO) that are being produced by heterogeneous reactions and diffusing through the boundary layer. Equations 2.4 and 2.8 are second-order equations (the second derivative in the species balance is tied into the diffusion velocity calculation), and additional constraints for this boundary-value problem must be specified. At $r = 0$, symmetry dictates that gradients in the dependent variables vanish, and there is zero mass flow at this location.

### 2.1.3 Solution Procedure

The solution is found using the two-point boundary-value solver, TWOPNT, described by Grcar [33], which is a hybrid damped Newton's method and time-marching scheme. TWOPNT uses Newton's algorithm to attempt convergence of the steady-state problem. If Newton's method begins to stray from the bounds of the problem (e.g. mass fractions outside the bounds $0 \leq Y_k \leq 1$, or negative temperatures), a time-marching scheme is executed to attempt to bring the solution back into the domain (the final solution is not affected by this time-marching scheme–it is only an approach to aid the numerical solution procedure). This requires unsteady forms of the governing equations. For example, the unsteady form of Eq. 2.4 is

$$\rho\frac{\partial Y_k}{\partial t} + \frac{1}{A}\frac{\partial}{\partial r}(\dot{m} + \rho V_k A)Y_k = \dot{s}_k W_k \sigma_r + \dot{\omega}_k W_k \phi \quad \text{for } k = 1, ..., K_g, \tag{2.13}$$

with the time differential approximated as

$$\rho\frac{\partial Y_k}{\partial t} \approx \rho_j^{n+1}\frac{Y_{k,j}^{n+1} - Y_{k,j}^{n}}{h}, \tag{2.14}$$

where the superscript $n$ indicates the time level and $h$ is the time step [s], specified by the user. All other terms are discretized in the spatial coordinate as discussed previously and evaluated at time $n+1$. The backward Euler method is used to solve these coupled equations, and the solution marches forward in time a number of steps specified by the user. Further details regarding this solution procedure are provided by Kee et al. [29].

Convergence is defined when the Newton correction step, $\Delta\Phi$, satisfies the following relation:

$$|\Delta\Phi| \leq \max(A, R\Phi). \tag{2.15}$$

In this equation, $\Phi$ is the solution vector, $[\dot{m}_1, T_1, p_1, Y_{1,1}, ..., Y_{K_g,1}, ..., \dot{m}_j, T_j, p_j, Y_{1,j}, ..., Y_{K_g,j}, ..., \dot{m}_J, T_J, p_J, Y_{1,J}, ..., Y_{K_g,J}]$, (with point 1 located where $r = 0$ and point $J$ at the "right" boundary, or largest domain radius); $A$ and $R$ are the absolute and relative tolerances specified by the user.

The TWOPNT solver also includes a provision for mesh refinement, and data points are added when one of three criterion are met:

1. the magnitude of a component's change exceeds some fraction ($\delta$) of the component's global change:

$$|\Phi_{n,j} - \Phi_{n,j-1}| > \delta\left(\max\Phi_n - \min\Phi_n\right), \tag{2.16}$$

2. the magnitude of change in a derivative exceeds a fraction ($\gamma$) of the global change:

$$\frac{\left|\frac{\Phi_{n,j+1}-\Phi_{n,j}}{r_{j+1}-r_j}-\frac{\Phi_{n,j}-\Phi_{n,j-1}}{r_j-r_{j-1}}\right|}{\max\left(\frac{\Phi_{n,j+1}-\Phi_{n,j}}{r_{j+1}-r_j}\right)-\min\left(\frac{\Phi_{n,j+1}-\Phi_{n,j}}{r_{j+1}-r_j}\right)}>\gamma,, \tag{2.17}$$

3. the magnitude of change in a component exceeds a fraction ($\alpha$) of the magnitude of that component:

$$|\Phi_{n,j}-\Phi_{n,j-1}|>\alpha\,|\Phi_{n,j}|\,. \tag{2.18}$$

At the edge of the particle ($r = r_p$), there are physical reasons for a discontinuity in the slope of the dependent variables. The refinement criteria given by Eq. 2.17 is ignored when $j = j_p$ to prevent continual mesh refinement at this point.

# CHAPTER 3

# EFFECT OF $CO_2$ AND STEAM GASIFICATION REACTIONS ON THE OXY-COMBUSTION OF PULVERIZED COAL CHAR

## 3.1 Abstract

For oxy-combustion with flue gas recirculation, elevated levels of $CO_2$ and steam affect the heat capacity of the gas, radiant transport, and other gas transport properties. A topic of widespread speculation has concerned the effect of gasification reactions of coal char on the char burning rate. To asses the impact of these reactions on the oxy-fuel combustion of pulverized coal char, we computed the char consumption characteristics for a range of $CO_2$ and $H_2O$ reaction rate coefficients for a 100 $\mu$m coal char particle reacting in environments of varying $O_2$, $H_2O$, and $CO_2$ concentrations using the kinetics code SKIPPY (Surface Kinetics in Porous Particles). Results indicate that gasification reactions reduce the char particle temperature significantly (because of the reaction endothermicity) and thereby reduce the rate of char oxidation and the radiant emission from burning char particles. However, the overall effect of the combined steam and $CO_2$ gasification reactions is to increase the carbon consumption rate by approximately 10% in typical oxy-fuel combustion environments. The gasification reactions have a greater influence on char combustion in oxygen-enriched environments, due to the higher char combustion temperature under these conditions. In addition, the gasification reactions have increasing influence as the gas temperature increases (for a given $O_2$ concentration) and as the particle size increases.

---

Reprinted with permission from Ref. [28]. Coauthors: Christopher R. Shaddix, Manfred Geier, Alejandro Molina, and Brian S. Haynes.

Gasification reactions account for roughly 20% of the carbon consumption in low oxygen conditions, and for about 30% under oxygen-enriched conditions. An increase in the carbon consumption rate and a decrease in particle temperature are also evident under conventional air-blown combustion conditions when the gasification reactions are included in the model.

## 3.2 Introduction

Coal combustion accounts for over 40% of the global electricity supply [34] and is likely to continue to be used for stationary power generation well into the future. As the international community considers enacting carbon dioxide emissions regulations, the development of cost-effective technologies to capture $CO_2$ is becoming increasingly important, particularly for the coal combustion processes (which also accounts for over 40% of the worldwide energy-related $CO_2$ emissions [35]). One promising method for carbon capture while producing electricity is oxy-combustion of coal [5]. In this approach, oxygen is separated from air before combustion and then mixed with a portion of the flue gas (primarily consisting of $CO_2$ and steam) before injection into a coal boiler. Flue gas recirculation is required to moderate the combustion temperature and prevent excessive furnace slagging. The flue gas from this process is rich in $CO_2$ and can be readily compressed and transported for utilization or storage once the moisture has been removed. With flue gas recirculation, the $CO_2$ levels in the furnace gases are much higher in oxy-fuel combustion (reaching 60-70 vol-%) than in conventional, air-fired combustion. In principle, flue gas recycling may occur before or after moisture removal, but commercial applications of oxy-fuel combustion will most likely utilize at least some wet flue gas recycling [36], leading to water vapor levels of up to 25–35 vol-% in postflame furnace gases. In order to implement this technology efficiently, the coal combustion characteristics in these environments, which are different than conventional air-fired environments, must be understood.

Various aspects of the coal combustion process have been found to be different in oxy-combustion environments, which can be partially attributed to the differences in the gas-phase properties (e.g. heat capacity and radiant characteristics) between an oxy-combustion environment and an air-fired environment. For instance, the rate of coal volatile consumption is reduced and coal ignition is delayed in environments containing high concentrations of $CO_2$, for a given furnace temperature and oxygen concentration [8, 20–22]. The burning rate of char particles is reduced due to the lower rate of oxygen diffusion through $CO_2$ in the particle boundary layer [18–20]. In addition to these well-established

effects, there has been speculation that the gasification reactions may enhance the char burning rate in oxy-fuel combustion [14–16]. While long considered too slow to compete with the oxidation reactions under air-fired combustion conditions, the gasification reactions may contribute to the overall consumption of the char because of the higher concentrations of $CO_2$ and $H_2O$ in an oxy-fired boiler.

By directly reacting with the solid carbon, one might expect the gasification reactions to increase the consumption of the char. However, the gasification reactions are strongly endothermic, requiring 172 kJ per mole of solid carbon when the reaction occurs with $CO_2$ and 131 $kJ/mol_C$ for reaction with steam. Therefore, the occurrence of these reactions lowers the char particle temperature, which in turn reduces the rate of oxidation. We previously studied the consequences of including the gasification reaction of $CO_2$ with solid carbon [17]. We found that the overall consumption rate of a char particle reacting at a temperature near the gas temperature (i.e. at low $O_2$ concentration in the surrounding gas) is slightly increased by the $CO_2$ gasification reaction. Alternatively, when the particle is reacting at a temperature considerably higher than the ambient gas temperature (i.e. in an $O_2$-enriched environment), the $CO_2$ gasification reaction decreases the overall carbon removal rate, though by a small amount [17]. In either case, the $CO_2$ gasification reaction was shown to substantially reduce the char particle combustion temperature. In the work reported here, the combined effects of both $CO_2$ and steam gasification reactions on the overall char consumption characteristics are evaluated.

## 3.3 Gasification Rates at 1 atm

The gasification rates of different carbonaceous materials with $CO_2$ or steam as gasifying agents have been studied extensively, primarily at low and intermediate temperatures, using thermogravimetric analyzers (TGAs) [37–39]. Although the actual mechanism of these two reactions and the types of carbon sites the reactants can access is still the subject of some debate, the gasification processes under atmospheric pressure are generally assumed to follow the global reaction scheme [37, 40–42]:

$$CO_2 + C_s \underset{k_{1,r}}{\overset{k_{1,f}}{\rightleftharpoons}} C(O)_s + CO \tag{3.1}$$

$$H_2O + C_s \underset{k_{2,r}}{\overset{k_{2,f}}{\rightleftharpoons}} C(O)_s + H_2 \tag{3.2}$$

$$C(O)_s + C_b \xrightarrow{k_3} CO + C_s \tag{3.3}$$

where the subscript s denotes a surface species that is available to react heterogeneously, $C_b$ is bulk carbon below the reacting mono-layer, and $k$ is the reaction rate coefficient in the direction specified by the arrow. Assuming a first-order concentration dependence, the overall rate of $CO_2$ gasification (described by reactions 3.1 and 3.3, in mol/m$^2$·s) follows a Langmuir-Hinshelwood kinetic expression, according to Eq. 3.4 [37, 40, 41]:

$$r = \frac{k_{1,f} p_{CO_2} [C_t]}{1 + \frac{k_{1,f}}{k_3} p_{CO_2} + \frac{k_{1,r}}{k_3} p_{CO}}, \tag{3.4}$$

where $[C_t]$ refers to the total concentration of surface active sites and $p$ is the partial pressure. Eq. 3.5 is a similar expression that describes the rate of steam gasification [37, 40, 42]:

$$r = \frac{k_{2,f} p_{H_2O} [C_t]}{1 + \frac{k_{2,f}}{k_3} p_{H_2O} + \frac{k_{2,r}}{k_3} p_{H_2}}. \tag{3.5}$$

The kinetic rate coefficients for reactions 3.1–3.3 are likely well-represented by an Arrhenius law, but the associated parameters are not well-established. It is widely recognized that the overall activation energies for the char gasification reactions are substantially greater than the $\sim$ 160 kJ/mol activation energy for reaction of coal chars with $O_2$ [9]. Laurendeau [37] reviewed the major studies of atmospheric pressure char gasification before 1978 and concluded that the effective activation energy was between 230–270 kJ/mol for gasification by $CO_2$ and between 190–270 kJ/mol for gasification by $H_2O$.

The overall kinetic rate of char gasification (or oxidation) is highly dependent on the char source and thermal history, as emphasized by Radovic et al. [43], and as explicitly recognized via the proportionality of overall rate to active site concentration, as expressed in Eqs. 3.4 and 3.5. Because of this, the best option for estimating the gasification rate coefficient when char oxidation is also important is to use rate coefficients of $CO_2$ and steam gasification relative to the rate coefficient for oxidation, for a given char. Then, when using a given kinetic expression to describe the char oxidation process, appropriate expressions for the $CO_2$ and steam gasification rate coefficients can be readily derived. Note, however, that this approach necessarily ignores the further subtlety represented by possible differences in the intrinsic reaction order of the overall gasification and oxidation rates. In light of the uncertainties in the kinetics parameters, this omission will only have a minor effect on the conclusions presented in this study.

Several studies in the literature have determined the relative kinetic rate coefficients of gasification by $CO_2$ and $H_2O$ to oxidation by $O_2$, primarily at 800 °C [40, 44–49]. From these measurements, one can reasonably bound the rate coefficient of the $CO_2$ gasification reaction relative to that of oxidation as falling between 1.0–20 $\times$ $10^{-5}$, at 800 °C, with a best-guess

of $6.2 \times 10^{-5}$, as summarized in ref. [17]. For steam gasification, several measurements of rate coefficients relative to oxidation have been reported, as shown in Table 3.1.

From these measurements, one can reasonably bound the relative rate coefficient of steam gasification of coal chars to be from $1.0–10 \times 10^{-4}$ at 800 °C (the Harris and Smith petcoke and Mann et al. results appear to be outliers). Liu et al. [50] recently compared the steam gasification rate of three different coal chars relative to gasification in $CO_2$. For all of the coal chars, the steam rate exceeded the $CO_2$ rate by a factor of 2–3 over the temperature range of 1400–1800 K. This agrees in magnitude with the rate coefficients shown in Table 3.1 relative to the rate coefficients for gasification by $CO_2$. On this basis, our best-guess relative rate coefficient of steam gasification is $2.0 \times 10^{-4}$ at 800 °C, a value that is about three times higher than our best-guess relative rate coefficient of $CO_2$ gasification.

## 3.4 Model Description

Char particle simulations were performed using SKIPPY (Surface Kinetics in Porous Particles), a computer program developed at the University of Sydney. The details of this FORTRAN program are included in 2.1. Briefly, SKIPPY solves the steady-state mass, species, and energy conservation equations for a reacting porous particle and its reacting boundary layer. From this solution, SKIPPY predicts species concentrations and temperatures within the pores of the char, at the outer surface of the char, and within the boundary layer surrounding the char. Both heterogeneous (gas-solid) and gas-phase chemical reactions are considered. The model assumes:

- a single, spherical particle in an unconstrained and unperturbed boundary-layer
- steady-state
- a 1-dimensional (radial) domain

**Table 3.1**. Ratio of Steam Gasification to Oxidation at 800 °C

| Source | Carbon Type | Relative Rate Coefficient |
|---|---|---|
| Degroot and Richards, 1989 [46] | cellulose char | $1.1 \times 10^{-3}$ |
| Harris and Smith, 1991 [47] | pet coke | $2.2 \times 10^{-6}$ |
| | lignite | $2.0 \times 10^{-4}$ |
| Roberts and Harris, 2000 [48] | hv bituminous | $2.3 \times 10^{-4}$ |
| | semi-anthracite | $1.3 \times 10^{-4}$ |
| Mann et al., 2004 [49] | lignite char | $4.5 \times 10^{-7}$ |

- gases are radiantly inactive over this spatial scale
- homogeneous and heterogeneous reactions proceed according to the law of mass action, the formalism is described by Kee et al. [51]

GRI-MECH 3.0 [52] was used to describe the gas-phase reaction kinetics, while the heterogeneous char reaction kinetics were described using the mechanism specified in Table 3.2. This surface mechanism is the same as that applied previously by Molina et al. [53, 54] with the addition of two steps describing the char gasification reactions with $CO_2$ and steam. Oxidation and gasification reactions are treated as adsorption-limited, with arbitrarily fast desorption reaction rates that guarantee insignificant accumulation of oxygen complexes on the surface of the char.

While it is understood that the gasification reactions should be written as multistep processes with reverse reaction contributions from $H_2$ and CO reacting with the oxygen-bound surface sites, our lack of knowledge of the relevant intrinsic reaction rates makes it necessary to use overall gasification steps with rate coefficients based on best estimates of activation energy and relative rate coefficients. This simplification is at least partly justified under the conditions investigated here because any $H_2$ that is produced from steam gasification reacts rapidly with oxygen and oxidizing radicals in the high-temperature boundary layers, and the reverse reaction of CO with surface oxides has a low activation energy and becomes increasingly unimportant at high temperatures [55].

Base-case simulations considered a single sub-bituminous coal char particle, with the properties shown in Table 3.3. The effects of the gasification reactions as a function of the gasification rate coefficients and gas environment were explored in this study. These effects were considered for a single particle, eliminating other variabilities, such as variations in the oxidation kinetics, or char properties that change during burnout, such as the particle

**Table 3.2**. Heterogeneous reaction mechanism

| Reaction | $A$ (mol/cm$^2 \cdot$ s) | $E$ (kJ/mol) |
|---|---|---|
| $C_b + C_s + O_2 \rightarrow CO + C(O)_s$ | $3.3 \times 10^{15}$ | 167.4 |
| $C(O)_s + C_b \rightarrow CO + C_s$ | $1.0 \times 10^{8}$ | 0. |
| $C_s + O_2 \rightarrow C(O_2)_s$ | $9.5 \times 10^{13}$ | 142.3 |
| $C(O_2)_s + C_b \rightarrow CO_2 + C_s$ | $1.0 \times 10^{8}$ | 0. |
| $C_s + CO_2 \rightarrow CO + C(O)_s$ | variable | 251.0 |
| $C_s + H_2O \rightarrow H_2 + C(O)_s$ | variable | 222.0 |

**Table 3.3**. Properties for the base-case simulations, which are the same as the sub-bituminous char studied by Geier et al. [56] and as assumed in the simulations by Hecht et al. [17].

| | |
|---|---|
| diameter | 100 $\mu$m |
| bulk density | 500 kg/m$^3$ |
| thermal conductivity | 1.33 W/m $\cdot$ K |
| (inert) ash content | 3% |
| tortuosity | 5 |
| void fraction | 0.4 |
| gas temperature | 1690 K |
| wall temperature | 500 K |
| emissivity | 0.8 |

porosity, diameter, and ash content. The small amount of ash that was modeled here was assumed to be inert, ignoring any potential catalytic effects.

The specific active surface area is also required to model this system. There is disagreement in the literature on how the pore structure is related to the surface area for heterogeneous oxidation and gasification reactions, as discussed by Molina and Mondragón [57], but there is widespread evidence that little of the micropore surface area (which dominates traditional measures of total char surface area) is accessed during high-temperature char oxidation and gasification [58–61]. In our previous simulations of char combustion, the active surface area was varied as a function of bulk gas oxygen concentration to get reasonable agreement of the predictions with the trends in measured char particle temperatures as a function of bulk gas oxygen content [17]. While a somewhat reduced surface area (or surface active site density) might arise from devolatilizing coal particles in the higher temperature volatiles flames produced in an elevated $O_2$ environment, the magnitude of the surface area variation (from 8 m$^2$/g at 12% $O_2$ down to 0.225 m$^2$/g at 36% $O_2$) that was required to match the model predictions with the experimental data strained belief.

Without conclusive experimental evidence of how the devolatilization condition affects the active surface area, in the current study, we sought agreement with experimentally measured char particle temperatures while keeping the assumed surface area density constant. The relative rate coefficients were fixed at our best-guess values at 800 °C ($6.2 \times 10^{-5}$ for gasification by $CO_2$ and $2.0 \times 10^{-4}$ for gasification by $H_2O$, each relative to the oxidation rate, as described previously). Then the activation energies were adjusted within the literature bounds (230–270 kJ/mol for gasification by $CO_2$ and 190–270 kJ/mol for gasification by $H_2O$ [37]) until predicted temperatures matched experimentally measured temperatures under the constraint of constant specific surface area.

The predicted char particle temperatures are shown in Fig. 3.1 for char reacting in $N_2$ diluent environments as a function of the presumed active surface area. The gasification reactions tend to cool the char particles as the active surface area increases. When both gasification reactions are included in the reaction mechanism, good agreement between the model and experiment can be achieved at a fixed surface area at all three of the oxygen concentrations studied with kinetic parameters in the range of values reported in the literature. We find an active surface area of 10 $m^2/g$ with activation energies of 222 kJ/mol for steam gasification and 251 kJ/mol for gasification by $CO_2$ to give the best agreement between the model predictions and mean measured char particle temperatures [56]. This magnitude of surface area approximately corresponds to the sum of macropore and mesopore surface area as measured by mercury porisiometry for high heating rate chars investigated experimentally [62] and therefore is physically reasonable.

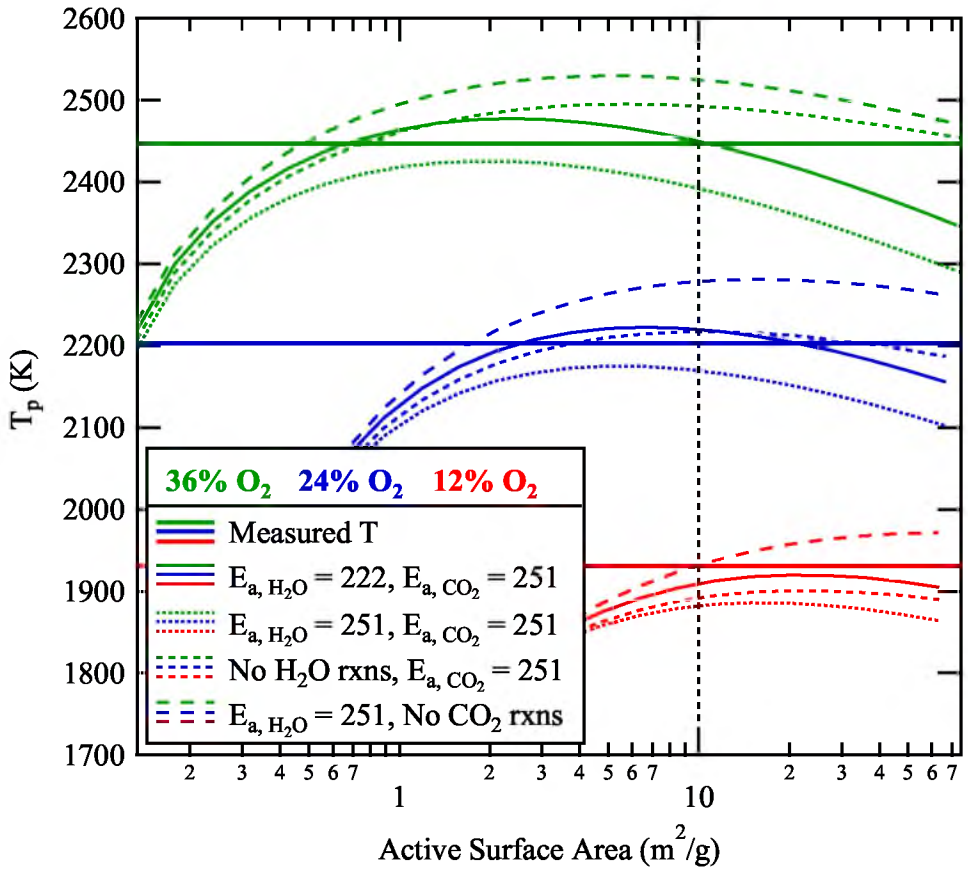


**Figure 3.1**. Predicted and measured [56] char particle temperatures for a particle reacting in a 1690K, 14% $H_2O$, $O_2$, balance $N_2$ environment while varying the presumed surface area and activation energy of the steam and $CO_2$ gasification reactions. Units of activation energy are kJ/mol.

To determine the effects of the gasification reactions over a wide range of possible rate coefficients, the activation energies were held fixed and the pre-exponentials, $A$, for the char gasification steps were varied in separate simulations. For gasification by $CO_2$, the pre-exponential value was varied from 0 (i.e. no gasification by $CO_2$) up to a value of $1.8 \times 10^{16}$ mol/cm$^2 \cdot$ s. For gasification by $H_2O$, the pre-exponential value was varied from 0 (i.e. no gasification by $H_2O$) up to a value of $2.2 \times 10^{15}$ mol/cm$^2 \cdot$ s. At 800 °C, these maximum pre-exponentials yield relative rate coefficients that are $2 \times 10^{-4}$ and $1 \times 10^{-3}$ (for $CO_2$ and steam, respectively) times the oxidation rate coefficient at this temperature. These correspond to the highest relative rate coefficients found in the literature by Goetz et al. [44] (for $CO_2$ gasification) and Degroot and Richards [46] (for gasification by $H_2O$). The wide ranges of gasification rate coefficients evaluated here were chosen both on account of the uncertainties in the actual gasification rate coefficients and to more clearly evaluate the trends in the char particle response as a function of the gasification rate coefficients.

Simulations were conducted for gas environments characteristic of dry-recycle oxy-fuel combustion, with a moisture level of 14 vol-%, and wet-recycle oxy-fuel combustion, wherein only the primary oxidizer is dried, with a furnace moisture content of 25 vol-%. The balance of the furnace gas was assumed to be composed of $O_2$ and $CO_2$. Oxygen levels ranging from 12 vol-% to 36 vol-% were considered, spanning the range from conventional combustion to strongly oxygen-enhanced combustion (in boilers char combustion generally occurs at substantially lower oxygen contents than exist in the boiler inlets). The effects of gas temperature and particle size were also evaluated, and environments with a $N_2$ diluent (characteristic of a conventional air-fired boiler) were simulated.

## 3.5 Results

### 3.5.1 Effect of Gasification Rate Coefficients on Particle Temperature and Species Profiles

The computed radial profiles of temperature and gas species for a 100 $\mu$m diameter char particle reacting in 12% $O_2$ in an oxy-fuel environment at 1690 K are shown in Fig. 3.2. The profiles start near the particle center and extend into the boundary layer to 100 times the particle radius. As shown in the top frame of Fig. 3.2, the rate coefficient of gasification by $CO_2$ affects the char temperature much more than the rate coefficient of gasification by $H_2O$. This is due to the combined effect of a higher concentration of $CO_2$ than steam in the surrounding gas, and the greater endothermicity of the $CO_2$ gasification reaction. At

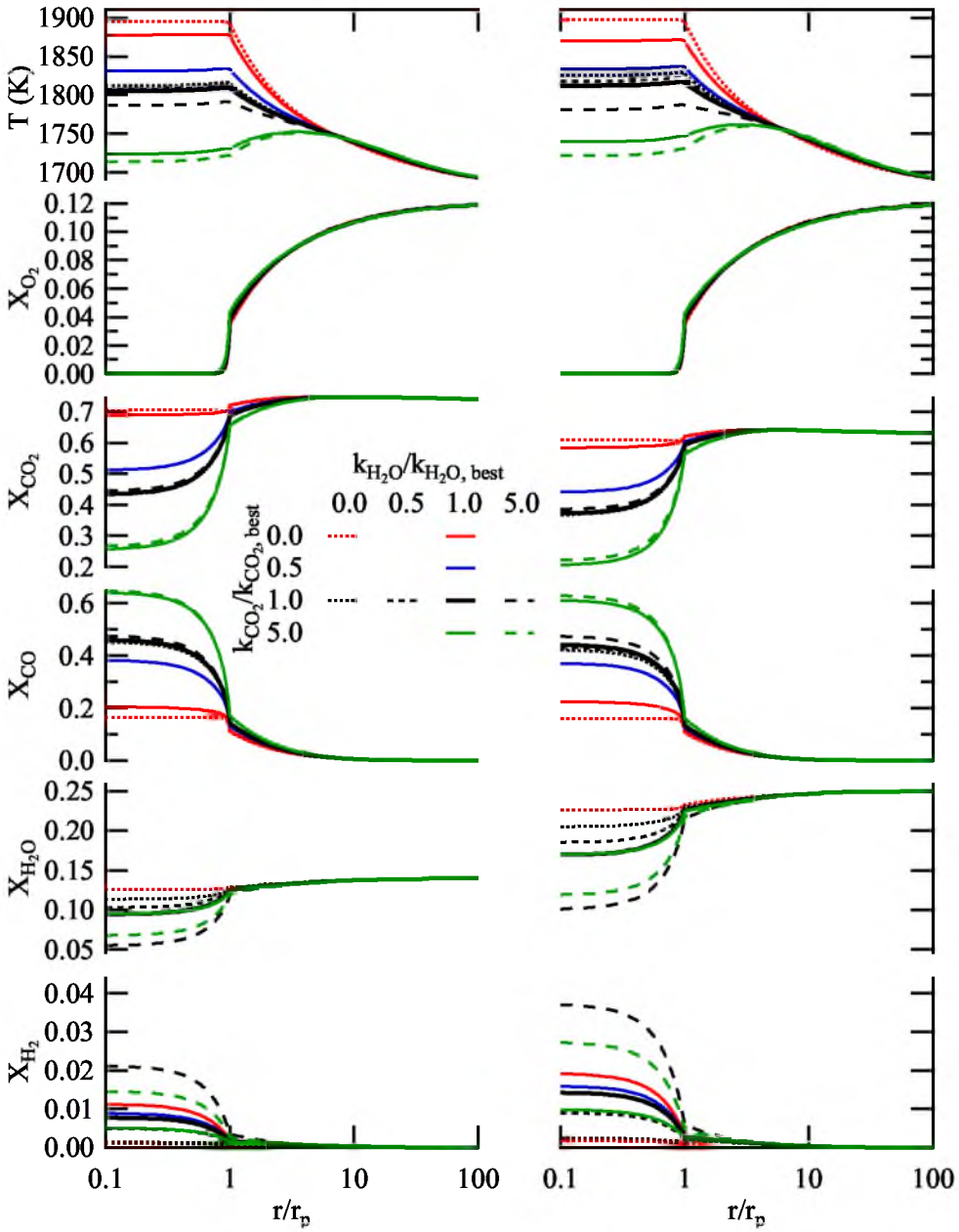


**Figure 3.2**. Temperature and species profiles as functions of normalized distance from the center of a 100 $\mu$m diameter char particle burning in 12% $O_2$ in $CO_2$ at 1690 K. $r/r_p = 1$ corresponds to the surface of the particle. The panels on the left represent a dry-recycle oxy-combustion environment, with 14% $H_2O$ in the bulk gas, whereas the panels on the right represent a wet-recycle oxy-combustion environment, with 25% $H_2O$ in the bulk gas. Different line colors represent different assumed rate coefficients for the $CO_2$ gasification reaction, whereas different line styles represent different assumed rate coefficients for gasification by $H_2O$, as shown in the legend. The thick black line represents the best-guesses of $CO_2$ and $H_2O$ gasification rate coefficients. For gasification by $CO_2$, the best-guess pre-exponential value (corresponding to a normalized rate coefficient of 1) is $3.6 \times 10^{15}$ mol/cm$^2 \cdot$ s and for gasification by $H_2O$, the best-guess pre-exponential is $4.4 \times 10^{14}$ mol/cm$^2 \cdot$ s.

our best-guess rate coefficient for gasification by $H_2O$, ignoring $CO_2$ gasification causes the particle temperature to be 60–70 K (depending on the $H_2O$ concentration in the bulk gas) higher than the result when using our best-guess rate coefficient for gasification by $CO_2$. Similarly, using a $CO_2$ gasification rate coefficient that is five times the best-guess rate coefficient results in a particle temperature that is lower by 70–80 K than the result using the best-guess $CO_2$ gasification rate coefficient. When fixing the $CO_2$ gasification reaction to its best-guess rate coefficient, ignoring $H_2O$ gasification only causes an error of 7–14 K, and using a $H_2O$ gasification rate coefficient that is five times the best-guess rate coefficient yields a particle temperature that is 18–30 K lower than the temperature prediction that includes the gasification reactions proceeding at the best-guess rates.

The species profiles in the lower frames of Fig. 3.2 show that under the modeled condition (with 12% $O_2$ in the bulk gas), the 100 $\mu$m char particle is burning near the diffusion limit, with a low concentration of $O_2$ ($\approx 4\%$) at the particle surface. The gasification reactions have little influence on the $O_2$ diffusion to the particle (and therefore barely affect the char oxidation rate). In contrast, the CO and $CO_2$ concentrations within the char particle are strongly influenced by the $CO_2$ gasification reaction, as this reaction converts solid carbon and $CO_2$ into CO. Also, as expected, the concentrations of $H_2O$ and $H_2$ within the char particle are strongly dependent on the steam gasification reaction rate coefficient. The $CO_2$ gasification reaction also affects the $H_2$ concentration within the char particle. When the $CO_2$ gasification reaction is ignored, a high particle temperature causes the steam gasification reaction to proceed at a relatively fast rate, generating significant $H_2$, and as the $CO_2$ gasification rate coefficient is increased, the particle temperature, steam gasification rate, and amount of $H_2$ generated by the steam gasification reaction all decrease.

To determine the influence of the gasification reactions during oxygen-enriched combustion, simulations were performed for the same char particle reacting in 24% and 36% $O_2$. Similar trends as those seen in the 12% $O_2$ environment were evident in both of these oxygen-enriched cases. Profiles from the simulations with 36% $O_2$ are shown here (in Fig. 3.3), as these show the strongest effects from the gasification reactions. As shown in Fig. 3.3, at a fixed steam gasification rate, predicted particle temperatures are up to 270 K higher than when the $CO_2$ gasification reaction proceeds using our best-guess rate coefficient. At five times the best-guess rate, the temperature is 140 K lower than the best-guess prediction. At this bulk $O_2$ level, the char particle temperature is over 2100 K, despite the occurrence of the endothermic gasification reactions. At this high temperature (which causes fast gasification rates), the $CO_2$ gasification reaction completely consumes

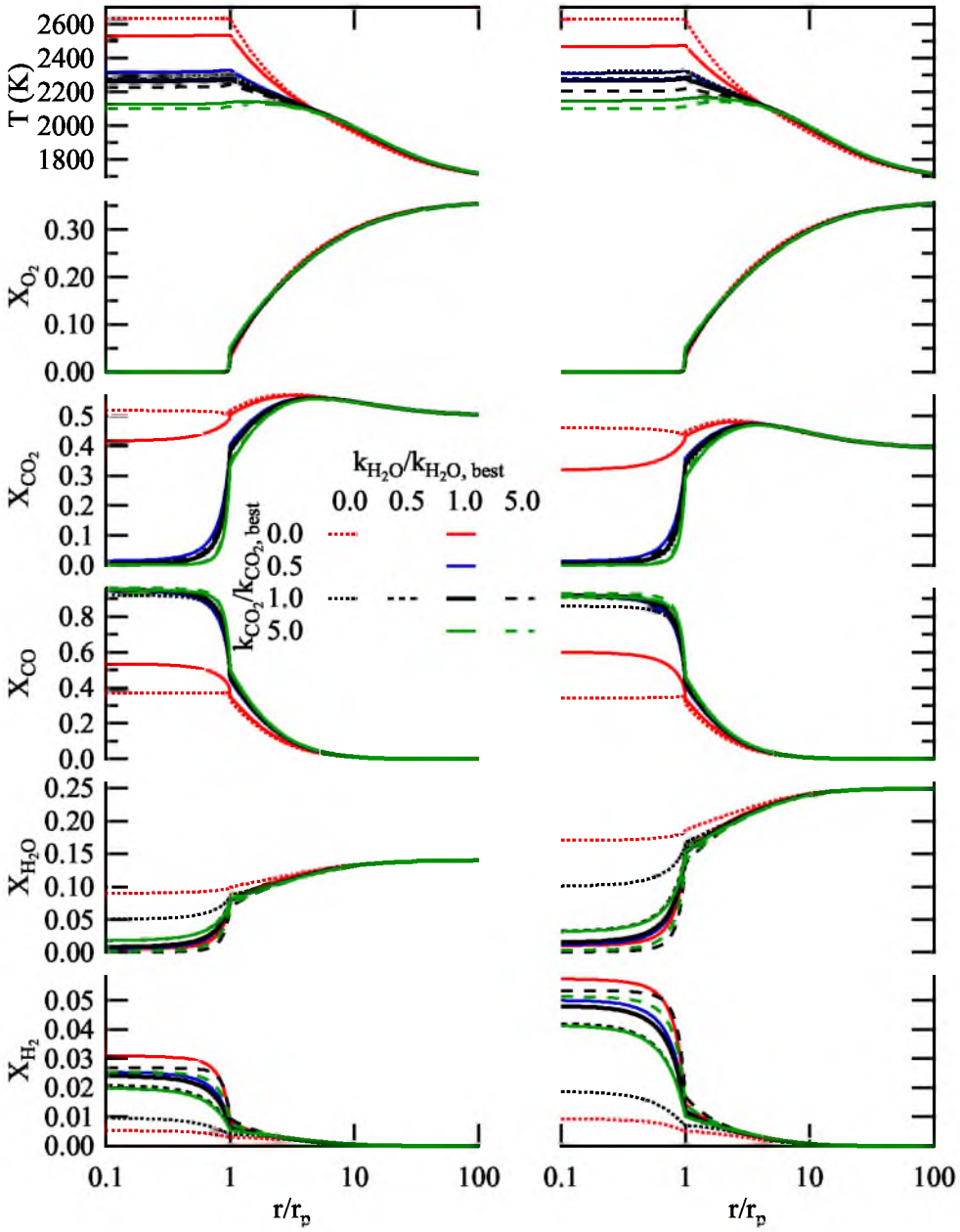


**Figure 3.3**. Temperature and species profiles as a function of normalized distance from the center of a char particle burning in 36% $O_2$ in $CO_2$ at 1690 K. Right/left panel conventions and line styles and colors are the same as for Fig. 3.2.

the $CO_2$ within the particle when the presumed gasification rate coefficient is at least half of the best-guess value. Similarly, steam is nearly completely consumed within the char particle when the rate coefficient for gasification by steam is at least half of its best-guess value. This is in contrast to the results for combustion in 12% bulk $O_2$ (shown in Fig. 3.2), where steam and $CO_2$ are only partially consumed within the char particle, for even the highest gasification rates considered. Similar to the 12% $O_2$ case, the oxidation of the 100 $\mu$m particle is proceeding near the diffusion limit, such that the gasification reactions have little impact on the $O_2$ diffusion profile through the boundary layer.

### 3.5.2 Effect of Gasification Rate Coefficients on Char Consumption Rate

Figure 3.4 presents contour plots of the char carbon consumption rates for a 100 $\mu$m diameter char particle burning in oxy-fuel combustion environments as functions of the $H_2O$ and $CO_2$ gasification rate coefficients. For both the dry- and wet-recycle cases, the carbon consumption rate is strongly dependent on the $CO_2$ gasification rate coefficient, whereas the steam gasification rate coefficient only has a significant influence for a relative rate coefficient greater than one (the contours are nearly vertical for the bottom half of each plot). For the wet-recycle cases, the contours have a greater dependence on the $H_2O$ gasification rate coefficient because the higher steam concentration increases the steam gasification rate. The steam gasification rate coefficient (relative to the $CO_2$ gasification rate coefficient) has less influence on carbon consumption as the oxygen concentration increases, for both the dry- and wet-recycle cases. Because the activation energy of the $CO_2$ gasification reaction is higher than that of the steam gasification reaction, at high oxygen concentrations (resulting in high particle temperatures), the $CO_2$ gasification rate will increase faster than the steam gasification rate. Thus, at higher oxygen concentrations, the steam gasification reaction becomes relatively less important. The contour plots in Fig. 3.4 show a carbon consumption rate variation of about 10% over the range of relative rate coefficients considered in this study.

For a given oxygen concentration, an increase in the $H_2O$ concentration causes the net carbon consumption to increase slightly, as shown by the carbon consumption rates listed in Fig. 3.4. Although the carbon consumption rate does not appear to be as strongly tied to the steam gasification rate coefficient as the $CO_2$ rate coefficient, the steam gasification reaction does consume carbon. In these simulations, as in boilers, an increase in steam concentration

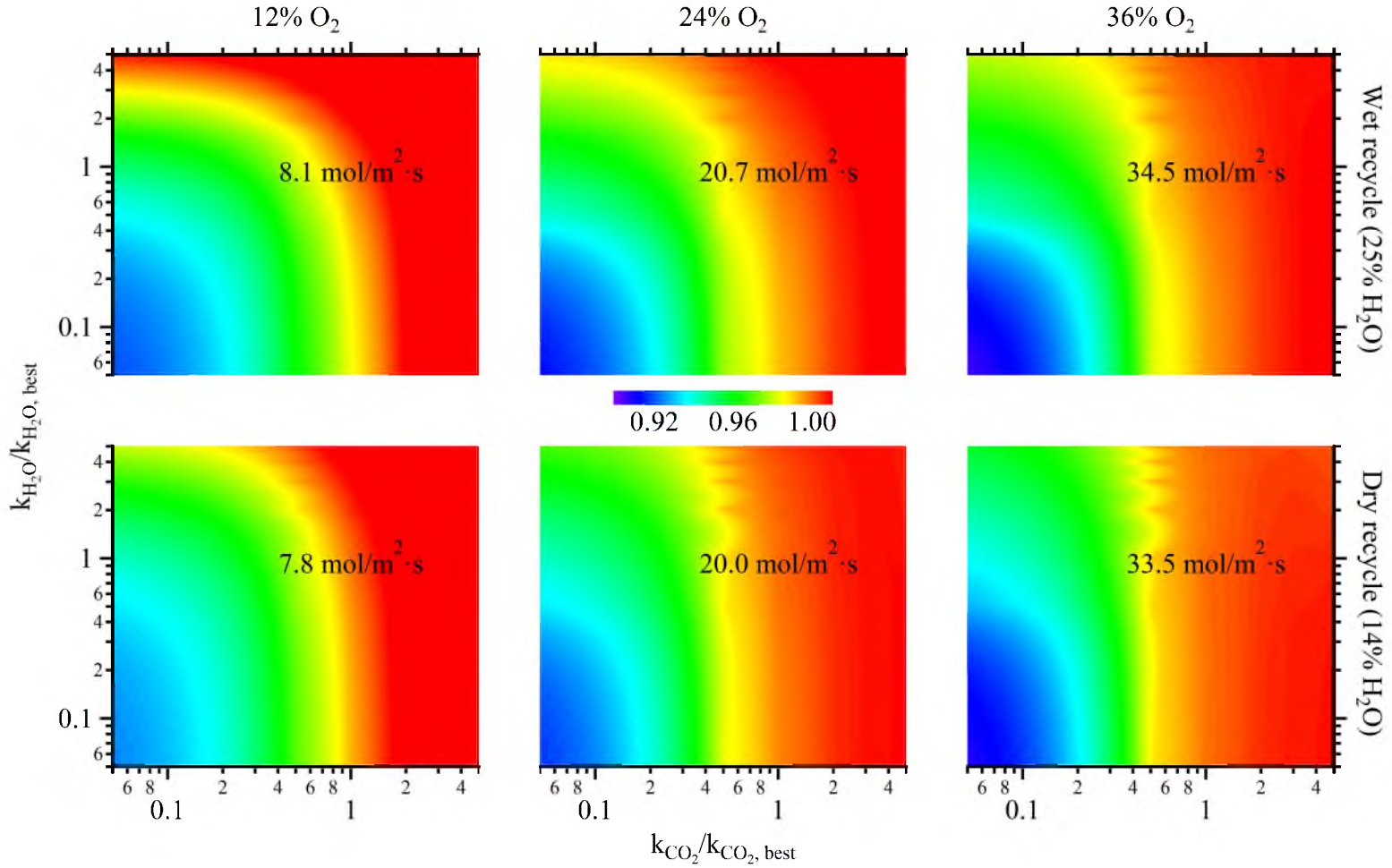


**Figure 3.4**. Contour plots showing the total carbon consumption rates as the $CO_2$ and $H_2O$ gasification rate coefficients are varied. The gasification rate coefficients have been normalized using the same best-guess pre-exponentials as for Figs. 3.2 and 3.3. Carbon consumption rates have been normalized by the rate at the best-guess gasification rates (normalized rate of 1). Absolute carbon consumption rates at the best-guess gasification rate coefficients are shown on the plots.

requires a decrease in $CO_2$ concentration, convolving the effect of concentration variations. The relative contributions of oxidation, $CO_2$ gasification, and steam gasification to carbon consumption are shown in Fig. 3.5. With 12% oxygen in the bulk gas (which yields relatively low reaction temperatures), gasification reactions (with $CO_2$ and $H_2O$) are responsible for about 20% of the carbon consumption. At 36% $O_2$ in the bulk gas, these gasification reactions account for about 31% of the overall carbon consumption. Inspection of the right panel as compared to the left shows that exchanging some (0.11 atm) of the $CO_2$ for $H_2O$ causes the relative carbon consumption due to steam to nearly double while only slightly decreasing the relative consumption from $CO_2$, and results in a net increase in the relative carbon consumption from gasification reactions. The relative consumption from oxygen also decreases slightly while the surface temperature increases by a few degrees as the steam concentration increases.

Figure 3.5 highlights the complex interplay between the heterogeneous reactions occurring during the oxy-combustion of pulverized coal. If gasification reactions are not considered, nearly 400 kJ/mol$_C$ is released by the oxidation reaction, leading to predictions of high particle temperatures shown by the open circles in Fig. 3.5. When the endothermic gasification reactions are included, the enthalpy released by the heterogeneous reactions drops significantly, resulting in considerably lower predicted particle temperatures. The enthalpy released can be calculated by summing the product of the reaction rate and its heat release for the oxidation and gasification reactions. At 12% $O_2$ in the bulk gas, around 280 kJ/mol$_C$ are released by the reactions, and at 36% $O_2$, only about 220 kJ/mol$_C$. The rate of carbon oxidation by $O_2$ is slower at lower temperature, but the additional carbon consumption from the $CO_2$ and $H_2O$ gasification reactions slightly increases the predicted carbon consumption rate. Boundary layer reactions, for example, $O_2$ reacting with the CO and $H_2$ produced from the gasification reactions, feed energy back to the particle, adding additional complexity to an energy balance.

### 3.5.3 Gas Temperature and Particle Size Effects

Figure 3.6 summarizes the results of a series of simulations in which the ambient gas temperature and the char particle diameter were varied over a wide range. The left panel of Fig. 3.6 shows the carbon consumption rate and particle temperature for a 100 $\mu$m char particle burning in 12% and 36% $O_2$ dry-recycle oxy-fuel combustion environments as a function of the bulk gas temperature. Both the particle temperature and the carbon con-

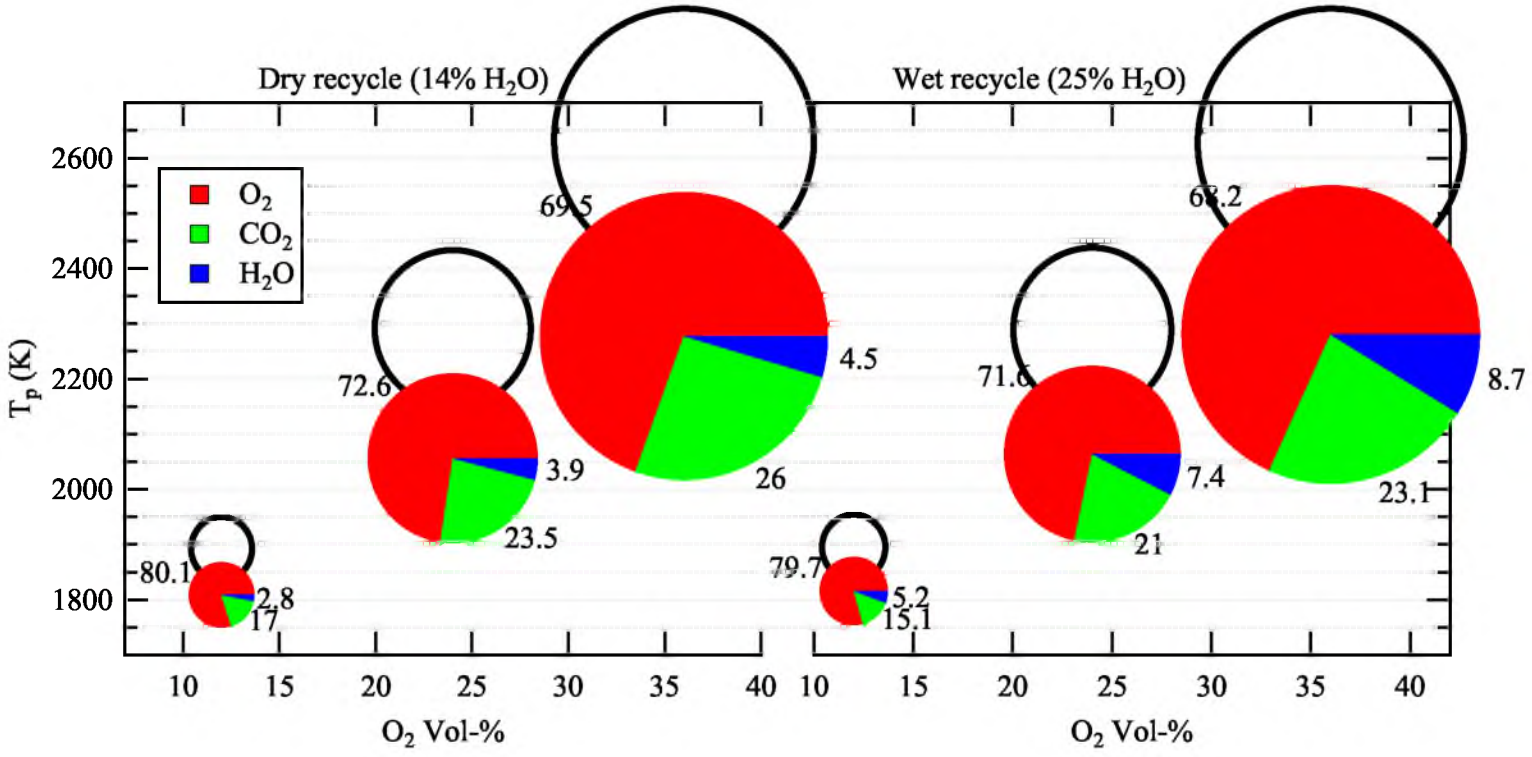


**Figure 3.5**. Relative contributions to carbon consumption by reactions with oxygen, carbon dioxide, and steam. Size of circle is proportional to overall carbon consumption rate, and percentages of contributions are shown on the chart. Open circles show particle surface temperature and relative carbon consumption rate without gasification reactions (only oxidation), and filled circles include gasification reactions at our best-guess rate coefficients.

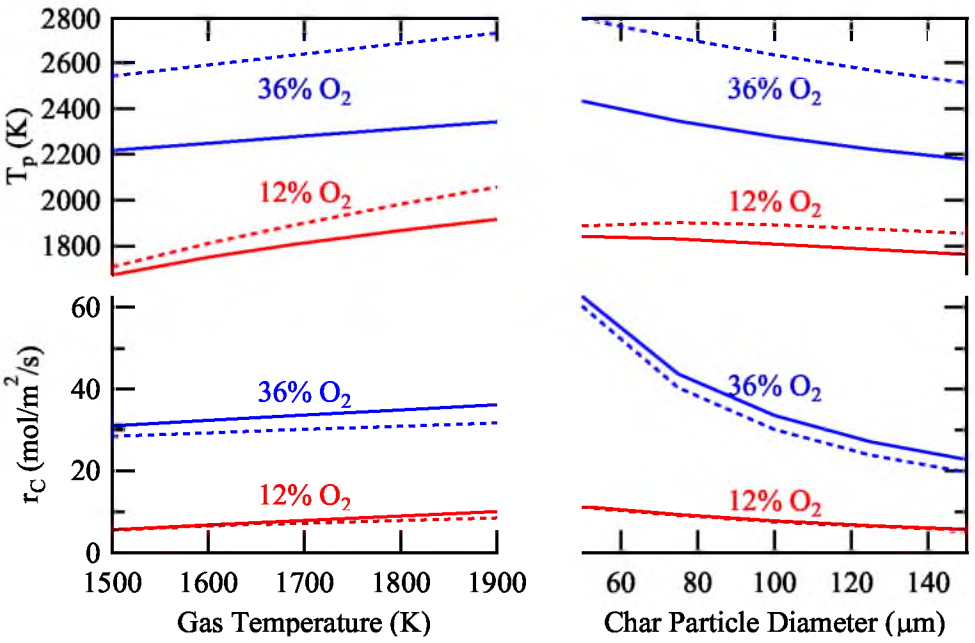


**Figure 3.6**. Particle temperature and carbon consumption rate as a function of gas temperature and particle size for dry-recycle oxy-fuel combustion in 12% and 36% $O_2$. Solid lines are simulations using the best-guess gasification rates, dashed lines are simulations without gasification reactions. When varying gas temperature, a particle diameter of 100 $\mu$m is used, and when varying particle diameter a gas temperature of 1690 K is used.

sumption rate increase as the gas temperature increases, due to the reaction rates increasing at higher temperatures. Simulations that ignore the gasification reactions (dashed lines) clearly predict higher temperatures and lower carbon consumption rates than simulations that include the gasification reactions. This is not an intuitive result, once again showing the trade-offs between endothermic gasification reactions lowering the reaction temperatures and rates, and the additional carbon consumption caused by the gasification reactions. As the gas temperature increases, the effect of the gasification reactions on particle temperature and consumption rate increases, as would be expected based on the high activation energies of these reactions.

The right panel of Fig. 3.6 shows the carbon consumption rate and particle temperature as a function of the char particle size during combustion in a 1690 K environment. Larger particles burn at lower temperature and at lower surface-specific rates than smaller particles because larger particles have greater radiative losses and less reactant penetration. As a measure of reactant penetration, effectiveness factors, which are the ratio of the carbon consumption rate by a species to the theoretical carbon consumption rate by that species if not slowed by pore diffusion, were calculated.

As shown in Table 3.4 , oxygen penetrates much less than either $CO_2$ or $H_2O$ and there is less reactant penetration under the high oxygen conditions. From a practical perspective, reactant penetration not only affects the consumption of carbon and the local heat release, but also the local concentration of $CO_2$, which can influence the extent of ash vaporization during char combustion [63].

At all sizes considered, gasification reactions decrease the particle temperature while increasing the carbon consumption rate. During combustion in 36% $O_2$, the considerable effect of gasification reactions on the char particle temperature is nearly independent of particle size. During combustion in 12% $O_2$, the effect of the gasification reactions on char temperature is quite small for 50 $\mu$m particles, and then increases slightly to a temperature difference that is once again nearly independent of particle size for particles larger than

**Table 3.4**. Effectiveness factors for each reactant under dry-recycle oxy-fuel combustion conditions.

| | 12% $O_2$ | | 36% $O_2$ | |
|---|---|---|---|---|
| | 50 $\mu$m | 150 $\mu$m | 50 $\mu$m | 150 $\mu$m |
| $O_2$ | 0.24 | 0.11 | 0.09 | 0.05 |
| $CO_2$ | 0.99 | 0.83 | 0.55 | 0.37 |
| $H_2O$ | 1.0 | 0.90 | 0.82 | 0.53 |

80 $\mu$m. Reactant penetration and radiant and conductive heat losses all affect the particle temperature, and this complex balance causes the local maximum temperature around 80 $\mu$m, when gasification reactions are not included in the simulations. This local maximum temperature in the 12% $O_2$ condition shifts to smaller particles (below 50 $\mu$m) when the gasification reactions are included in the simulations.

### 3.5.4 Gasification Reactions in Oxy- vs. Air-fired Combustion Environments

Because of the increased concentrations of $CO_2$ and (most likely) $H_2O$ in an oxy-fuel combustion environment, it is natural to consider the potential influence of gasification reactions for this application. However, during conventional, air-fired char combustion, gasification reactions may also contribute to the consumption of solid carbon. Locally, or throughout the reactor, there may be high steam concentrations from residual moisture in the coal and from volatile combustion. Also, high $CO_2$ and $H_2O$ concentrations may be generated within the boundary layer of char particles when CO and $H_2$ are fully oxidized to $CO_2$ and $H_2O$. To investigate the potential role of these reactions under such conditions, simulations were conducted using the same base conditions as for the oxy-fuel simulations, but with $N_2$ replacing $CO_2$ as the bulk diluent gas. A small concentration of $CO_2$ (4 vol-%) was assumed to remain in the bulk gas, as well as 14 vol-% $H_2O$, which would be characteristic of an air-fired boiler, and is consistent with our previous study [17].

Temperature and species profiles for a 100 $\mu$m char particle reacting in an air-fired environment are presented in Fig 3.7. As with the oxy-fuel simulations, particle temperatures are higher if gasification reactions are excluded from the calculations, as shown in the top frame. This effect is more pronounced at higher oxygen concentrations (and higher particle temperatures), shown in the right frames of the figure. Char oxidation and boundary layer reactions in fact produce substantial $CO_2$ near the particle. If gasification reactions are included in the simulations, the $CO_2$ is at least partly consumed and converted to CO within the particle. However, CO is oxidized in the boundary layer, producing a higher concentration of $CO_2$ near the particle than either in the bulk gas, or within the particle. Similarly, $H_2O$ from the bulk gas is at least partly consumed within the particle. The $H_2O$ gasification reaction produces one mole of CO and one mole of $H_2$ from one mole of $H_2O$, enhancing the molar flux of CO coming from the particle (adding to the flux from the $CO_2$ gasification and oxidation reactions). The $H_2$ generated heterogeneously is oxidized back

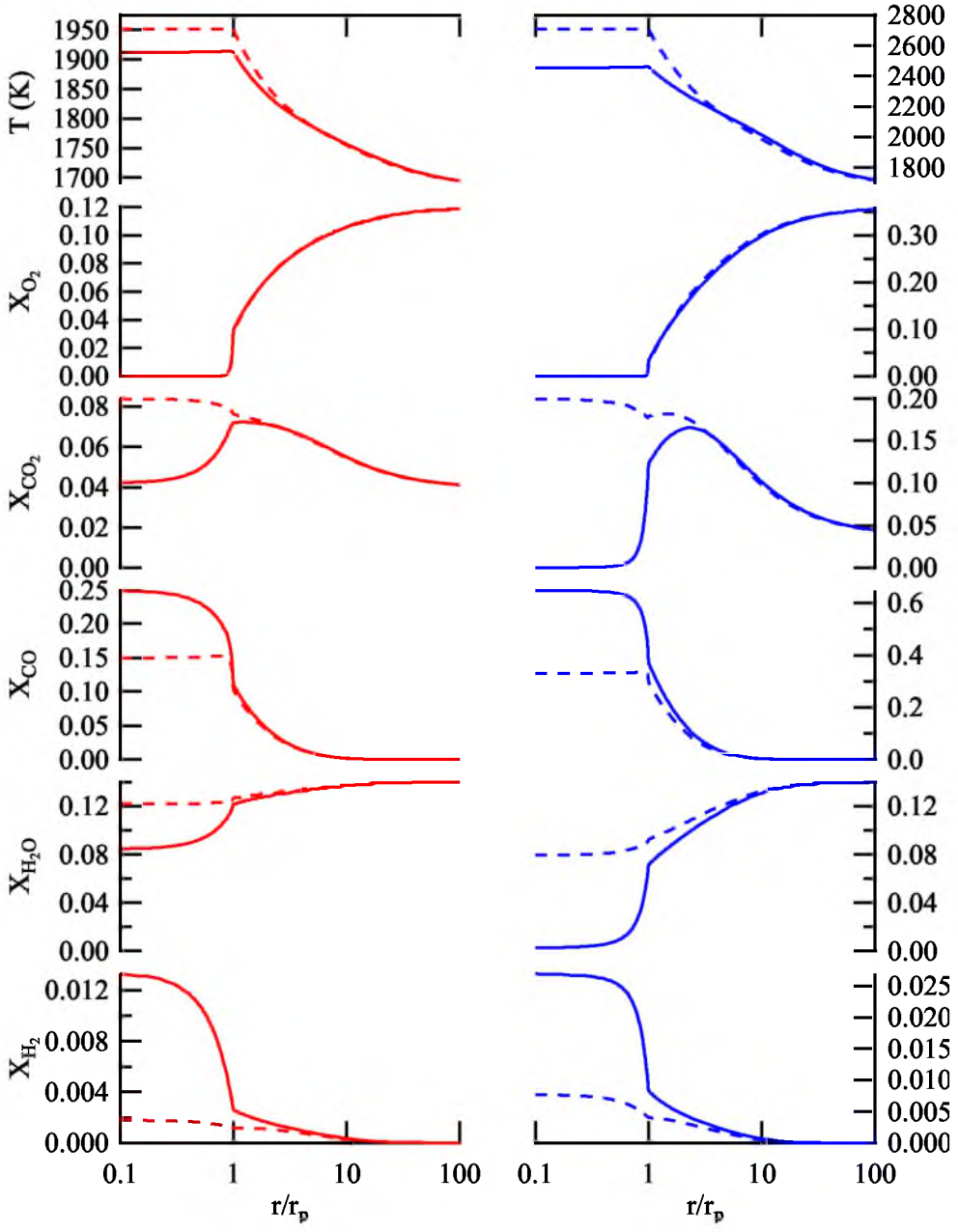


**Figure 3.7**. Temperature and species profiles as a function of normalized distance from the center of a 100 $\mu$m char particle burning in an air-fired environment ($N_2$ diluent) at 1690 K. Left panel are results for 12% $O_2$ in the bulk gas, and the right panel are results for 36% $O_2$ in the bulk gas (note the separate axes). Solid lines include oxidation and gasification reactions using the best-guess rate coefficients while dashed lines only include oxidation reactions.

to steam in the boundary layer, with no net generation of $H_2O$.

Table 3.5 gives the calculated decrease in particle temperature and increase in the char consumption rate for equivalent $N_2$ diluent and $CO_2$ diluent reaction conditions when including the best-guess steam and $CO_2$ gasification rate coefficients. As is apparent, the gasification reactions do play a role in the prediction of both temperature and char consumption rates during air-fired combustion. As the ambient oxygen concentration increases, the char particles burn at a higher temperature, increasing the rates of the gasification reactions and the conversion of gasification products (CO to $CO_2$ and $H_2$ to $H_2O$) in the particle boundary layer, leading to a greater influence of the gasification reactions. The gasification reactions have a greater influence on char consumption for oxy-fuel combustion conditions, as expected, but for char combustion in elevated oxygen levels, regardless of the diluent gas composition, the gasifications have a significant impact. With the activation energies used in this study, and our best-guess relative rate coefficients at 800 °C, the gasification rate coefficients scale to about 1% of the oxidation rate coefficient at 2000 K. Although the oxidation rate coefficient is appreciably higher than the gasification rate coefficients, the gasification reactions are significant due to the local concentrations of $CO_2$ and $H_2O$ and their greater penetration into the particle.

A higher concentration of steam slightly decreases the influence of the gasification reactions on the particle temperature, but increases the carbon consumption rate, which can be seen by comparing the dry- to wet-recycle cases in Table 3.5. This behavior is due to the higher activation energy and endothermicity of the $CO_2$ gasification reaction than the $H_2O$ gasification reaction, as discussed earlier with respect to Figs. 3.4 and 3.5.

**Table 3.5**. Decrease in surface temperature and increase in char conversion rate if gasification reactions are included in the model. Percentages are calculated based off the values considering only oxidation reactions.

| | 12% $O_2$ | | 24% $O_2$ | | 36% $O_2$ | |
|---|---|---|---|---|---|---|
| | $T$ [K] | $r_C$ $\left[\frac{mol}{m^2 s}\right]$ (%) | $T$ [K] | $r_C$ $\left[\frac{mol}{m^2 s}\right]$ (%) | $T$ [K] | $r_C$ $\left[\frac{mol}{m^2 s}\right]$ (%) |
| $N_2$ diluent | 37 | 0.3 (3.4) | 144 | 1.2 (5.9) | 246 | 2.5 (7.6) |
| dry oxy-fuel | 84 | 0.6 (8.8) | 235 | 1.8 (10.1) | 356 | 3.4 (11.4) |
| wet oxy-fuel | 79 | 0.7 (9.5) | 225 | 2.0 (10.7) | 347 | 3.7 (11.9) |

### 3.5.5 Implications for Char Combustion Modeling and Interpretation of Experimental Measurements

Using a fine radial mesh on each particle and detailed kinetics to determine the temperature and species profiles in a coal fired boiler would require immense computing resources. To reduce computational complexity, CFD codes typically consider char particles as source/sink terms to the gas-phase model and employ global kinetics in a heterogeneous char combustion submodel. CFD calculations of conventional, air-fired boilers, and even several recent oxy-combustion submodels have considered oxygen as the only molecule reacting with the solid carbon [6]. As shown in this study, neglecting reactions with $CO_2$ and $H_2O$ causes a higher predicted particle temperature, often significantly higher than those from simulations that include gasification reactions, and a lower carbon consumption rate. This can lead to erroneous predictions of of burnout times and heat release profiles in oxy-combustion simulations. Since the gasification reactions can also influence the perceived global kinetics under air-fired conditions, the oxidation kinetics currently used in CFD codes will likely need to be reevaluated when including these reactions. In general, the relevance of gasification reactions hampers derivation of accurate high-temperature oxidation kinetic data because the oxidation combustion products ($CO_2$ and $H_2O$) are themselves reactants and are present in high concentration locally near the reaction sites.

Conversion of char nitrogen to $NO_x$ (and $NO_x$ precursors) is highly dependent on temperature [53]. Modeling efforts to predict these pathways must be sensitive to the effect of the gasification reactions on char combustion temperatures. Reactions of coal char with $CO_2$ and $H_2O$ might also influence the way in which char-N (and char-S) is released from the particle, potentially adding complexity to the prediction of $NO_x$ (and $SO_x$) formation.

The steam gasification reaction is important when considering the extent to which the flue-gas must be dried before recycle. We have shown that with a higher steam concentration, the steam gasification reaction causes the char combustion temperature to decrease and the carbon consumption rate to increase. These effects must be accounted for when designing an oxy-combustion system.

This study has demonstrated that char gasification reactions influence the char temperature and carbon consumption during both oxy- and conventional combustion of coal, and we have demonstrated the influence over a wide range of potential gasification rate coefficients. Accurate high-temperature, atmospheric pressure gasification rate data are still needed for more quantitative treatment of these reactions and improved CFD coal combustion models.

## 3.6 Conclusions

Using rate parameters for char gasification by steam and $CO_2$ established from literature data, the char combustion of a 100 $\mu$m diameter high-volatile bituminous coal particle was modeled for candidate dry-recycle and wet-recycle oxy-fuel combustion environments with various oxygen levels using the Surface Kinetics in Porous Particles (SKIPPY) code. The simulations revealed that char gasification by both steam and $CO_2$ reduce the char combustion temperature, with the $CO_2$ gasification reaction having the predominant influence. The gasification reactions were found to have greater influence for char combustion in elevated oxygen environments, where the char combustion temperature is higher. The gasification reactions augment the char carbon consumption rate, but only by about 10%. Simulations were also conducted over a range of gas temperatures and particle sizes. In general, the gasification reactions have increasing influence as the gas temperature increases (for a given $O_2$ concentration) and as the particle size increases. Simulations of traditional $N_2$ diluent combustion reveal that gasification reactions can influence char combustion in these environments, as well. Based on our existing (albeit limited) knowledge of char gasification rates, it appears that it is important to include these reactions when interpreting experimental measurements of char combustion or when simulating char combustion, especially in oxy-fuel combustion environments.

# CHAPTER 4

# ANALYSIS OF THE ERRORS ASSOCIATED WITH TYPICAL PULVERIZED COAL CHAR COMBUSTION MODELING ASSUMPTIONS FOR OXY-FUEL COMBUSTION

## 4.1 Abstract

In CFD models of pulverized coal combustion, which often have complex, turbulent flows with millions of coal particles reacting, the char combustion submodel needs to be computationally efficient. There are several common assumptions that are made in char combustion models that allow for a compact, computationally efficient model. In this work, oft used single- and double-film simplified models are described, and the temperature and carbon combustion rates predicted from these models are compared against a more accurate continuous-film model. Both the single- and double-film models include a description of the heterogeneous reactions of carbon with $O_2$, $CO_2$, and $H_2O$, along with a Thiele-based description of reactant penetration. As compared to the continuous-film model, the double-film model predicts higher temperatures and carbon consumption rates, while the single-film model gives more accurate results. A single-film model is therefore preferred to a double-film model for a simplified, yet fairly accurate description of char combustion. For particles from 65-135 $\mu$m, in $O_2$ concentrations ranging from 12-60 vol-%, with either $CO_2$ or $N_2$ as a diluent, particle temperatures from the single-film model are expected to be accurate within 270 K, and carbon consumption rate predictions should be within 16%, with greater accuracies for a $CO_2$ diluent and at lower bulk oxygen concentrations. A

In Press *Combustion and Flame*, available at `http://dx.doi.org/10.1016/j.combustflame.2013.02.015`. Coauthors: Christopher R. Shaddix, JoAnn S. Lighty

single-film model that accounts for reactant penetration and both oxidation and gasification reactions is suggested as a computationally efficient submodel for coal char combustion that is reasonably accurate over a wide range of gas environments.

## 4.2 Nomenclature

| | |
|---|---|
| $A_0$ | pre-exponential factor for rate coefficient [$\mathrm{mol_C/s{\cdot}m^2 \cdot (mol_{gas}/m^3)}$] |
| $c$ | molar concentration [$\mathrm{mol/m^3}$] |
| $c_p$ | heat capacity [J/mol·K] |
| $D$ | diffusivity [$\mathrm{m^2/s}$] |
| $E_a$ | activation energy [J/mol] |
| $\epsilon$ | emissivity of the particle |
| $\phi$ | porosity (or void fraction) |
| $h$ | molar enthalpy [J/mol] |
| $\eta$ | effectiveness factor |
| $k$ | reaction rate coefficient [$\mathrm{mol_C/s{\cdot}m^2 \cdot (mol_{gas}/m^3)}$] |
| $\kappa$ | heat transfer Péclet number |
| $\kappa_m$ | mass transfer Péclet number |
| $\lambda$ | gas thermal conductivity [W/m·K] |
| $\mathrm{M_T}$ | Thiele modulus |
| $N$ | moles [mol] |
| $n_{\mathrm{gas}}$ | number of gas phase species |
| $P$ | Pressure [Pa] |
| $Q$ | heat [J] |
| $R$ | universal gas constant [J/mol·K] |
| $r$ | radius [m] |
| $\sigma$ | Stefan-Boltzmann constant [$\mathrm{W/m^2{\cdot}K^4}$] |
| $\sigma_r$ | specific surface area for heterogeneous reactions [$\mathrm{m^2/m^3}$] |
| $\tau$ | tortuosity |
| $T$ | temperature [K] |
| $x$ | mole fraction |

*Subscripts*

| | |
|---|---|
| 1 | between the particle and flame sheet |
| 2 | between the flame sheet and $\infty$ |

| | |
|---|---|
| app | apparent |
| C | carbon from the particle |
| eff | effective |
| $f$ | at the flame sheet |
| $\infty$ | outside the boundary layer in the bulk gas |
| $j$ | reaction number |
| $p$ | surface of the particle |
| $i$ | species $i$ |
| ref | reference |
| $t$ | total of all gas species |
| $w$ | wall (to which the particle is radiating) |

*Superscripts*

| | |
|---|---|
| $\dot{}$ | flow rate [$s^{-1}$] |
| $\bar{}$ | mean value |
| $''$ | per unit area [$m^{-2}$] |

## 4.3 Introduction

Char combustion is a complex process that involves gaseous transport, homogeneous gas-phase chemistry, heterogeneous gas-solid chemistry, and porous media transport through tortuous geometries. Equations to mathematically describe these phenomena exist, but using spatially resolved detailed models for a large number of particles reacting in complex, often turbulent flow conditions would require computational power of an immense scale. Assumptions and simplifications are regularly made and often necessary to model char combustion [64–67].

Two common char combustion submodels used in CFD simulations are one developed by Baum and Street [68], and a model first proposed by Smith [9]. In both of these models, oxygen is the only species that reacts with the char, while recent work has suggested that gasification reactions of char with $CO_2$ and $H_2O$ can have an impact on combustion temperatures and burning rates [17, 28, 56, 69]. The Baum and Street model is based on apparent kinetics, wherein oxygen diffusion and kinetic resistances govern the burning rate, but oxygen does not penetrate into the pores of the char. Smith's model includes reactant penetration, based on the Thiele modulus, and the combustion rate is dependent

on intrinsic kinetics and the pressure of oxygen at the particle surface. In both of these models, homogeneous chemistry in the boundary layer is neglected.

Globally, the reactions of carbon with combustion gases are

$$2C + O_2 \rightarrow 2CO \tag{4.1}$$

$$C + O_2 \rightarrow CO_2 \tag{4.2}$$

$$C + CO_2 \rightarrow 2CO \tag{4.3}$$

$$C + H_2O \rightarrow CO + H_2 \tag{4.4}$$

There is a multitude of literature documenting experiments to measure the kinetics of these reactions, including those specifically aimed at determining the relative production of CO and $CO_2$ during oxidation [70, 71] and those aimed at determining the relative rates of gasification (Rxns. 4.3 and 4.4) to oxidation [40, 44–49]. Regardless of the specific rates, carbon preferentially oxidizes to CO at high temperature, and there is a potential for $H_2$ to be present in the boundary layer. Oxidation of CO and $H_2$ in the boundary layer can alter the energy balance and the species available for reaction at the particle surface.

In this work, we seek to quantify uncertainties that arise from typical pulverized coal char combustion modeling assumptions. Some of the modeling assumptions examined in this analysis include the effects of homogeneous chemistry, the description of the heterogeneous chemical reactions, and intraparticle diffusion and reaction. Bounds on errors in char particle temperature and carbon consumption rate are determined, to aid in the interpretation of CFD model results that make these assumptions and guide the development of char combustion submodels. In particular, assessments of the uncertainty in CFD predictions of coal boiler performance (e.g. heat transfer, LOI, and pollutant formation) rely on such an evaluation of the uncertainties in the char combustion model.

## 4.4 Description of Models

In this work, several models of varying complexity are compared to each other. Across all models, the following is assumed:

- a single, spherical particle in an unconstrained and unperturbed boundary-layer
- steady-state
- a 1-dimensional (radial) domain

- gases are radiantly inactive over this spatial scale

The most detailed and physically accurate model used in this work is the Surface Kinetics in Porous Particles code (SKIPPY), as described elsewhere [28]. SKIPPY solves the steady-state mass, species, and energy conservation equations for a reacting porous particle and its reacting boundary layer. From this solution, SKIPPY predicts species concentrations and temperatures within the pores of the char, at the outer surface of the char, and within the boundary layer surrounding the char. Both heterogeneous (gas-solid) and gas-phase chemical reactions are considered. In the work presented here, GRI-MECH 3.0 [52] was used to describe the gas-phase reaction kinetics, while the heterogeneous char reaction kinetics were described using the mechanism specified in Table 4.1. This mechanism is the same as that used in our previous work [28]. Oxidation and gasification reactions are treated as adsorption-limited, with arbitrarily fast desorption reaction rates that guarantee insignificant accumulation of oxygen complexes on the surface of the char. Recent work has suggested a 5-step mechanism to describe carbon oxidation rather than this 4-step oxidation mechanism to capture both the pressure and temperature dependence of the $CO_2/CO$ ratio [72]. Since the 4-step surface mechanism captures the more important temperature dependence (but not the pressure dependence) of the $CO_2/CO$ ratio, it should be accurate under the atmospheric pressure conditions considered in this analysis. The rate coefficients chosen for the oxidation and gasification reactions are based on the analysis conducted in our previous work [17, 28].

Two simplified models are compared to SKIPPY in this work. The first is a single-film model, which assumes there are no reactions in the boundary layer. The second model considered is a double-film model, which is closely related to the Moving Flame Front model described by Zhang et al. [73–76], except our model accounts for Stefan flow. The double-film model assumes that there is an infinitely-thin flame-sheet at a point in the

**Table 4.1**. Heterogeneous reaction mechanism. The density of surface carbon sites is $1.7 \times 10^{-5}$ $\mathrm{mol_{C_s}/m^3}$.

| Reaction | $A$ (mol/cm$^2$ ·s) | $E_a$ (kJ/mol) |
|---|---|---|
| $C_b + C_s + O_2 \rightarrow CO + C(O)_s$ | $3.3 \times 10^{15}$ | 167.4 |
| $C_s + O_2 \rightarrow C(O_2)_s$ | $9.5 \times 10^{13}$ | 142.3 |
| $C_s + CO_2 \rightarrow CO + C(O)_s$ | $3.6 \times 10^{15}$ | 251.0 |
| $C_s + H_2O \rightarrow H_2 + C(O)_s$ | $4.4 \times 10^{14}$ | 222.0 |
| $C(O)_s + C_b \rightarrow CO + C_s$ | $1.0 \times 10^{8}$ | 0. |
| $C(O_2)_s + C_b \rightarrow CO_2 + C_s$ | $1.0 \times 10^{8}$ | 0. |

boundary layer that converts CO to $CO_2$ and $H_2$ to $H_2O$. At all other points in the boundary layer, the gases are unreactive. In contrast to a classical double-film model, the oxygen is not necessarily completely consumed in the boundary layer, and $O_2$, $CO_2$, and $H_2O$ each react and consume the solid carbon.

In the unreactive region(s) of the boundary layer, the total and species molar flow rates are constant. Assuming that the assumptions associated with Fick's law hold, and that we can decouple the species continuity equations by assuming an effective diffusivity, species continuity reduces to

$$\dot{N}_i = x_i \dot{N}_t - 4\pi r^2 c_t D_{i,\text{eff}} \frac{dx_i}{dr}. \tag{4.5}$$

The steady flow of heat in the boundary layer can be described by a similar equation

$$\dot{Q} = \sum_{i=1}^{n_{\text{gas}}} \dot{N}_i h_i - 4\pi r^2 \lambda \frac{dT}{dr}, \tag{4.6}$$

The enthalpy is related to temperature through the heat capacity, $c_p = (\partial h/\partial T)_p$ where the subscript $p$ denotes that the differential occurs at constant pressure. Assuming that the gas layer is at constant pressure and the heat capacity is not a function of temperature, we can integrate this equation using a reference point to find

$$h_i = h_{i,\text{ref}} + \bar{c}_{p,i}(T - T_{\text{ref}}), \tag{4.7}$$

where the heat capacity of species $i$ is evaluated at a mean temperature between $T$ and $T_{\text{ref}}$.

Equations 4.5 and 4.6 (after substitution of Eq. 4.7) can be integrated, leading to algebraic expressions describing species continuity and energy flow in unreactive section(s) of the boundary layer.

### 4.4.1 Single-film Model

In the single-film model, the entire boundary layer is unreactive, and integration of Eq. 4.5 from the radius of the particle to $\infty$ (the edge of the boundary layer), results in the expression

$$x_{i,p} = \frac{\dot{N}''_{i,p}}{\dot{N}''_{t,p}} + \left( x_{i,\infty} - \frac{\dot{N}''_{i,p}}{\dot{N}''_{t,p}} \right) e^{-\kappa_{m,i}}, \tag{4.8}$$

where

$$\kappa_{m,i} = \frac{r_p \dot{N}''_{t,p}}{c_t D_{i,\text{eff}}}, \tag{4.9}$$

is a version of the mass transfer Péclet number (the Péclet number characterizes the ratio of convective to diffusive transport).

The heat flow in the boundary layer must be balanced by the energy released from reactions in the particle, and radiation losses from the particle. The enthalpy advection term (the summation in Eq. 4.6) already accounts for the enthalpy change of the gases during heterogeneous reactions, but does not account for the enthalpy released as the solid carbon is converted to gas phase species [51]. After integration of Eq. 4.6, using the particle surface as the reference point in Eq. 4.7, a thermal energy balance is written as

$$\dot{N}''_{\mathrm{C},p} h_{\mathrm{C},p} - \epsilon\sigma\left(T_p^4 - T_w^4\right) = \sum_{i=1}^{n_{\mathrm{gas}}} \dot{N}''_i h_{i,p} + \frac{\bar{\lambda}}{r_p}\left[\frac{\kappa}{e^{\kappa}-1}\right]\left(T_p - T_\infty\right), \tag{4.10}$$

where,

$$\kappa = \frac{r_p}{\bar{\lambda}} \sum_{i=1}^{n_{\mathrm{gas}}} \dot{N}''_{i,p} \bar{c}_{p,i} \tag{4.11}$$

is a version of the heat transfer Péclet number.

### 4.4.2 Double-film Model

In the double-film model, it is assumed that an infinitely thin flame sheet exists somewhere in the boundary layer. There are two unreactive gas layers, with the unreactive layer between the particle and the flame sheet denoted as region 1, and the unreactive layer between the flame and the bulk gas (at $r = \infty$) denoted as region 2. In region 2, all of the CO and $H_2$ that were generated at the particle are assumed to have been oxidized to $CO_2$ and $H_2O$ in the flame sheet. Therefore, the only species fluxes in region 2 are oxygen towards the particle, and $CO_2$ from the particle, which must be equal (on a molar basis, because of the conservation of oxygen), requiring $\dot{N}_{t,2} = 0$. Armed with this knowledge, integration of Eq. 4.5 in the two regions yields

$$x_{i,p} = \frac{\dot{N}''_{i,p,1}}{\dot{N}''_{t,p,1}} + \left(x_{i,f} - \frac{\dot{N}''_{i,p,1}}{\dot{N}''_{t,p,1}}\right) e^{-\kappa_{m,i,1}\left(1 - r_p/r_f\right)}, \tag{4.12}$$

$$x_{i,f} = x_{i,\infty} + \frac{\dot{N}''_{i,p,2} r_f}{c_t D_{i,\mathrm{eff}}}, \tag{4.13}$$

where $\kappa_{m,i,1}$ is the same as $\kappa_{m,i}$ (Eq. 4.9), except the total molar flux is $\dot{N}''_{t,p,1}$ rather than $\dot{N}''_{t,p}$.

Integrating Eq. 4.6 in regions 1 and 2 yields

$$\dot{Q}''_{p,1} = \sum_{i=1}^{n_{\text{gas}}} \dot{N}''_{i,p,1} h_{i,p} + \frac{\bar{\lambda}_1}{r_p} \left[ \frac{\kappa_1}{e^{\kappa_1 (1 - r_p/r_f)} - 1} \right] (T_p - T_f) \,, \tag{4.14}$$

$$\dot{Q}''_{f,2} = \sum_{i=1}^{n_{\text{gas}}} \dot{N}''_{i,f,2} h_{i,f} + \frac{\bar{\lambda}_2}{r_f} \left[ \frac{\kappa_2}{e^{\kappa_2} - 1} \right] (T_f - T_\infty) \,. \tag{4.15}$$

In these equations, $\kappa_1$ is given by Eq. 4.11, where $\bar{\lambda} = \bar{\lambda}_1$ and $\bar{c}_{p,i}$ are evaluated at the mean temperature in region 1, assumed to be $(T_p + T_f)/2$. Similarly, $\kappa_2$ is also described by Eq. 4.11, where $\bar{\lambda} = \bar{\lambda}_2$ and $\bar{c}_{p,i}$ are evaluated at the mean temperature in region 2. The heat transfer by the gas in region 1 must once again be balanced by the surface reactions and radiation; assuming that the particle radiation to the surroundings is not affected by the presence of the flame,

$$\dot{N}''_{\text{C},p} h_{\text{C},p} - \epsilon\sigma \left( T_p^4 - T_w^4 \right) = \sum_{i=1}^{n_{\text{gas}}} \dot{N}''_{i,p,1} h_{i,p} + \frac{\bar{\lambda}_1}{r_p} \left[ \frac{\kappa_1}{e^{\kappa_1 (1 - r_p/r_f)} - 1} \right] (T_p - T_f) \,. \tag{4.16}$$

The gas heat transfer in region 1 must also be balanced by the gas heat transfer in region 2, or

$$r_p^2 \dot{Q}''_{p,1} = r_f^2 \dot{Q}''_{f,2} . \tag{4.17}$$

While there is no explicit term to describe heat release by the flame in this equation, the enthalpy advection terms properly account for chemical reactions. In the double-film model, the flame can be arbitrarily placed, or as suggested by Zhang et al. [73], placed to maximize the overall consumption rate of solid carbon ($\dot{N}_{\text{C}}$).

### 4.4.3 Heterogeneous Reactions

Within the char particle, reactions 4.1-4.4 are considered, and it is assumed that these reactions follow the law of mass action kinetics where each rate coefficient follows an Arrhenius expression,

$$k_j = A_{0,j} \exp\left( \frac{-E_{a,j}}{R T_p} \right) . \tag{4.18}$$

The particle is porous, and the analysis by Thiele [77] is followed, to account for reactant penetration into the pores. Assumptions include first order, irreversible reactions that are proportional to the concentration of one reacting species; a uniform particle temperature; pores are connected and can be described by a constant (average) ratio of perimeter to flow area; there is no net mass flow (Stefan flow is neglected in the pores); and, other

reactions/reactants do not affect the rates. The diffusivity of the reactants in the pores is corrected by the ratio of the void fraction to tortuosity. The overall reaction rate coefficient for oxygen is found by adding the reaction rate coefficients of reactions 4.1 and 4.2, then for each of the reactive gases, $i = O_2, CO_2, H_2O$, the Thiele modulus is calculated as

$$\mathrm{M_{T},}_{i} = r_p \sqrt{\frac{\sigma_r k_{r,i}}{\frac{\phi}{\tau} D_{i,\mathrm{eff}}}}. \tag{4.19}$$

An effectiveness factor for each of the three reactive gases is then found as

$$\eta_i = \frac{3}{\mathrm{M_{T},}_{i}} \left( \frac{1}{\tanh(\mathrm{M_{T},}_{i})} - \frac{1}{\mathrm{M_{T},}_{i}} \right). \tag{4.20}$$

For each of the four reactions, the molar flux of the reactant $i$ due to reaction $j$ at the particle surface is calculated as

$$\dot{N}''_{p,i,\mathrm{rxn}\ j} = -\eta_i k_j \left( \frac{\sigma_r r_p}{3} \right) \left( \frac{x_{i,p} P}{R T_p} \right). \tag{4.21}$$

Finally, the flux of carbon and each gas species can be calculated

$$\dot{N}''_{\mathrm{C},p} = -(2\dot{N}''_{p,\mathrm{O_2,rxn\ 4.1}} + \dot{N}''_{p,\mathrm{O_2,rxn\ 4.2}} + \dot{N}''_{p,\mathrm{CO_2,rxn\ 4.3}} + \dot{N}''_{\mathrm{H2O,rxn\ 4.4}}) \tag{4.22}$$

$$\dot{N}''_{\mathrm{O_2},p} = \dot{N}''_{p,\mathrm{O_2,rxn\ 4.1}} + \dot{N}''_{p,\mathrm{O_2,rxn\ 4.2}} \tag{4.23}$$

$$\dot{N}''_{\mathrm{CO_2},p} = \dot{N}''_{p,\mathrm{CO_2,rxn\ 4.3}} - \dot{N}''_{p,\mathrm{O_2,rxn\ 4.2}} \tag{4.24}$$

$$\dot{N}''_{\mathrm{CO},p} = -2\dot{N}''_{p,\mathrm{O_2,rxn\ 4.1}} - 2\dot{N}''_{p,\mathrm{CO_2,rxn\ 4.3}} - \dot{N}''_{p,\mathrm{H2O,rxn\ 4.4}} \tag{4.25}$$

$$\dot{N}''_{\mathrm{H_2O},p} = \dot{N}''_{p,\mathrm{H_2O,rxn\ 4.4}} \tag{4.26}$$

$$\dot{N}''_{\mathrm{H_2},p} = -\dot{N}''_{p,\mathrm{H_2O,rxn\ 4.4}} \tag{4.27}$$

Note that for the double-film model, these are the species fluxes in region 1, and the species fluxes in region 2 are

$$\dot{N}''_{\mathrm{O_2},f,2} = -\frac{r_p^2}{r_f^2} \dot{N}''_{\mathrm{C},p,1} \tag{4.28}$$

$$\dot{N}''_{\mathrm{CO_2},f,2} = \frac{r_p^2}{r_f^2} \dot{N}''_{\mathrm{C},p,1} \tag{4.29}$$

### 4.4.4 Solution Procedure

The fluxes described by Eqs. 4.22-4.27 are dependent on the mole fractions of $O_2$, $CO_2$, and $H_2O$ at the particle surface as well as the particle temperature. To solve for the mole fractions at the particle surface (Eq. 4.8 for the single-film model or Eq. 4.12 for the

double-film model) or the particle temperature (Eq. 4.10 for the single-film model or Eq. 4.16 for the double-film model), the species and carbon fluxes must be known. A damped-Newton method is used to simultaneously solve these equations. Initially, predictions are made for mole fractions and temperature at the particle surface (and the flame, in the case of the double-film model). From this, the species fluxes and properties are calculated, and the mole fractions and temperatures at the particle surface (and the flame, in the case of the double-film model) are recalculated. Newton's method is used to calculate a correction step on the mole fractions and temperatures. Damping on the correction step occurs when the corrected solution is outside the bounds (the mole fractions are constrained to lie between 0 and 1, and the particle temperature must be less than 6000 K). The solution is considered converged when the normalized error in mole fractions and temperatures are below a given tolerance.

The double-film model requires an additional solver to determine the radius of the flame. A Nelder-Mead simplex algorithm, as implemented in SciPy [78], is used to find the radius of the flame where the carbon consumption rate is maximized.

## 4.5 Results and Discussion

To compare the models, the reaction mechanism specified in Table 4.1 was implemented in both the single-film and double-film models described previously. Because Surface CHEMKIN [31] is used by SKIPPY to determine reaction rates, the pre-exponential factors, $A$, were multiplied by the density of carbon sites (given in the caption of Table 4.1) to determine the pre-exponential factor, $A_0$, for use in the simplified models. The same char parameters shown in Table 4.2 were also used in each of the models.

Typical profiles of the temperature and mole fractions within the particle and in the boundary layer are shown in Fig. 4.1, for combustion with 24 vol-% $O_2$ in the bulk gas, 14% $H_2O$, and either $CO_2$ as a diluent gas (to model oxy-combustion conditions), or $N_2$ as a diluent (with 4% $CO_2$ in the bulk gas, which is closer to air-fired combustion conditions). In the figure, SKIPPY results are referred to as the continuous-film model, where reactions occur throughout the boundary layer (and within the pores of the particle). Results labeled 'no homogeneous chemistry' are also SKIPPY results, where gas-phase chemistry has been turned off. This result reduces SKIPPY to a single-film model (and neglects any homogeneous chemistry in the particle pores). The agreement between the SKIPPY results without homogeneous chemistry and the single-film model confirms that SKIPPY is reduced

**Table 4.2**. Properties for the base-case simulations, which are the same as the sub-bituminous char studied by Geier et al. [56] and as assumed in the simulations by Hecht et al. [17, 28].

| | |
|---|---|
| diameter | 100 $\mu$m |
| bulk density | 560 kg/m$^3$ |
| thermal conductivity | 1.33 W/m $\cdot$ K |
| (inert) ash content | 3% |
| tortuosity | 5 |
| void fraction | 0.4 |
| specific surface area | $1 \times 10^4$ m$^2$/kg |
| gas temperature | 1690 K |
| wall temperature | 500 K |
| emissivity | 0.8 |

**Figure 4.1**. Comparison temperatures and mole-fractions of gas phase species in the particle and in the boundary layer for the 100 $\mu$m particle characterized by Table 4.2. Results are for the single-film, double-film, and SKIPPY models. Thick, solid gray line is SKIPPY with all chemistries; thin, solid blue line is SKIPPY without gas-phase chemistry. The diluent gas on the following page is $CO_2$ and on the second following page is $N_2$. Both plots have 14 vol-% $H_2O$ and 24% $O_2$ in the bulk gas. $N_2$ diluent includes 4% $CO_2$ in the bulk gas.

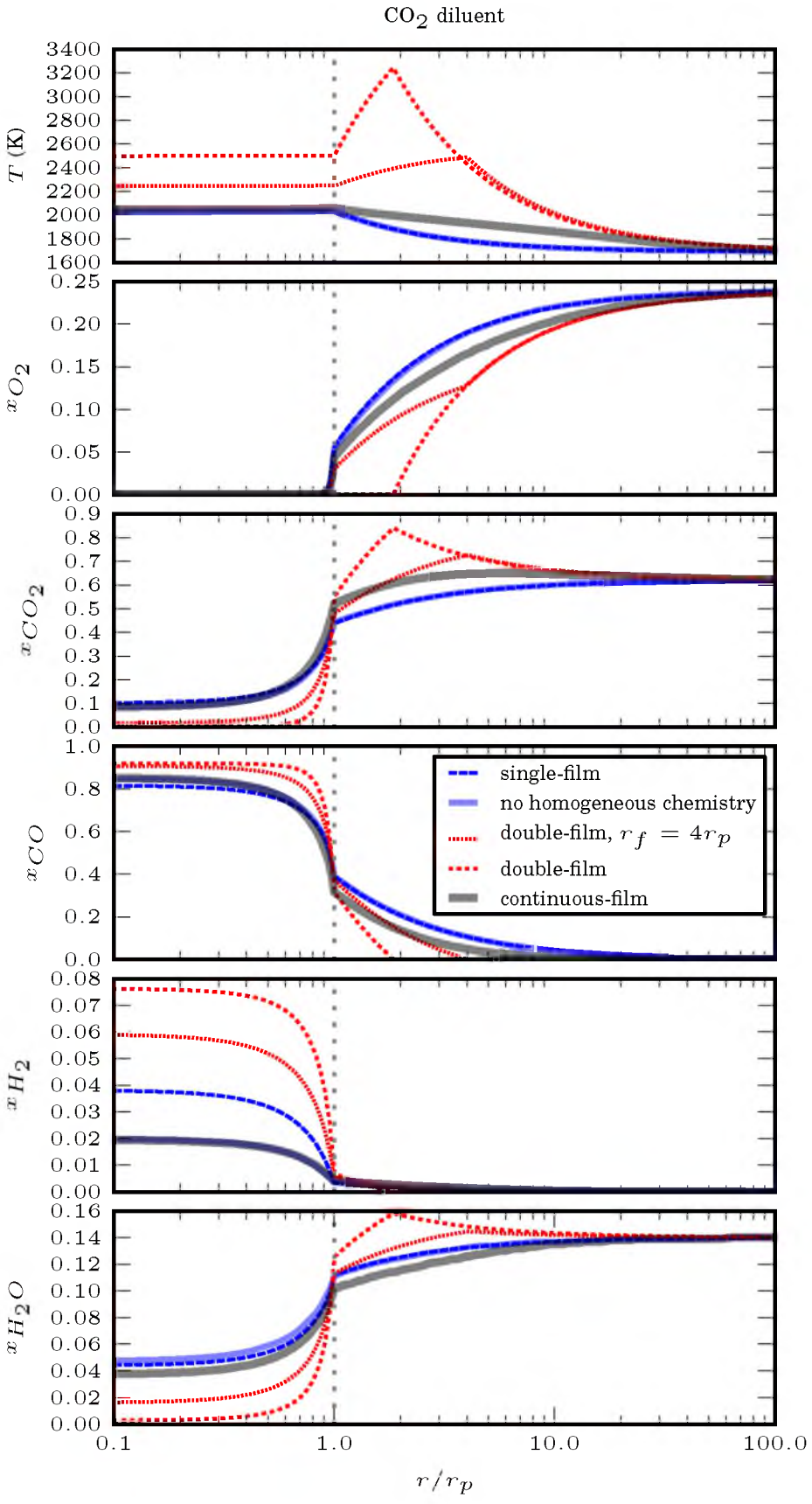
$CO_2$ diluent
$T$ (K)
$x_{O_2}$
$x_{CO_2}$
$x_{CO}$
$x_{H_2}$
$x_{H_2O}$
single-film
no homogeneous chemistry
double-film, $r_f = 4r_p$
double-film
continuous-film
0.1
1.0
10.0
100.0
$r/r_p$

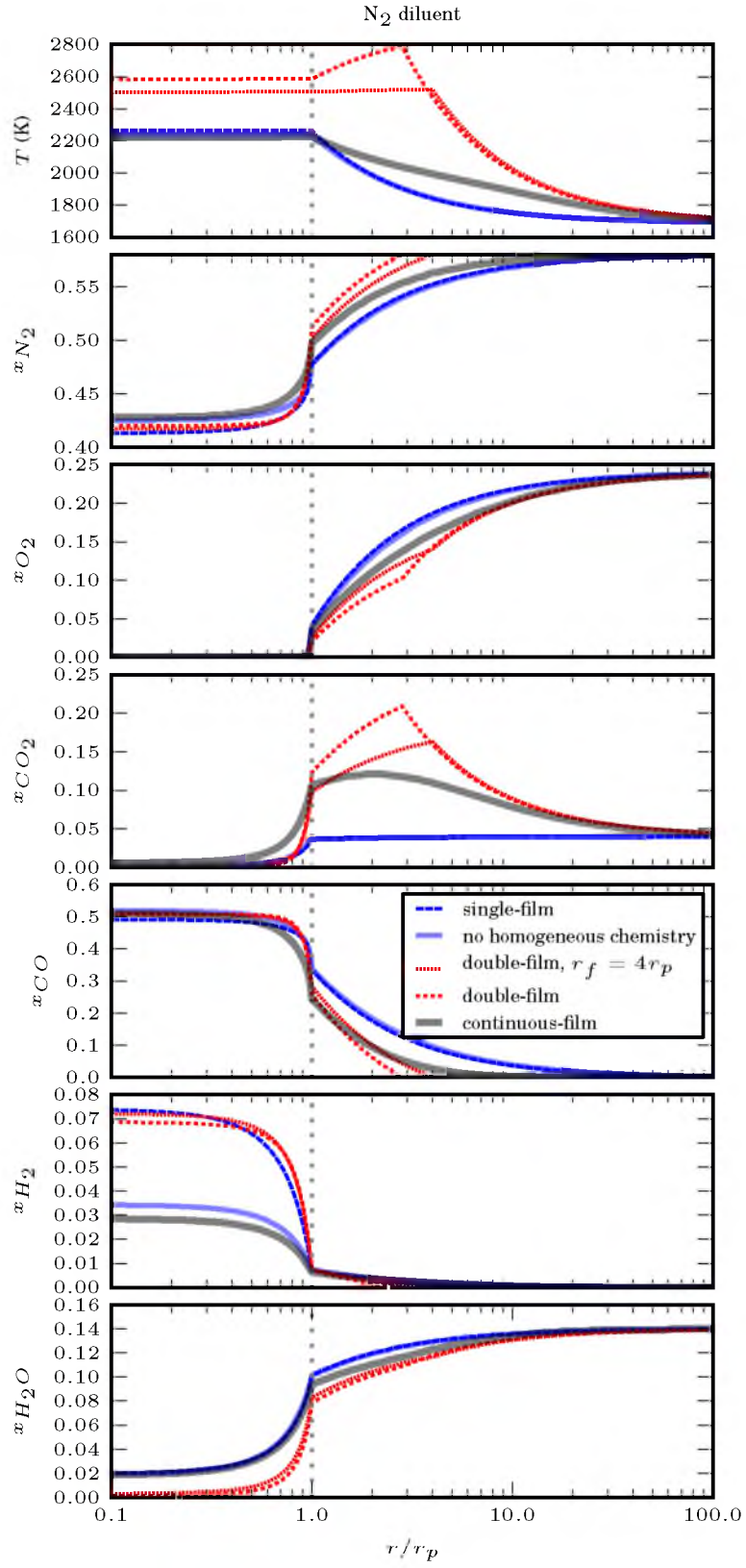


**Figure 4.1**. Continued.

to a single-film model when the homogeneous chemistry is turned off. Small differences in temperatures and mole fractions are due to the simplifications made in the single-film model. One simplification is that an effective diffusivity rather than a multicomponent diffusion description allowed the species diffusion equations to be decoupled. Secondly, diffusivity and other transport properties are evaluated at a mean temperature, which may not be representative of the entire boundary layer temperature. Finally, the Thiele description for reactant penetration is only valid for one species reacting in a cylindrical pore, whereas in these simulations, three species are reacting with the solid carbon, and $CO_2$ is both a product and a reactant. Nonetheless, under these conditions, the two models agree well.

The double-film and continuous-film models also show some similar trends. Reactions in the boundary layer release heat. For the continuous-film model, the temperature still decays away from the particle surface, but is higher than the single-film model temperatures throughout the boundary layer. Meanwhile, the double-film model has a temperature peak at the flame-front. Boundary layer reactions increase the concentration of $CO_2$ and decrease the concentration of $O_2$ available to react at the particle surface. These reactions also drive the concentrations of $H_2$ and CO to zero at a point closer to the particle surface than the single-film models.

Char combustion models must accurately predict carbon consumption rates, in addition to char particle temperatures, so that the burnout of the char can be predicted. Figure 4.2 shows the particle temperatures and carbon consumption rates for the same 100 $\mu$m particle as a function of bulk oxygen concentration. Both the particle temperatures and carbon consumption rates increase as the oxygen concentration increases. The temperatures and carbon consumption rates predicted by the continuous-film model (which is the most physically accurate) are most closely matched by the single-film model over the entire range of conditions studied here. The SKIPPY model without homogeneous chemistry agrees well with the full SKIPPY model at low oxygen concentrations, but both the temperature and carbon consumption rates begin to diverge at the higher oxygen concentrations.

The two double-film model results shown in Figs. 4.1 and 4.2 are the same model with two placements of the flame sheet. One result is where the flame sheet is somewhat arbitrarily placed at $4r_p$, and the other, labeled simply 'double-film', follows the suggestion of Zhang et al. [73] in placing the flame sheet in the position that maximizes the carbon consumption rate. When $CO_2$ is the diluent, this approach causes the flame sheet to be located where it would in a classical double-film model, at the point where the $O_2$ is completely consumed in the boundary layer, and $CO_2$ and $H_2O$ are the only species consuming the carbon. When $N_2$

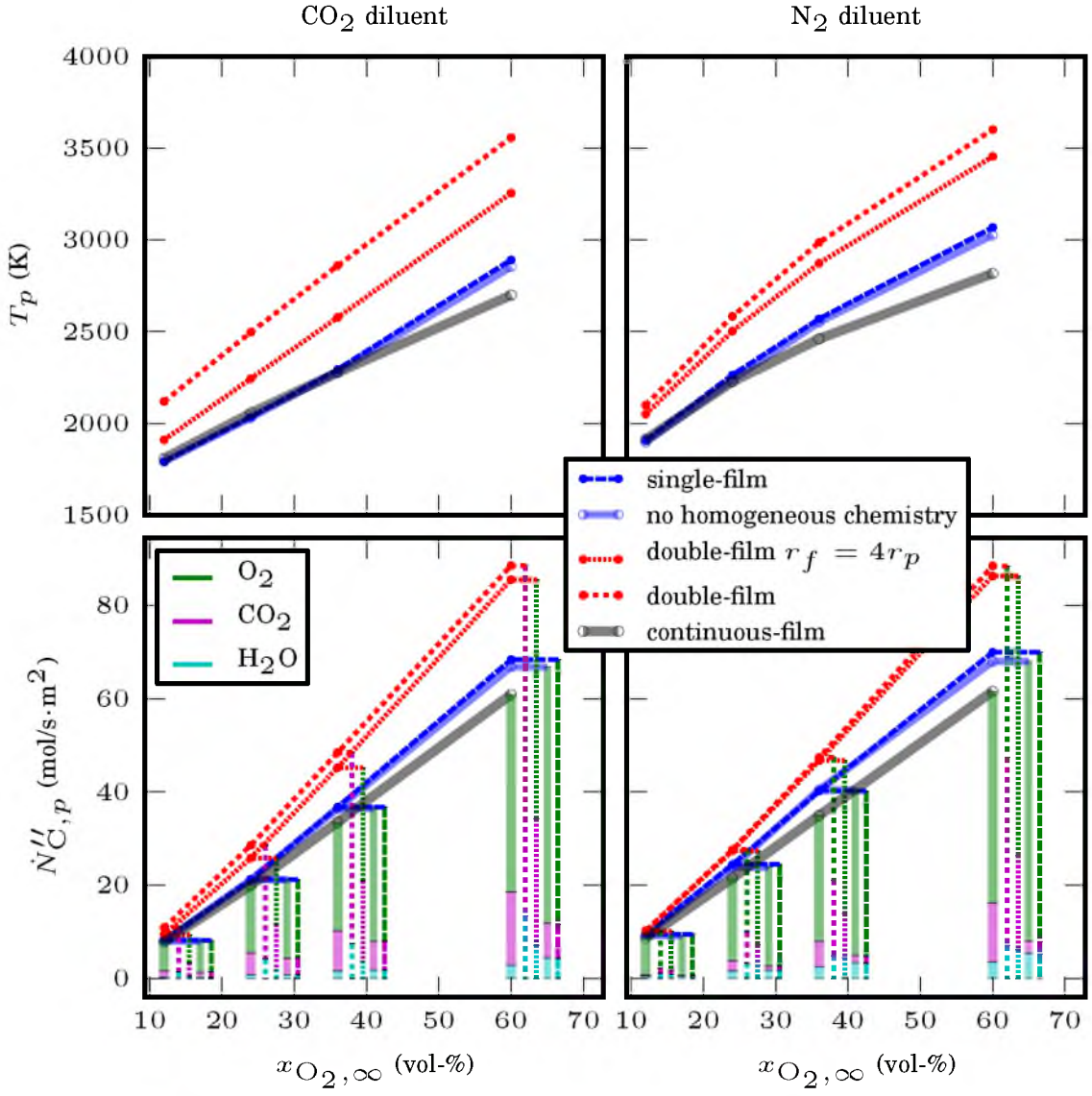


**Figure 4.2**. Particle temperatures (top) and carbon fluxes at the particle surface (bottom) predicted by the different models for the 100 $\mu$m particle characterized by Table 4.2. Frames on the left are for the $CO_2$ diluent and frames on the right are for the $N_2$ diluent. In the bottom frames, the bars leading up to the data points with the same line style show the portion of carbon consumption attributed to the gasifiying species shown in the legend ($O_2$, $CO_2$, or $H_2O$).

is the diluent, the maximum carbon consumption rate occurs when the flame sheet is further from the particle, and $O_2$ is not completely consumed in the boundary layer. Regardless of where the flame sheet is placed in the boundary layer, the particle temperatures and total carbon consumption rates predicted by the double-film model are significantly higher than those predicted by the continuous-film model. Maximizing the carbon consumption rate in the double-film model causes even higher particle temperatures and carbon consumption rates than when the radius of the flame is four times the radius of the particle. The flame sheet, wherein CO and $H_2$ are oxidized, transfers significant heat to the particle. Although the mole fraction of $O_2$ at the particle surface decreases and the mole fractions of $H_2O$ and $CO_2$ increase, causing the gasification reaction rates to increase and the oxidation reaction rate to decrease, the endothermic gasification reactions do not consume enough heat to reduce the particle temperature back to where it would be without the flame sheet in the boundary layer. Moving the flame sheet further out in the boundary layer causes the predicted particle temperatures to decrease until eventually, the predictions between the single and double-film models are identical.

A careful inspection of the lower panels of Fig. 4.2 elucidates the species responsible for the carbon consumption. With the exception of the double-film model, the majority of carbon consumption is due to $O_2$, followed by $CO_2$, and then $H_2O$ across the range of oxygen concentrations in the bulk gas. $CO_2$ is responsible for the majority of the carbon consumption for the double-film model, when $CO_2$ is the diluent, and a large fraction for the $N_2$ diluent. The fraction of consumption by $CO_2$ is also larger for the continuous-film and double-film model where $r_f = 4r_p$, than for either version of the single-film models. Boundary-layer reactions, when accounted for, generate significant quantities of $CO_2$ as CO is oxidized. Consequently, the flux of $CO_2$ to the particle, and the mole fraction of $CO_2$ at the particle surface, increases, while the $O_2$ flux and concentration at the particle decreases, due to $O_2$ utilization in the boundary layer. The net effect is a greater proportion of carbon consumption attributed to $CO_2$, but a similar overall carbon consumption rate prediction as when boundary layer reactions are neglected.

Since the gasification reactions are endothermic, one might expect the particle temperature to be lower when boundary layer reactions are active and a larger portion of carbon consumption is due to $CO_2$ gasification. In fact, the heat released by the CO and $H_2$ oxidation in the boundary layer feeds back to the particle and the temperatures predicted by the double-film model are higher than those predicted by the single-film model. When the heat release in the boundary layer is spread out over a larger distance, as

in the continuous-film model, the temperatures predicted are slightly higher than those predicted by the single-film models at low oxygen concentrations, but lower at high bulk $O_2$ concentrations, highlighting the complexities in these models.

As another parametric study, Fig. 4.3 shows the temperatures and carbon consumption rates as a function of particle size for three bulk oxygen concentrations. The double-film model with a maximized carbon consumption rate has been omitted from this plot, due to the large deviations from the continuous-film model. Smaller particles burn at higher temperatures, and have a higher flux of carbon (although it should be noted that the flux is normalized to the external surface area of the particle, $4\pi r_p^2$, and the flow rate of carbon (mol/s) actually increases as the diameter increases). Although there are endothermic gasification reactions along with the exothermic oxidation reactions, the net result of heterogeneous chemistry is exothermic. Smaller particles have larger effectiveness factors, and subsequently higher reaction rates. This causes the larger carbon consumption rate and higher temperatures for smaller particles. A comparison of the particle temperatures in $N_2$ and $CO_2$ diluent environments shows consistently higher temperatures for all particle sizes and for all models in $N_2$ environments, because of the reduced contribution of the endothermic $CO_2$ gasification reaction and the higher diffusivity of oxygen through nitrogen as compared to $CO_2$ [6].

Across the range of sizes (60-135 $\mu$m) and bulk oxygen concentrations (24-60%), of the two simplified models, the single-film model predicts both carbon consumption rates and particle temperatures that are more similar to continuous-film model predictions. There is also very little difference between the single-film model and SKIPPY model without homogeneous chemistry, confirming that the simplifications regarding the effectiveness factor and gas diffusion are reasonable. The errors between the single-film models and the full SKIPPY model are larger with nitrogen as a diluent as compared to $CO_2$ and as the bulk $O_2$ concentration increases, but the differences between the models are not a strong function of particle size. The largest error in temperature between the single-film model and the continuous-film model is 270 K for a 60 $\mu$m particle with 60% $O_2$ in the bulk gas and $N_2$ as the diluent. The largest relative error in carbon consumption rate between the single-film and continuous-film models is 15.3% for a 135 $\mu$m particle with 36% $O_2$ in the bulk gas and $N_2$ as the diluent.

A base surface area of 10 $m^2/g$ was used for all of the previous simulations because this surface area approximately corresponds to the sum of macropore and mesopore surface area that is most likely accessible under high temperature reacting conditions [58, 59],

**Figure 4.3**. Particle temperatures and carbon consumption rates for the models as a function of particle size. Bulk oxygen concentration increases from top to bottom, as listed in the top of each frame. $CO_2$ diluent results are in the left frames, and $N_2$ diluent results in the right. Line colors and styles match those in Fig. 4.2.

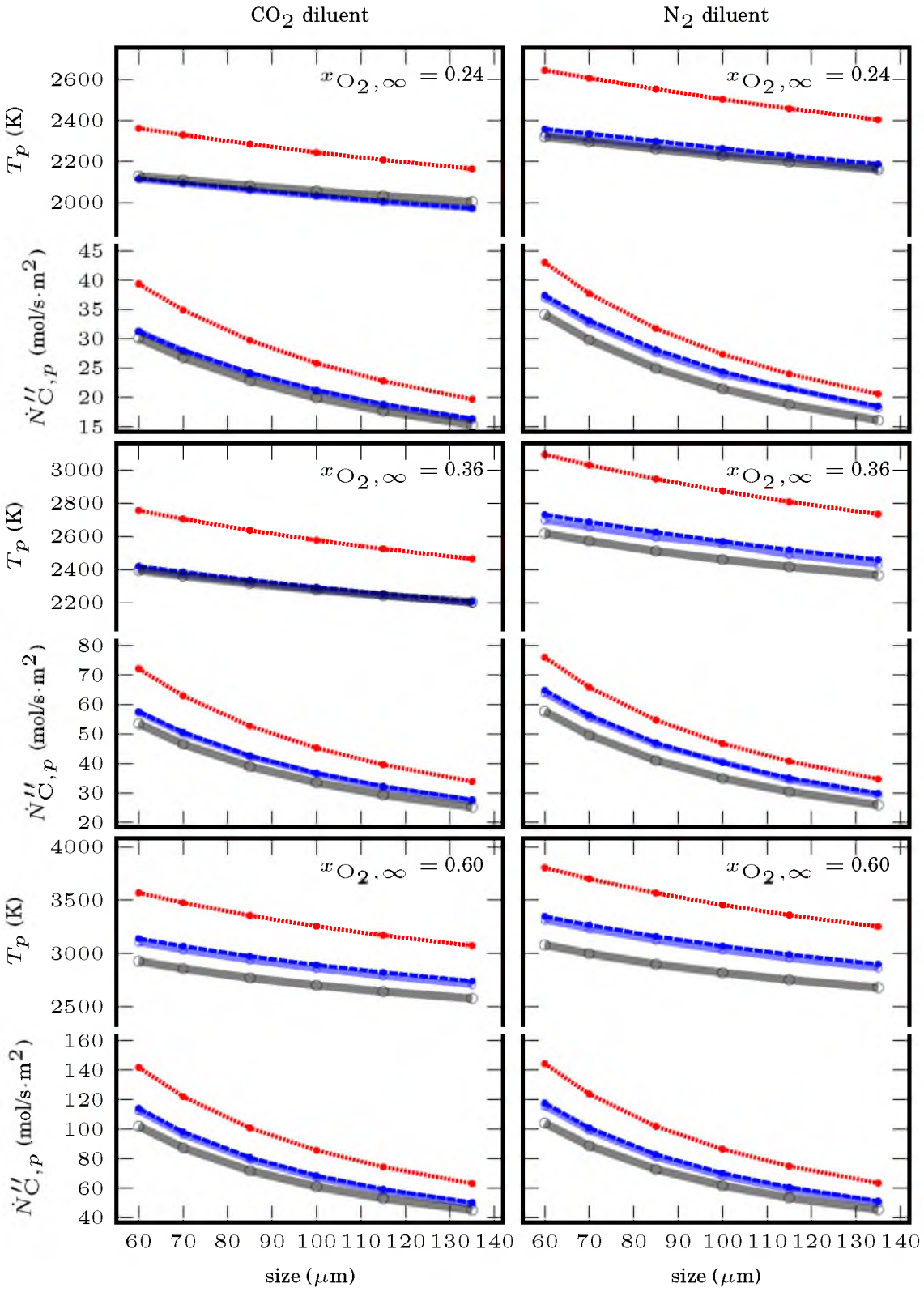
CO2 diluent
N2 diluent
$x_{O_2,\infty} = 0.24$
$x_{O_2,\infty} = 0.36$
$x_{O_2,\infty} = 0.60$
$T_p$ (K)
$\dot{N}''_{C,p}$ (mol/s·m$^2$)
size ($\mu$m)

and also because use of this surface area in the continuous film model has been shown to yield accurate char particle combustion temperature estimates when using the reaction mechanism listed in Table 4.1 [28]. There is considerable uncertainty in this value of surface area, as well as uncertainty in the literature as to how the development of surface area and/or reactivity affect the burning rate of char as burnout progresses [57]. Variations in surface area affect the burning rates in the same manner as changing the pre-exponential factors (although this changes the pre-exponential factors for oxidation and gasification rates by equal percentages), as the reaction rate coefficients shown in Eqs. 4.19 and 4.21 are multiplied by the specific surface area. Figure 4.4 shows the particle temperatures and carbon consumption rates predicted by the two simplified and continuous-film models as a function of specific surface area for three particle sizes.

Generally, the particle temperatures decrease slightly as the surface area increases. At 10 $m^2/g$, $O_2$ has very limited penetration, while $CO_2$ and $H_2O$ penetrate significantly into the particle (see Fig. 4.1 for two examples of reactant penetration). As the surface area decreases, the oxygen penetrates further into the particle, and while $CO_2$ and $H_2O$ also diffuse further into the particle, the carbon consumption from oxygen becomes relatively more important than the consumption from the other two reactants, which is evident in the bottom of the frames in Fig. 4.4. Although the overall carbon consumption rate decreases for a smaller surface area, because the contribution from $O_2$ increases (which is an exothermic reaction), the temperature at 1 $m^2/g$ is generally similar to, if not higher than, that at 10 $m^2/g$. Increasing the specific surface area to 100 $m^2/g$ tends to have the opposite effect. For a high specific surface area, the gasification reactions with $CO_2$ and $H_2O$ consume a larger fraction of the carbon, and the endothermicity of these reactions brings the particle temperature down. However, the increasing the proportion of carbon consumption from gasification reactions as the surface area increases does not always decrease the particle temperatures. For small particles in 24 and 36% $O_2$, there are several cases where an increase in particle temperature is predicted as the surface area increases from 1 to 10 $m^2/g$. In these cases, the gains in overall carbon consumption rate outweigh the decrease in oxidation relative to gasification and the particle temperature increases with increasing surface area. A comparison of the three particle sizes shown in Fig. 4.4 also reveals that smaller particles tend to burn at higher temperatures, and have a higher flux of carbon–the same trend that was shown and discussed in relation to Fig. 4.3.

Across the range of parameters varied in these simulations, the single-film model once again has a higher degree of correlation to the continuous-film model than the double-film

**Figure 4.4**. Temperatures and carbon consumption rates as a function of specific surface area. The three sets of frames to the left are for a $CO_2$ diluent, and the three frames to the right for the $N_2$ diluent for different sizes of particles, as labeled at the top. The oxygen concentration in the bulk gas increases from top to bottom, as listed in each frame. Line colors and styles match those in Fig. 4.2.

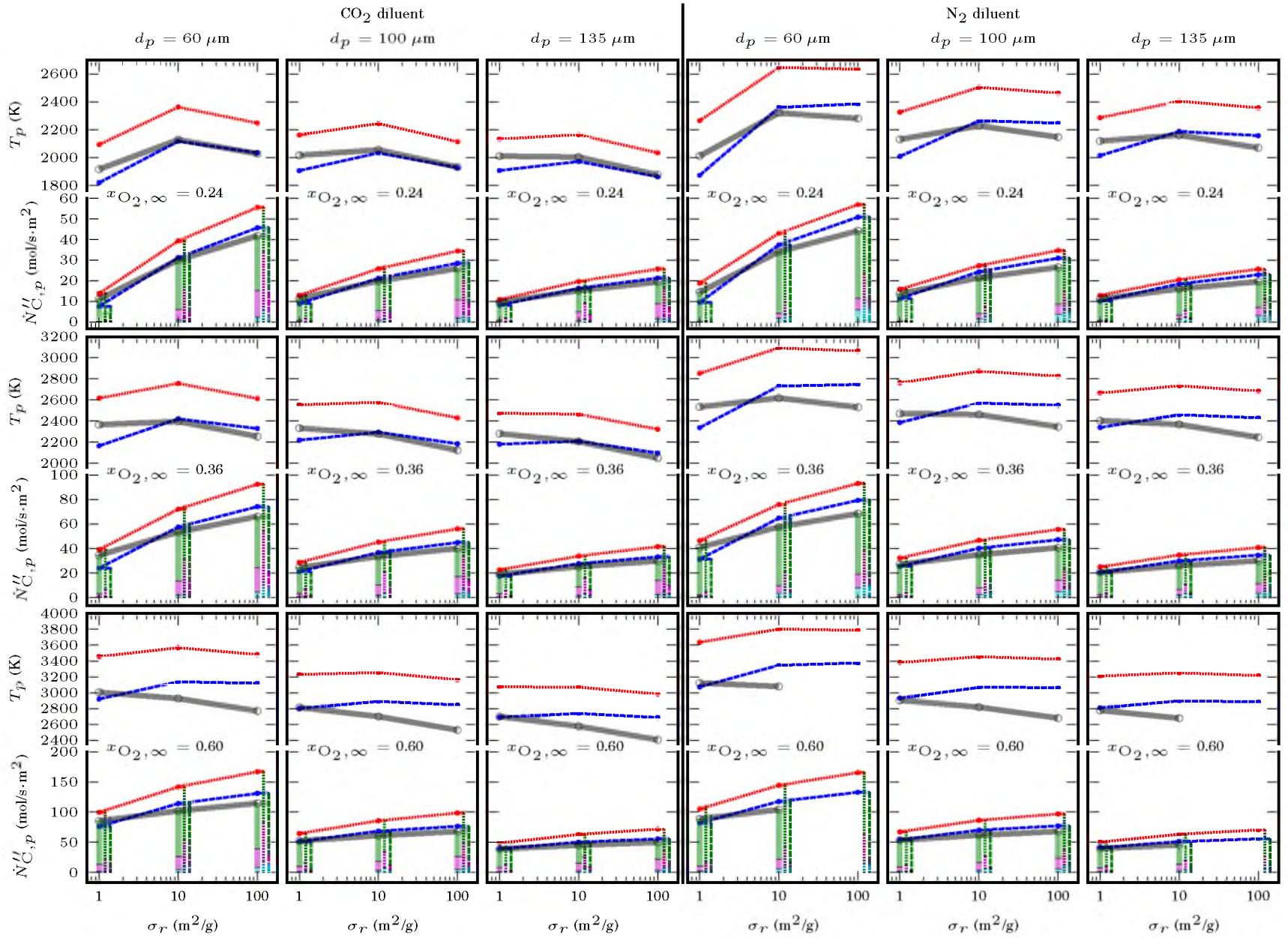
$CO_2$ diluent
$N_2$ diluent
$d_p = 60\ \mu$m
$d_p = 100\ \mu$m
$d_p = 135\ \mu$m
$T_p$ (K)
$\dot{N}''_{C,p}$ (mol/s·m$^2$)
$x_{O_2,\infty} = 0.24$
$x_{O_2,\infty} = 0.36$
$x_{O_2,\infty} = 0.60$
$\sigma_r$ (m$^2$/g)

model. As before, the single-film model results show a better correlation to the continuous-film results when $CO_2$ is the diluent gas than when $N_2$ is the diluent. The largest difference in temperature between the single- and continuous-film models is 386 K for a 100 $\mu$m particle with a specific surface area of 100 $m^2/g$ in $N_2$ diluent and 60% $O_2$ in the bulk gas. The largest relative error in carbon consumption rate is 34.2% for a 60 $\mu$m particle with a specific surface area of 1 $m^2/g$ in $N_2$ diluent and 24% $O_2$ in the bulk gas.

## 4.6 Modeling Implications

The single-film model presented in this work includes gasification reactions, Stefan flow, and intraparticle diffusion (reactant penetration), factors which are often omitted from single-film models [56]. Gasification reactions reduce the combustion temperature by up to a few hundred degrees (depending on the combustion conditions), but increase the carbon consumption rate by up to 12% [17, 28]. The oxidation kinetics for a given coal could potentially be adjusted to account for the lack of gasification reactions in a model, but the applicability range of the model in terms of combustion environments and particle sizes would be severely limited. Since each of Rxns. 4.1, 4.3, and 4.4 produce two moles of gas for every one mole of reactant, it is important to include Stefan flow in a single-film analysis. For a 100 $\mu$m particle, the mass-transfer Péclet number, $\kappa_{m,i}$ ranges from 0.02, for hydrogen for a particle in 12% $O_2$, to 0.66, for $CO_2$ for a particle in 60% $O_2$. Similarly, the heat transfer Péclet number, $\kappa$, ranges from 0.06 to 0.39, as the bulk oxygen mole fraction ranges from 0.12 to 0.6. At low oxygen concentrations, diffusion dominates relative to convection due to slow reaction rates, as the low Péclet numbers show. As the reaction rates increase, with high temperatures caused by high $O_2$ concentrations, convection becomes important and Stefan flow cannot be neglected. The effect of Stefan flow on the single-film model was interrogated by setting the the total molar flowrate in Eq. 4.5 to zero and integrating throughout the boundary-layer, and setting the heat-transfer Péclet number to zero in Eq. 4.10. For a 100 $\mu$m particle with $N_2$ as a diluent, the particle temperatures are higher by 25 K than the single-film model with Stefan flow in 12% $O_2$ and higher by 540 K in 60% $O_2$. The carbon consumption rates are also over-predicted by up to 17% when Stefan flow is not properly accounted for.

Models that discount reactant penetration require apparent rather than intrinsic reaction rate coefficient pre-exponentials, reaction orders, and activation energies. In an apparent kinetic model, the reaction order is related to the intrinsic reaction order as $(n_{\text{intrinsic}}+1)/2$,

and the activation energy is half of the intrinsic activation energy [79]. An apparent single-film model that neglects reactant penetration and relies on apparent kinetics was formulated by redefining the flux of the reacting species at the surface (Eq. 4.21) as

$$\dot{N}''_{p,i,\text{rxn } j} = -k_{j,\text{app}} \left( \frac{x_{i,p} P}{R T_p} \right). \tag{4.30}$$

Note that because the intrinsic reaction order was one for each of the reactants, the apparent reaction order is also one. The apparent reaction rate, $k_{j,\text{app}}$, has an activation energy of half the intrinsic activation energy. The top frames of Fig. 4.5 show the pre-exponential factors required to match the particle temperatures and carbon consumption rates found by the intrinsic single-film model that includes reactant penetration. As the bulk oxygen concentration increases from 12-60%, the pre-exponential factors required to match the particle temperatures and carbon consumption rates predicted by the intrinsic single-film model also increase, by up to a factor of 4.8, for the steam gasification reaction (Rxn. 4.4) in $CO_2$. Although the variation required in the pre-exponential factors are large, the errors in temperature and carbon consumption rates shown in the bottom two frames of Fig. 4.5 are fairly small, when the apparent pre-exponential factors are fixed. The particle temperature predicted by the apparent model is 55 K higher than the intrinsic model with 12% $O_2$ in the bulk gas and 25 K lower with 60% $O_2$ in the bulk gas when $CO_2$ is the diluent. Very little differences in carbon consumption rates (and the relative contributions to carbon consumption rates from the three reactants) between the intrinsic and apparent kinetic models are shown in the bottom frames of Fig. 4.5. The maximum relative error in carbon consumption rates between the apparent and intrinsic single-film models is 22%, for the char particle burning in 12% $O_2$ and the $CO_2$ diluent. Neglecting reactant penetration and using apparent kinetics may, therefore, be an acceptable assumption. However, if a transient surface area or pore development model is used, an intrinsic model is better suited to capture the effects of reactant penetration with fixed kinetic parameters.

There are several facets of char combustion that are not included in the single-film model described here. First, the particles are assumed to be spherical, which is often not the case for coal char particles, and even less likely for biomass derived chars. Aris demonstrated that a shape factor defined as the ratio of the particle volume to external surface area is sufficient to describe reactant penetration for a steady-state heat and mass-transfer analysis [80], but warns that a more rigorous derivation of a shape factor is needed to describe transient heat and mass-transfer to irregularly shaped particles [81]. Secondly, catalytic and dilution effects from ash are ignored. Murphy and Shaddix show that the loss of reactivity as burnout progresses and low apparent activation energies can be largely attributed to ash effects [79].

**Figure 4.5**. Top frames show the pre-exponential factors required by the apparent kinetic model required to match the temperatures and carbon consumption rates (for each of the three reactants) predicted by the intrinsic single-film model for a 100 $\mu$m char particle. Middle and bottom frames are the temperature and carbon consumption rates for the apparent and intrinsic models, where the pre-exponential factors for the apparent kinetic model are 3900, 210, 3100, 1200 m/s for Rxns. 4.1-4.4, respectively. $CO_2$ diluent results are in the left frames, and $N_2$ diluent results in the right. Line colors and styles match those in Fig. 4.2, or are shown in the legends.

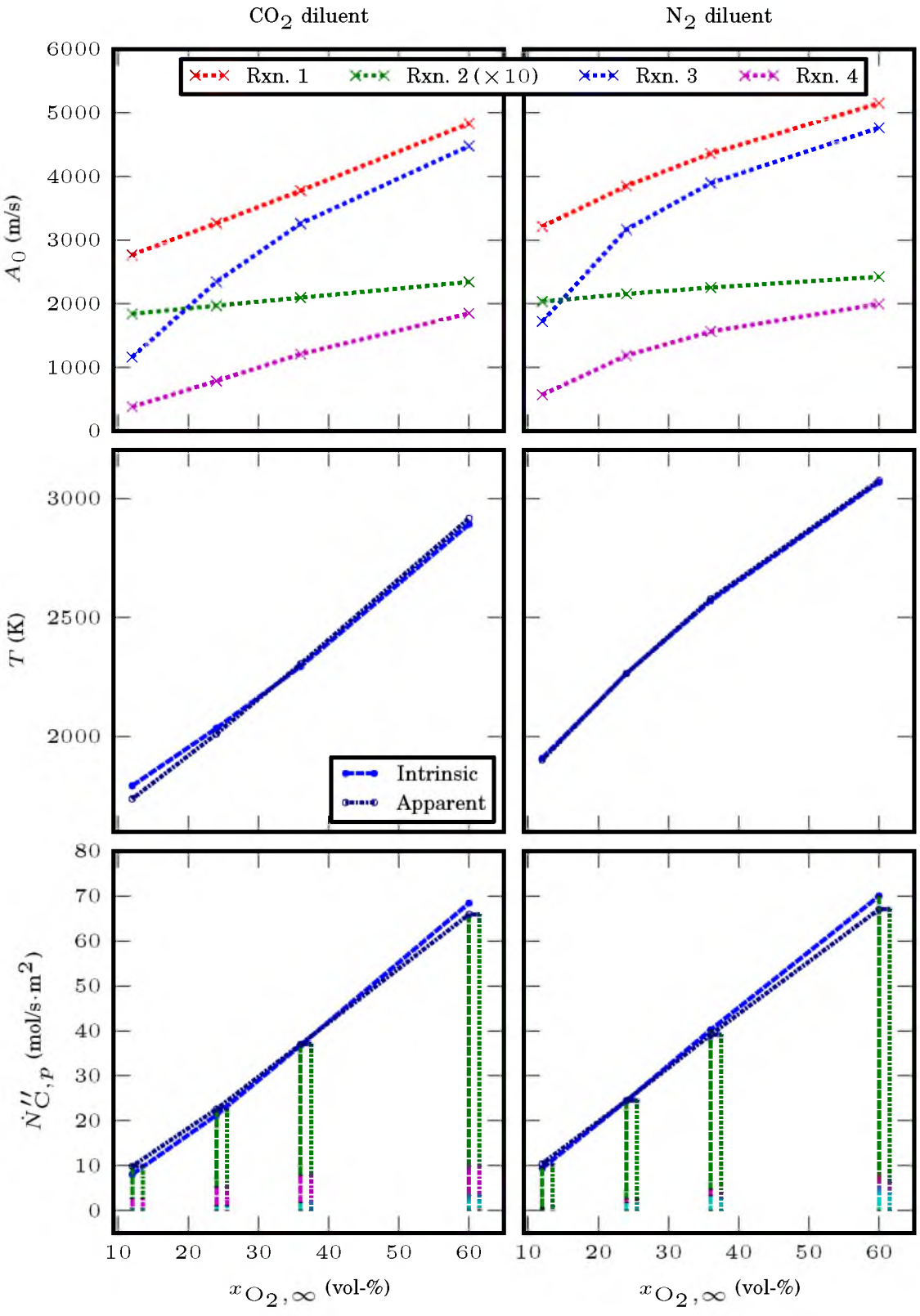
CO2 diluent
N2 diluent
Rxn. 1
Rxn. 2 (×10)
Rxn. 3
Rxn. 4
A0 (m/s)
T (K)
Intrinsic
Apparent
ṅ''C,p (mol/s·m2)
x O2,∞ (vol-%)
x O2,∞ (vol-%)

Finally, the single-film model presented here is steady-state and for a single particle. In a more applied CFD simulation, this submodel would need to include transient, thermal inertia terms, account for particle-particle interactions, distortions in the boundary-layers surrounding each particle, and potentially include gas radiation, which can be important in environments with high concentration of $CO_2$ and steam.

## 4.7 Conclusions

Many common assumptions are made when pulverized char combustion is modeled. These assumptions are necessary to reduce computational complexity and solve the governing equations for a large number of particles reacting in complex flows. Single- and double-film models have been compared to a continuous-film model for combustion of a single, steady-state particle in this analysis. In the single-film model, reactions do not occur in the boundary layer, while the double-film model accounts for homogeneous reactions by assuming there is an infinitely thin flame sheet that converts any CO to $CO_2$ and any $H_2$ to $H_2O$. The continuous-film model requires discretization of the boundary layer of a single particle. While this provides an accurate physical description of char combustion, this model is too computationally intensive to be used as a submodel in a CFD simulation.

As implemented here, both the single- and double-film models use an effectiveness factor as a function of the Thiele modulus to describe reactant penetration. Each of the models includes reactions of coal char with $O_2$, $CO_2$, and $H_2O$. All three of these reactions are required to match particle temperatures and carbon consumption rates over a wide range of gas conditions spanning from traditional air-fired combustion conditions to oxygen enhanced air and oxy-combustion conditions.

As compared to the double-film model, the single-film model predicts particle temperatures and carbon combustion rates that are much closer to those predicted by the continuous-film model. When the heat release occurs at an infinitely thin flame sheet, as it does in the double-film model, the particle temperatures and carbon consumption rates are over-predicted. When a 60-135 $\mu$m particle is reacting in 60% $O_2$, at a temperature around 2800 K, neglecting gas-phase reactions (as the single-film model does) causes an error in temperature prediction of no more than 270 K, with lower errors when the particle reacts in lower concentrations of oxygen, or with $CO_2$ as the diluent. The errors in carbon consumption rate from neglecting gas-phase reactions is estimated to be no more than 15.5%, over the range of sizes (60-135 $\mu$m) and oxygen concentrations (12-60%) studied here.

As the specific surface area is varied by an order of magnitude, errors in particle temperature predictions and carbon consumption rates between the single- and continuous-film models increase. Errors in temperature could reach 390 K and errors in carbon consumption rates could reach nearly 35% as the surface area varies. Conversely, the use of an intrinsic kinetics description of a single-film model is not seen to offer any substantial benefit over a comparable apparent kinetics model.

A single-film model that includes reactions of carbon with $O_2$, $CO_2$, and $H_2O$ is an appropriate model to describe pulverized coal char combustion over a wide range of conditions. There are inevitable errors associated with the assumptions made by the single-film model, which have been quantified in this analysis for a calibrated oxidation-gasification mechanism of char combustion. This information can be used to guide single-particle data analysis and evaluate the errors associated with a CFD submodel using this description of char combustion.

# CHAPTER 5

# EXPERIMENTAL DESCRIPTION

As mentioned in Chapter 1, the devolatilization conditions can affect the resultant char properties, such as surface area and pore size. The properties are dependent on the particle heating rate and peak temperature experienced during devolatilization, but neither the reactivities [82] or char properties [26] are strongly dependent on the presence of $N_2$ versus $CO_2$ in the bulk gas. Nonetheless, since we are interested in determining and comparing char kinetics in this work, the first step involved devolatilizing the pulverized coals in a consistent environment to create chars with consistent properties. Devolatilization took place in a drop tube furnace at the University of Utah. The furnace was operated at 1200 °C while flowing 15 SLPM nitrogen with approximately 1 vol-% oxygen to burn off any tars that might be generated during devolatilization. The furnace has an ID of 5 cm and a heated length (with temperatures between 1000 and 1200 °C) that is about 60 cm long. This led to a residence time of about 0.9 sec. Chars were collected and then sieved into 6 narrow size bins (53-63 $\mu$m, 63-75 $\mu$m, 75-90 $\mu$m, 90-106 $\mu$m, 106-125 $\mu$m, and 125-150 $\mu$m) before further experiments were performed.

There are a wide range of experimental configurations described in the literature, as summarized by Buhre et al. [5] and Chen et al. [6], from the bench scale up to the pilot scale. In this work, measurements on single, reacting char particles were desired, and the optically accessible laminar entrained flow reactor at Sandia National Laboratories was used to make these measurements. The reactor has been described previously [13], and a sketch of the setup is shown in Fig. 5.1. As shown, particles are fed into the center of a flat-flame burner that creates the high temperature reaction environment. The particles react as they travel upwards in a quartz chimney. A laser scatters off particles when they are in the focal plane of the collection optics. When the scattered laser light travels through a small aperture and is detected by a photo-multiplier tube with a laser-line notch filter in front of it, the data

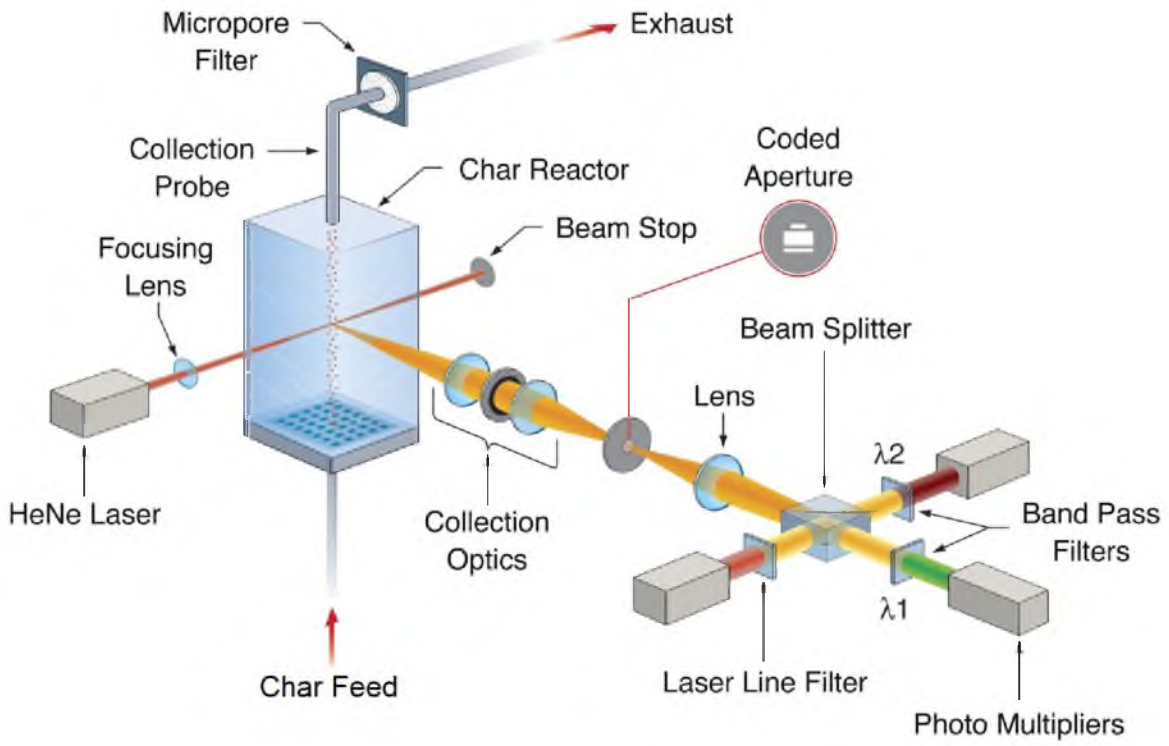


**Figure 5.1**. Optically accessible laminar entrained flow reactor. Particles are fed into the center of a flat-flame Hencken burner and react as they travel upwards in a quartz chimney. A laser scatters off individual particles when they are in the focus plane of the optics, triggering the data acquisition system, which measures the particle emission at two wavelengths as the image travels across a coded aperture.

collection system is triggered. The particle image travels across two more slits, of extended width, and the emissions from the particle at two wavelengths is measured. Light emissions from the particle as the image travels across the coded aperture are recorded at two different wavelengths. LabView is used to collect and analyze data from the photomultipliers. Signal processing removes any bad signals, such as when multiple particle images are traveling across the apertures at the same time, or if the signal is saturated, or below the noise level. From these signals, the particle size, velocity, and temperature are calculated. Typically, measurements are made on roughly 100 particles before changing the distance between the burner and where the measurement is made (changing the residence time in the reactor). The optics in this setup are fixed, and the burner is moved up and down to vary the residence time.

Also shown at the top of Fig. 5.1 is the collection probe. In separate experiments to the optical experiments, this water-cooled probe is used to collect char particles. A helium quench gas is injected radially at the tip of the probe, which is maintained at a low

temperature through water cooling. The cool gas is meant to quench the reactions of the particle at the tip of the probe, for which the residence time can be calculated. The probe is run isokinetically, where the particle velocities are the same as if the probe were not present, by varying the suction rate of the probe. Particles are collected on a filter. Particle feed rates during collection experiments are slightly higher than during optical experiments, to reduce collection time, which is typically on the order of 20 mins to collect about 10 mg of partially reacted char.

Collected samples are further analyzed off-line using a TGA. One measurement made on the collected samples is a burnout measurement, where the fixed carbon remaining in the samples are determined. By assuming that the ash in the chars does not gasify, the extent of reaction can be determined as a function of residence time, by comparing the percentage of fixed carbon in the chars. To measure the fixed carbon using the TGA, the ASTM standard for proximate analysis of coal is followed [83], neglecting the lid placement and removal and the minimum sample size. The procedure involves ramping the sample to 107 °C under a nitrogen atmosphere and soaking at that temperature to remove any moisture that might have accumulated during storage and collection of the sample. This is followed by a temperature ramp at 30 K/min and soak for 7 mins at 900 °C to remove any remaining volatiles. The temperature is then ramped down to 600 °C, the atmosphere is switched to air, and the temperature is ramped back to 750 °C at 3 K/min to react the remaining carbon in the sample. When the weight change is zero, the TGA is cooled back to room temperature. It is assumed that all of the fixed carbon is removed in the air environment portion of the TGA run, and that only ash remains at the end of this procedure.

The other procedure performed on the collected samples is an analysis for specific surface area. Brunauer, Emmett, and Teller [84] generalized Langmuir's adsorption theory to multimolecular adsorption by considering polarization theory. They arrived at the equation

$$v = \frac{v_m c x}{1-x}\left[\frac{1-(n+1)x^n+nx^{n+1}}{1+(c-1)x-cx^{n+1}}\right], \tag{5.1}$$

where $v_m$ is the volume of gas when the entire adsorbent surface is covered with a complete unimolecular layer, $x = p/p_s$, $p_s$ is the saturation pressure of the adsorbant, $c \approx e^{(E_1-E_L)/RT}$, where $E_1$ is the heat of adsorption of the first layer, and $E_L$ is the heat of liquefaction. Equation 5.1 is plotted in Fig. 5.2, for various numbers of adsorbed layers. For a low number of adsorbed layers, the isotherm is always concave down, and as the number of adsorbed layers becomes large, the isotherm achieves more of an S-shape. As summarized by Stoeckli and Houriet [85], Dubinin and Radushkevich describe the volume filling of micropores through the equation

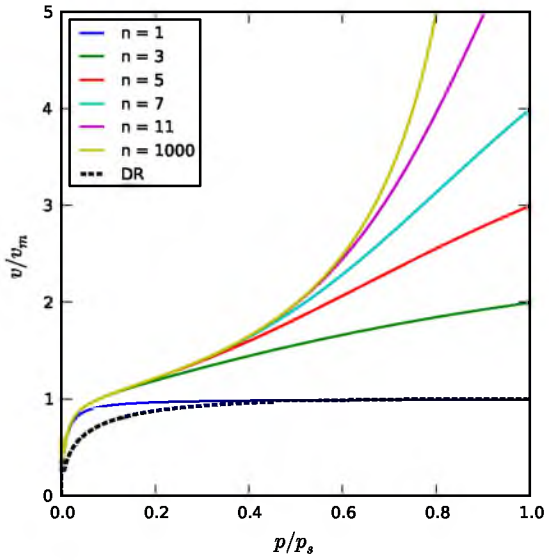


**Figure 5.2**. Brunauer-Emmett-Teller (BET) and Dubinin-Radushkevich (DR) isotherms. BET isotherms are labeled by the number of adsorbed layers.

$$v = v_m \exp\left[-\frac{B}{\beta^2}T^2 \log^2\left(\frac{1}{x}\right)\right], \tag{5.2}$$

where $B$ is a structural constant, and $\beta$ is an affinity coefficient. The isotherm for the Dubinin-Radushkevich (DR) theory is also shown in Fig. 5.2. The DR theory predicts a smaller adsorbed volume than the BET theory, for a given partial pressure of adsorbant.

For the collected coal chars, a typical adsorption experiment involved ramping and soaking the sample at 107 °C under a helium purge to remove any moisture that may have adsorbed during collection and storage. The samples were then ramped down to 30 °C, and the gas mixture was varied in several steps up to 100% $CO_2$ in helium. Helium is not expected to adsorb to the surface of the carbons, while $CO_2$ is, and the weight change as a function of partial pressure of $CO_2$ was used to find $v_m$, the volume of $CO_2$ adsorbed in a monolayer of the char surface area. By making an assumption on the packing density of $CO_2$, the surface area of the chars was determined. The packing density of $CO_2$ was evaluated by adsorption on the activated carbon, Carboxen. In this work, the Dubinin-Radushkevich relation was found to produce better results than the BET equation, and was used to analyze surface areas. The specific surface area for $CO_2$ was found to be 38 $Å^2$/molecule, which is significantly higher than the roughly 17 $Å^2$/molecule often quoted in the literature, but this could be due to the low packing densities at temperatures close to the critical temperature for $CO_2$, as noted by Marsh and Siemieniewska [86].

To summarize, coals were first devolatilized using a high temperature (1200 °C) drop-tube furnace with a $N_2$ diluent. These chars were sieved into narrow size ranges and fed into the laminar entrained flow reactor shown in Fig. 5.1. Measurements of temperature, velocity, and size were made on individual particles in various environments, for a range of residence times. Chars were also collected in some of the environments. Collected chars were further analyzed for burnout and micropore surface area using a TGA.

# CHAPTER 6

# EXPERIMENTAL MEASUREMENTS AND ANALYSIS OF COAL CHARS REACTING IN OXY-COMBUSTION ENVIRONMENTS

## 6.1 Introduction

Among the promising means of carbon capture and storage from coal-fired power plants is oxy-combustion. Oxy-combustion involves the separation of oxygen from air before introduction to the boiler, and then combustion of the solid fuel with pure oxygen diluted with recycled flue gas to control the temperature. Recycle could occur before or after moisture removal, but the recycle stream (which is primarily $CO_2$) is likely to contain some amounts of moisture [36]. After condensing out the moisture, the oxy-combustion effluent is highly-concentrated $CO_2$, which can be readily condensed, transported, and stored. At the University of Utah, a DQMOM/LES formulation for heterogeneous chemistries has been developed [87] for which validation and verification data are necessary for predictive modeling of the oxy-combustion of coal. A predictive model with quantified uncertainty will allow the rapid development of new build and retrofit oxy-combustion boilers.

For a retrofit application, recirculation of the flue gas could cause $CO_2$ levels in the furnace to approach 60-70 vol-%, and water vapor levels of up to 25-35 vol-% in postflame furnace gases. Both $CO_2$ and $H_2O$ have higher molar heat capacities than $N_2$, and are radiantly active gas species while $N_2$ is not. These gas properties will cause obvious heat transfer differences between air-fired and oxy-combustion environments. In addition, oxygen diffuses more rapidly through $N_2$ than $CO_2$, but more rapidly through $H_2O$ than either $N_2$ or $CO_2$, which will change the mass transfer characteristics during oxy-combustion. Previous research has shown that the substitution of $CO_2$ for $N_2$ delays coal ignition and reduces the

rate of coal volatile consumption, for a given furnace temperature and oxygen concentration [8, 20, 21]. A reduced burning rate in a oxy-combustion environment has been attributed to the reduced rate of oxygen diffusion in the boundary layer [18–20].

In addition to these known effects, with elevated levels of $CO_2$ and $H_2O$, gasification reactions, which are traditionally neglected for air-fired combustion, may begin to impact the char combustion rate and temperature. There has been some evidence that gasification reactions enhance the combustion rate under oxy-combustion conditions [14–16], but the high endothermicity of the gasification reactions lowers the combustion temperature, complicating the effects of these reactions. In some recent modeling efforts, we found that when a char particle is reacting at a temperature near the gas temperature (i.e. when there is a low $O_2$ concentration in the surrounding gas), the $CO_2$ gasification reaction increases the overall consumption of solid carbon, but only by a small amount. Alternatively, when the particle is reacting at a temperature considerably higher than the ambient gas temperature (i.e. in a high $O_2$ concentration environment), the $CO_2$ gasification reaction decreases the overall carbon removal rate, again by a small amount [17]. With a different treatment of the surface area, we found that although both the $CO_2$ and $H_2O$ gasification reactions reduced the combustion temperatures, the char carbon removal rate slightly increased in a wide range of environments [17].

Even for a single char particle reacting in a quiescent environment and considering only global reactions, there are many transport and kinetic phenomena involved. From the bulk gas, there is transport of reactants and inerts, which in the current study consists of $N_2$, $CO_2$, $H_2O$, and $O_2$. Heterogeneous reactions occur at the char particle surface, including oxidation ($\Delta h = -111\phi - 394$ kJ/mol):

$$C_s + (1 - \phi/2)O_2 \rightarrow \phi CO + (1 - \phi)CO_2, \tag{6.1}$$

$CO_2$ gasification ($\Delta h = 172$ kJ/mol):

$$C_s + CO_2 \rightarrow 2CO, \tag{6.2}$$

and $H_2O$ gasification ($\Delta h = 131$ kJ/mol):

$$C_s + H_2O \rightarrow H_2 + CO. \tag{6.3}$$

Gas diffuses into and out of the pores in the char particle where further reactions may take place, and products diffuse through the boundary layer back into the bulk gas. Gas

phase chemistry can occur in the boundary layer and in the pores of the particle as well, with reactions including CO oxidation ($\Delta h = -283$ kJ/mol):

$$CO + (1/2)O_2 \rightleftharpoons CO_2, \tag{6.4}$$

the water gas shift reaction ($\Delta h = -41$ kJ/mol):

$$CO + H_2O \rightleftharpoons CO_2 + H_2, \tag{6.5}$$

and $H_2$ oxidation ($\Delta h = -242$ kJ/mol):

$$H_2 + (1/2)O_2 \rightleftharpoons H_2O. \tag{6.6}$$

In this work, fundamental data of single coal char particle combustion in oxy-combustion environments are reported and analyzed. Combustion in a wide range of gaseous environments were studied to evaluate contributions to heterogeneous carbon consumption by oxygen, steam, and carbon dioxide. These data provide valuable insight into important reaction and transport phenomena for validation and verification of a model for the oxy-combustion of coal chars.

## 6.2 Methods

Three coals were chosen for this work: a representative high volatile bituminous coal from the Illinois #6 seam, a low-sulfur western bituminous coal from the Utah Skyline mine, and Black Thunder sub-bituminous coal from the Powder River Basin (PRB). A proximate and ultimate analysis of these coals is shown in Table 6.1. The PRB coal has the lowest fixed carbon, the highest moisture content, and the lowest heating value. These characteristics are expected since the PRB coal is sub-bituminous and of lower rank than other two bituminous coals. The two bituminous coals are similar in composition and heating value, although the Illinois #6 coal has a higher sulfur content.

As discussed in Chapter 5, these coals were first devolatilized using a drop tube furnace at the University of Utah. The furnace was operated at 1200 °C while flowing 15 SLPM nitrogen with approximately 1 vol-% oxygen to burn off any tars that might be generated during devolatilization. The furnace has an ID of 5 cm and a heated length (of temperatures between 1000 and 1200 °C) that is about 60 cm long. This led to a residence time of about 0.9 sec. Chars were collected and then sieved into 6 narrow size bins (53-63 $\mu$m, 63-75 $\mu$m, 75-90 $\mu$m, 90-106 $\mu$m, 106-125 $\mu$m, and 125-150 $\mu$m). Interestingly, the majority of PRB

**Table 6.1**. Proximate and Ultimate analyses for the three project coals

| Coal | Black Thunder | Utah Skyline | Illinois #6 | |
|---|---|---|---|---|
| Moisture | 23.69 | 3.18 | 9.64 | wt-%, as received |
| Ash | 4.94 | 8.83 | 7.99 | wt-%, as received |
| Volatile Matter | 33.36 | 38.6 | 36.78 | wt-%, as received |
| Fixed Carbon | 38.01 | 49.39 | 45.58 | wt-%, as received |
| C | 75.27 | 80.24 | 78.51 | wt-%, dry, ash free |
| H | 5.03 | 5.75 | 5.49 | wt-%, dry, ash free |
| N | 1.09 | 1.61 | 1.36 | wt-%, dry, ash free |
| S | 0.32 | 0.60 | 4.83 | wt-%, dry, ash free |
| O (by diff) | 18.29 | 11.80 | 9.81 | wt-%, dry, ash free |
| HHV | 12720 | 14327 | 14080 | BTU/lb., dry, ash free |

char was smaller than the parent coal (likely through fracturing and loss of volatiles), the Utah Skyline char was roughly the same size as the parent coal, while the Illinois #6 chars seemed to swell during devolatilization.

Chars in the narrowly sieved size bins were then fed into Sandia's optical entrained flow reactor that is also described in Chapter 5. A flat-flame Hencken burner is used to generate a high-temperature, well-characterized environment into which the char particles are fed. As the particles flow upwards in the reactor, optical diagnostics simultaneously measure size, velocity, and temperature of individual particles. Twelve different environments were used in this study: two at 24 vol-% $O_2$, with 14 vol-% $H_2O$, and a balance $N_2$ or $CO_2$; four at 36 vol-% $O_2$, with 10 and 14 vol-% $H_2O$, and a balance of $N_2$ or $CO_2$; and 6 at 60 vol-% $O_2$, with 10, 14, and 16 vol-% $H_2O$, and a balance $N_2$ or $CO_2$. Significantly oxygen-enriched conditions were chosen so that oxidation reactions would increase the combustion temperature, and thereby the rate of the gasification reactions to measurable levels. Intuition might suggest that at high temperatures, reactions would proceed very fast leading to diffusion limitations, but Murphy and Shaddix found that char particles react under increasing kinetic control at higher oxygen concentrations because of the higher oxygen flux available to the particle at these elevated oxygen concentrations[13]. When nitrogen was used as a diluent, the Hencken burner was operated at an adiabatic flame temperature of 1750 K, and with the $CO_2$ diluent, at 1850 K. A thermocouple was used to measure the reactor temperatures, and these conditions produced similar temperature profiles that all peaked around 1650 K. Temperature, velocity, and size measurements were made at 3-7 heights for around 100 particles in each of the size bins in all of the environments.

In addition to the optical measurements, under several conditions, chars were also

collected, and the burnout measurements described in Chapter 5 were made off-line in a TGA. Since there were three chars in six size bins that reacted in twelve different environments, it was not feasible to collect chars and make burnout measurements on all of the different variables explored. Therefore, for a given coal char, chars that experienced variations in oxygen concentration or steam concentration, or size were collected, or for a given environment and size, variations in coal chars were collected. For some of the collected coal chars, surface area measurements were also made, following the procedure described in Chapter 5.

Quantitative analysis of reaction kinetics is difficult, owing to particle-to-particle variability in reactivity, and the largely unknown kinetic mechanisms. In this work, the single-film model described in Chapter 4 was fit to the data. The four reaction steps shown by Rxns. 4.1–4.4 were considered, and the reaction orders were each first order with respect to the reactant ($O_2$, $CO_2$, and $H_2O$). Eq. 4.18 was used to determine the rate coefficients, and Eq. 4.21 shows the first order dependence on reactant concentration. Reaction 4.2 was set, based on the kinetic parameters in Rxn. 4.1 by the relationship given by Tognotti et al. [71]. Therefore, the pre-exponential factor for Rxn. 4.2 is 0.02 times the pre-exponential of Rxn. 4.1, and the activation energy is $3070R$ J/mol lower than the activation energy of Rxn. 4.1. With these constraints, the six parameters used to fit the data were the activation energies and pre-exponential factors for Rxns. 4.1, 4.3, and 4.4. The activation energies for these reactions were further constrained, based on the literature review described in Chapter 3. The activation energy for oxidation to CO (Rxn. 4.1) was constrained to lie between 150–190 kJ/mol, 230–270 J/mol for $CO_2$ gasification (Rxn. 4.3), and 190–270 for $H_2O$ gasification (Rxn. 4.4).

Fits were found to median optically measured particle temperatures for a size-binned char, in an environment, at a given residence time. With measurements at 3-7 heights in each environment, there were about 330 measurements for each char type. A 'particle' was created for each of these roughly 100 optical measurements, reacting at the median temperature at a given residence time. Due to significant uncertainties in the optically measured particle sizes, the diameter of each of these 'particles' was set to the mid-point of the fed size-bin (regardless of residence time or degree of burnout at which the temperatures were measured). Then, for a given set of kinetic parameters, the 'particle' temperature was set, and the species conservation equations (Eq. 4.8) were solved to determine the concentration of reactants at the particle surface, and the kinetic reaction rates. The error for the 'particle' was then calculated as the error in the thermal energy balance

equation (Eq. 4.10). The appropriate kinetic parameters were determined by minimizing the least-squared error for these 'particles' through MINPACK's lmdif and lmdir subroutines, as implemented in SciPy [78].

With kinetic fits, the burnout characteristics of the chars were calculated. A thermal inertia term was added to Eq. 4.10, so that it becomes

$$\dot{N}''_{\mathrm{C},p} h_{\mathrm{C},p} - \epsilon\sigma\left(T_p^4 - T_w^4\right) - \frac{\rho c_p r_p}{3}\frac{dT}{dt} = \sum_{i=1}^{n_{\mathrm{gas}}} \dot{N}''_i h_{i,p} + \frac{\bar{\lambda}}{r_p}\left[\frac{\kappa}{e^{\kappa}-1}\right](T_p - T_\infty), \tag{6.7}$$

where $c_p$ is the heat capacity of the char (assumed to be constant for all the chars at 2000 J/kg-K). The $dT/dt$ term was evaluated as $(T^n - T^{n-1})/\Delta t$, where superscript $n$ indicates the current time-step, at which all other temperatures and properties are evaluated. A pseudo-steady state was assumed, where the particle follows the single-film model at any point in time. Burnout progressed following the scheme proposed by Hurt et al. [10]. For a given time, the single-film model is solved (including the inertial term), calculating the particle temperature, mole fractions of reactants at the surface, and the molar burning rate, $\dot{N}_{\mathrm{C}}$. The molar burning rate given by Eq. 4.22 is converted to a mass rate ($dm/dt$) through the molecular weight of carbon, then the updated mass of the particle is given by

$$m = \frac{4}{3}\rho\pi r_p^3 + \frac{dm}{dt}dt. \tag{6.8}$$

Conversion is calculated as $X = 1 - m/m_0$ where $m_0$ is the initial mass of the particle. The mass fraction of carbon is related to the conversion through the relation $x_{\mathrm{C}} = (X - X_{\mathrm{C},0})/(1-X)$ where $X_{\mathrm{C},0}$ is the initial mass fraction of carbon (relative to carbon and ash) in the char particle. The mass of carbon is calculated by $m_{\mathrm{C}} = x_{\mathrm{C}} m$ (similarly, the initial mass of carbon can be calculated by using the initial mass fraction) and then the density of carbon is updated by

$$\rho_{\mathrm{C}} = \rho_{\mathrm{C},0}\left(\frac{m_{\mathrm{C}}}{m_{\mathrm{C},0}}\right)^{\alpha}. \tag{6.9}$$

In this equation, $\alpha$ is the mode of burning parameter, assumed to be the constant value of 0.25, as suggested by Mitchell et al. [88], that describes the fraction of carbon removed from the internal surfaces of the char to the fraction removed from the surface. For $\alpha = 1$, the density of the particle would continually decrease, but the diameter would remain fixed, and for $\alpha = 0$, the density would remain constant while the particle diameter would shrink as burnout progressed. After the density of carbon is calculated, the particle density is updated through the expression

$$\frac{1}{\rho} = \frac{x_{\mathrm{C}}}{\rho_{\mathrm{C}}} + \frac{1 - x_{\mathrm{C}}}{\rho_a}, \tag{6.10}$$

where $\rho_a$ is the density of the ash (assumed to be 2500 kg/m$^3$). In these simulations, the initial density of carbon is assumed to be 400 kg/m$^3$ for all three of the chars, and the initial particle density is calculated through Eq. 6.10, using the initial weight fraction of carbon in each char. Finally, with the updated density, the diameter of the particle is also updated through the relation

$$d_p = \left(\frac{6m}{\pi\rho}\right)^{1/3}. \tag{6.11}$$

Using these relationships, the particle solution is calculated from its initial injection into the EFR through heat-up, reaction, and burnout. It should be noted that many of the char structural parameters, such as the surface area, porosity, and tortousity, are assumed to remain fixed as burnout progresses in this model.

## 6.3 Results and Discussion

### 6.3.1 Experimentally Measured Temperatures

The gas temperatures were measured in each of the different environments using a 0.001" type R thermocouple. Because of the small diameter, radiation losses were minimized. Nonetheless, these losses are accounted for by an energy balance on the thermocouple wire. For a cylinder in cross-flow at low Reynolds number, the Nusselt number is found through the relation given by Hilpert [89], $\mathrm{Nu} = 0.989\mathrm{Re}^{0.33}\mathrm{Pr}^{1/3}$, where Re is the Reynolds number (based on the diameter of the thermocouple and the gas velocity) and Pr is the Prandtl number. Convection is balanced by radiation and the gas temperature will satisfy the equation

$$\sigma\epsilon(T_g^4 - T_w^4) = \frac{\mathrm{Nu}k}{d_{TC}}(T_g - T_{TC}), \tag{6.12}$$

where $\sigma$ is the Stefan-Boltzmann constant, $\epsilon$ is the emissivity of the thermocouple wire (assumed to be 0.2), $T_w$ is the wall temperature (assumed to be 500 K), $k$ is the thermal conductivity of the gas, $d_{TC}$ is the diameter of the thermocouple wire, $T_{TC}$ is the temperature measured by the thermocouple, and $T_g$ is the gas temperature.

Gas temperatures (corrected thermocouple measurements) are shown in Fig. 6.1. Differences between the gas and thermocouple temperatures are around 20 K. There is a heat up of the inert gas that feeds the particles in the first two inches of the furnace. This is followed by a peak temperature of around 1700 K in all but a few of the environments, and then a nearly linear drop-off of around 400 K over the length of the furnace. Environments that show the largest deviation from the mean temperature profile have 60 vol-% $O_2$ in the bulk gas. Some

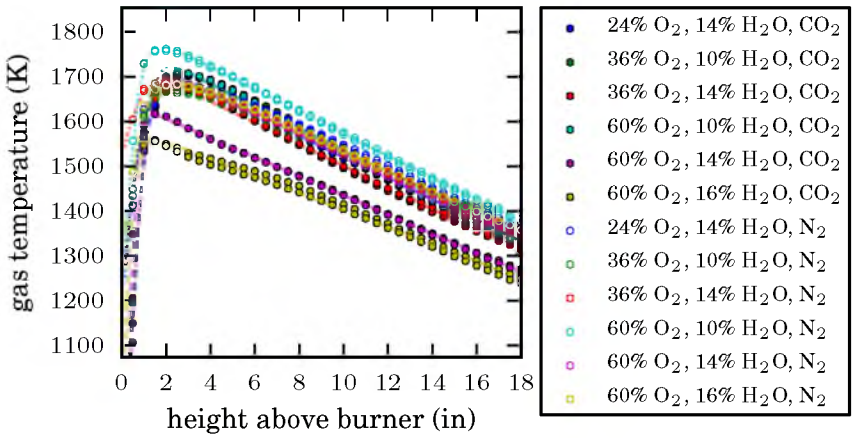


**Figure 6.1**. Gas temperature measurements in the different environments. There is hysteresis in some of the data as the thermocouple approached the burner and then moved away.

of the hypodermic burner fuel tubes would clog with oxidized metal under this condition, and maintaining a flat flame profile was difficult. This likely led to deviations from the ideal temperature profile (which was the same, based on the adiabatic flame temperatures, for all of the conditions).

A simulation was run using COMSOL Multiphysics® to determine the developing velocity profile in the Sandia reactor at 300 K. The calculated velocity profile at the reactor centerline was corrected by the mean gas temperature at the gas centerline, and the resulting velocity profle was compared to the mean optically measured particle velocities. Velocities predicted by the corrected developing flow profile, when scaled up by 7%, agree well with the optically measured particle velocities. The scaled, temperature corrected, developing flow profile is taken to be the particle velocities (it is the same for all particles), and the residence time in the reactor is calculated by integrating the height/velocity ratio. The overall residence time in the 18 inch reactor is calculated to be 171 ms.

A commercial digital camera was used to take photographs of the reacting char particles. The aperture and exposure time were set manually in an attempt to gather consistent photos, but the char feed rate varied, causing inconsistent particle loading during any given photo. Photographs of the reacting 90-106 $\mu$m Utah Skyline particles can be seen in Fig. 6.2 as a typical series. Trends in this figure are also evident in the other size bin photos, and for the different chars, although there is scatter due to the inconsistent feed rate. While these photos do not contain any quantitative information, qualitative information about burnout can be deduced from the length of the visible emissions, and the pixel brightness is

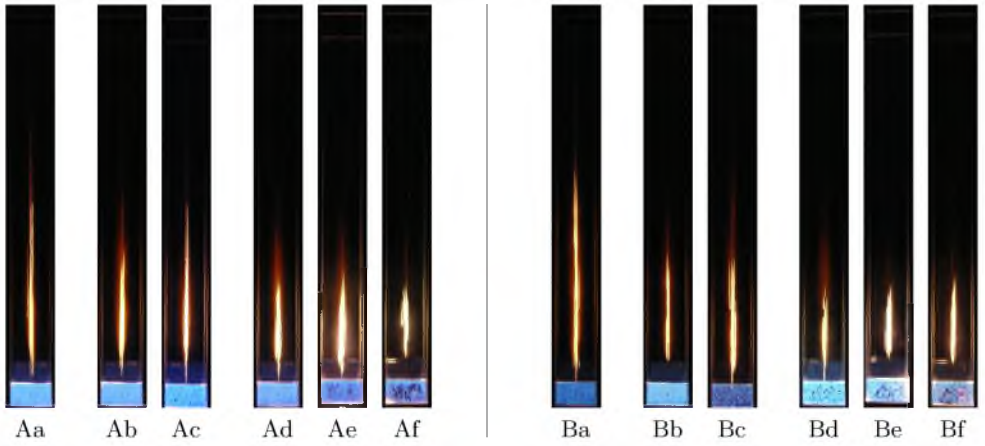


**Figure 6.2**. Digital photos of 90-106 $\mu$m Utah Skyline char combustion in different environments. Capital letter A denotes a diluent (balance) gas of $CO_2$ and capital B denotes a $N_2$ diluent. Lowercase letters denote: a) 24% $O_2$, 14% $H_2O$ b) 36% $O_2$, 10% $H_2O$ c) 36% $O_2$, 14% $H_2O$, d) 60% $O_2$, 10% $H_2O$, e) 60% $O_2$, 14% $H_2O$, f) b) 60% $O_2$, 16% $H_2O$. The bright blue at the bottom of the picture is the Hencken burner and the particles are flowing and reacting upwards in the pictures. The top of the picture is about 18 in above the burner, and the limit of the quartz chimney.

related to temperature. The poor Hencken burner flames can be seen as a lack of uniform blue at the bottom of the photos under high oxygen concentration conditions, as discussed with regards to the spread in the flame temperature measurements in Fig. 6.1.

As one might expect, as the oxygen concentration increases, the lengths of the visible emission traces in Fig. 6.2 decrease, and the emission brightnesses increase. With a higher oxygen concentration in the bulk gas, greater diffusion of oxygen through the boundary layer allows the exothermic oxidation reaction to proceed at a higher rate. This lowers the time required for burnout (shorter visible emission) and increases the temperature at which the particles are burning (brighter emission). The visible traces are also noticeably shorter with the $N_2$ diluent compared to the $CO_2$ diluent, at a given steam and oxygen concentration. This can be attributed to the greater diffusivity of oxygen through $N_2$ than $CO_2$ [18–20]. Although the trend is not completely evident in this series of photographs, in the complete set of photos, there appears to be a slight trend of faster burnout as the steam concentration increases. This effect is not as pronounced as the variation due to oxygen concentration differences, but the variation in steam concentration (10-16 vol-%) is also much less than the variation in oxygen concentration (24-60 vol-%). This could be due to either (or a combination of) steam gasification reactions consuming the char at a greater rate, or the higher diffusivity of oxygen through steam than either $CO_2$ or $N_2$. At 2000 K and 1 atm, the binary diffusion rate of oxygen through nitrogen is $5.2 \times 10^{-3}$, through $CO_2$

is $4.1 \times 10^{-3}$, and through $H_2O$ is $6.9 \times 10^{-3}$ $m^2/s$ (the relative diffusivities are shown in Fig. 1.2).

There is also evidence of more radial spreading of the chars as they react in higher oxygen concentration environments in Fig 6.2. The complete set of photographs shows that the PRB and Illinois #6 chars stray from the centerline more than the Utah Skyline char. This lateral movement of the chars as they react is probably due to remaining volatile matter in the char jetting from the pores and propelling the particles away from the centerline. At higher reaction temperatures (in the higher oxygen concentration environments), the rapid release of volatiles is more likely. This spread could also partially be attributed to a poor flame shape, and poorly developed velocity profile as the fuel tubes clogged under the 60% $O_2$ conditions.

As particles were reacting, temperature measurements were made at 3-7 heights of roughly 100 char particles. As shown in Fig. 6.3, there can be significant spread in the particle temperatures, caused partially by measurement error (estimated at ±20 K), but mostly by different reactivities, and variations in size of individual char particles. Because of this spread, the mean and median values measured for temperature are not always equivalent, with the median value generally being higher than the mean temperature. As the residence time in the reactor increases, there is a heat up of the particles, and then they tend to react at a fairly steady temperature, if not decreasing slightly as the residence time gets longer. To compare all of the chars reacting in all of the environments, the maximum median temperatures (regardless of the residence times) are plotted in Fig. 6.4. These temperatures are not a direct measurement of reactivity, but in general, higher temperatures for a given particle size correlate with higher combustion reactivity.

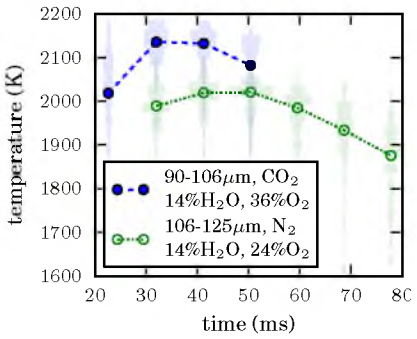


**Figure 6.3**. Utah Skyline char temperatures. Legend describes fed particle size, diluent gas (balance other than $O_2$ and $H_2O$), and $O_2$ and $H_2O$ vol-%. Circles are mean temperatures, and shaded region in the background are the normalized number density of particles within 20 K bins, showing the spread of the data.

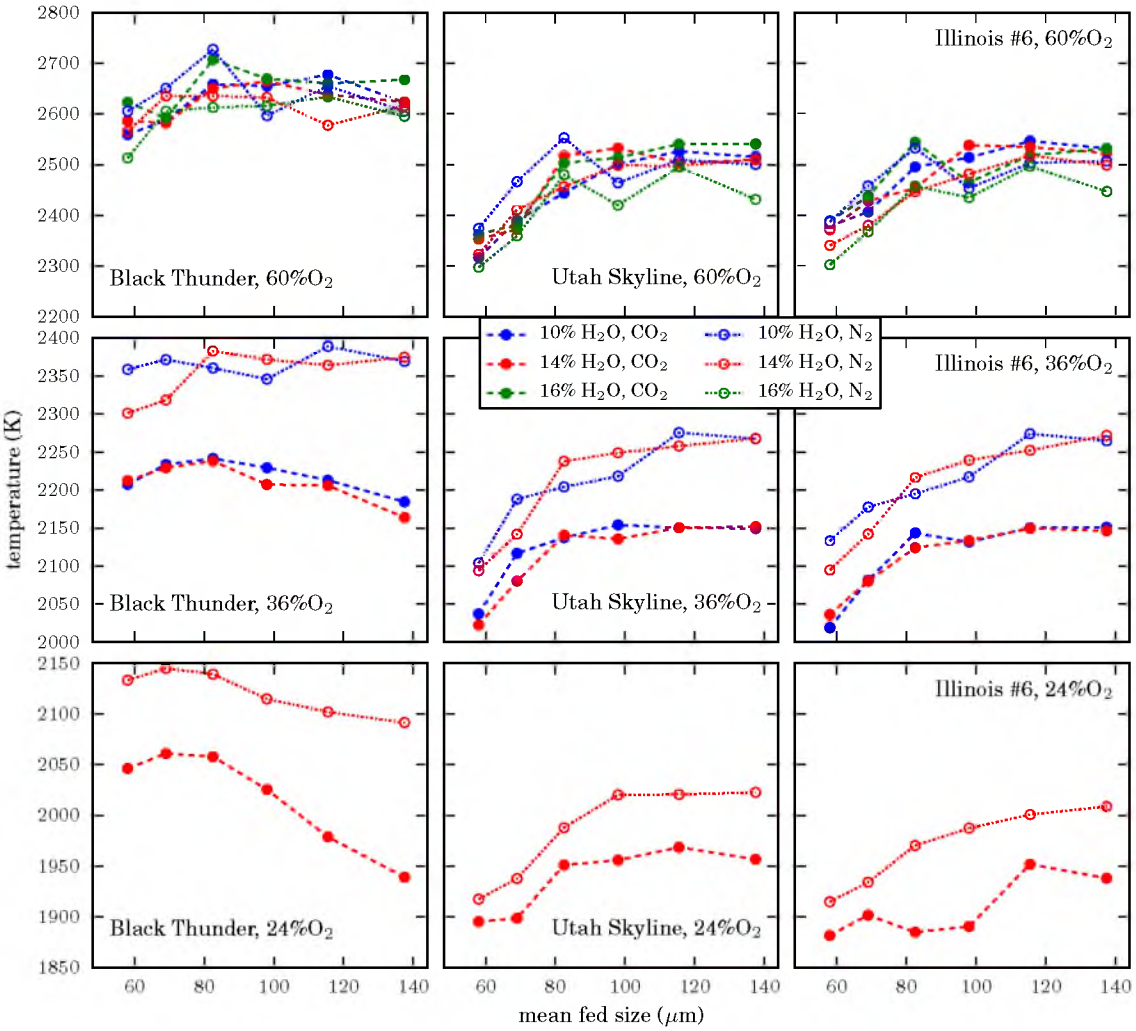


**Figure 6.4**. Char temperatures as a function of fed char diameter. Closed circles with long dashes have $CO_2$ as a diluent while open circles and short dashes have $N_2$ as a diluent. Colors are different steam concentrations, and the oxygen concentration varies with the vertical frames, as shown on the graph.

The more reactive sub-bituminous PRB char burns at a higher temperature than either of the two bituminous chars, which burn at about the same temperatures in all of the different environments. There is some dependence of temperature on particle size. For the Black Thunder char, the temperature seems to peak around 80 $\mu$m, while the Utah Skyline and Illinois #6 char temperatures increase (although they appear to level off) up to the largest particle size. A trade off exists between heat losses and available reactive surface area, leading to the dependency of temperature on particle size.

At both 24 and 36% $O_2$, there is an obvious influence of diluent on particle temperature.

Particles combust about 100 K hotter with the $N_2$ diluent than with the $CO_2$ diluent. This is consistent with the photographic evidence in Fig. 6.2, and other experimental observations [18, 20]. However, at 60% O2, all of the curves seem to collapse, and there are no obvious trends in temperature either due to diluent or steam concentration. As discussed earlier, the hypodermic fuel tubes of the Hencken burner had a tendency to clog at 60% $O_2$ (as can be seen by variations in flat-flame brightness in Fig. 6.2), leading to a more scatter in the data, making it more difficult to observe trends. The amount of diluent is significantly less with 60% $O_2$, with only 24-30% of the gas as a diluent, while there is 58-64% diluent in the 36% $O_2$ environment. Since the temperature difference between $N_2$ and $CO_2$ atmospheres is attributed to diffusion differences through the diluent, it is not too surprising that the difference decreases when there is very little diluent and a greater oxygen concentration. Independence of temperature from diluent may also be evidence of improved kinetic control in highly oxygen-enriched environments, as Murphy and Shaddix observed [13].

In the environments where the steam concentration was varied, there is no obvious trend of combustion temperature with steam concentration. However, as previously mentioned, the trace length in Fig. 6.2 decreased slightly as the steam concentration increased, suggesting faster burnout. An increase in the diffusivity of oxygen through steam would cause the exothermic oxidation reaction to proceed at a higher rate, and an increased concentration of $H_2O$ would cause the endothermic steam gasification reaction to proceed at a higher rate. These two effects are in competition to limit the temperature change in these environments, but lead to a greater consumption rate of carbon because of the higher concentrations of reactants at the particle surface. As described in Chapter 3, little temperature change, but an increase in carbon consumption as the steam concentration increases is predicted when the gasification reactions are considered [17].

### 6.3.2 Experimentally Measured Surface Area and Burnout

The collected chars were subsequently analyzed for burnout characteristics and the results are shown in Fig. 6.5. This busy figure includes all of the burnout data taken over the course of the experiments and is included to give the reader a place to make gross comparisons of all of the data. Many of the burnout trends are discussed in more depth and the data is included in later figures when model comparisons are made. There

**Figure 6.5**. Complete set of burnout data as a function of residence time in the reactor. Faint dashed lines in the background are the gas temperatures for the different environments. Symbol types and sizes are related to fed char size, and colors are related to steam concentration. $N_2$ diluent has open symbols, and $CO_2$ are filled, as detailed in the legend. Error bars are the standard deviation, and are only shown on data where experiments were repeated.

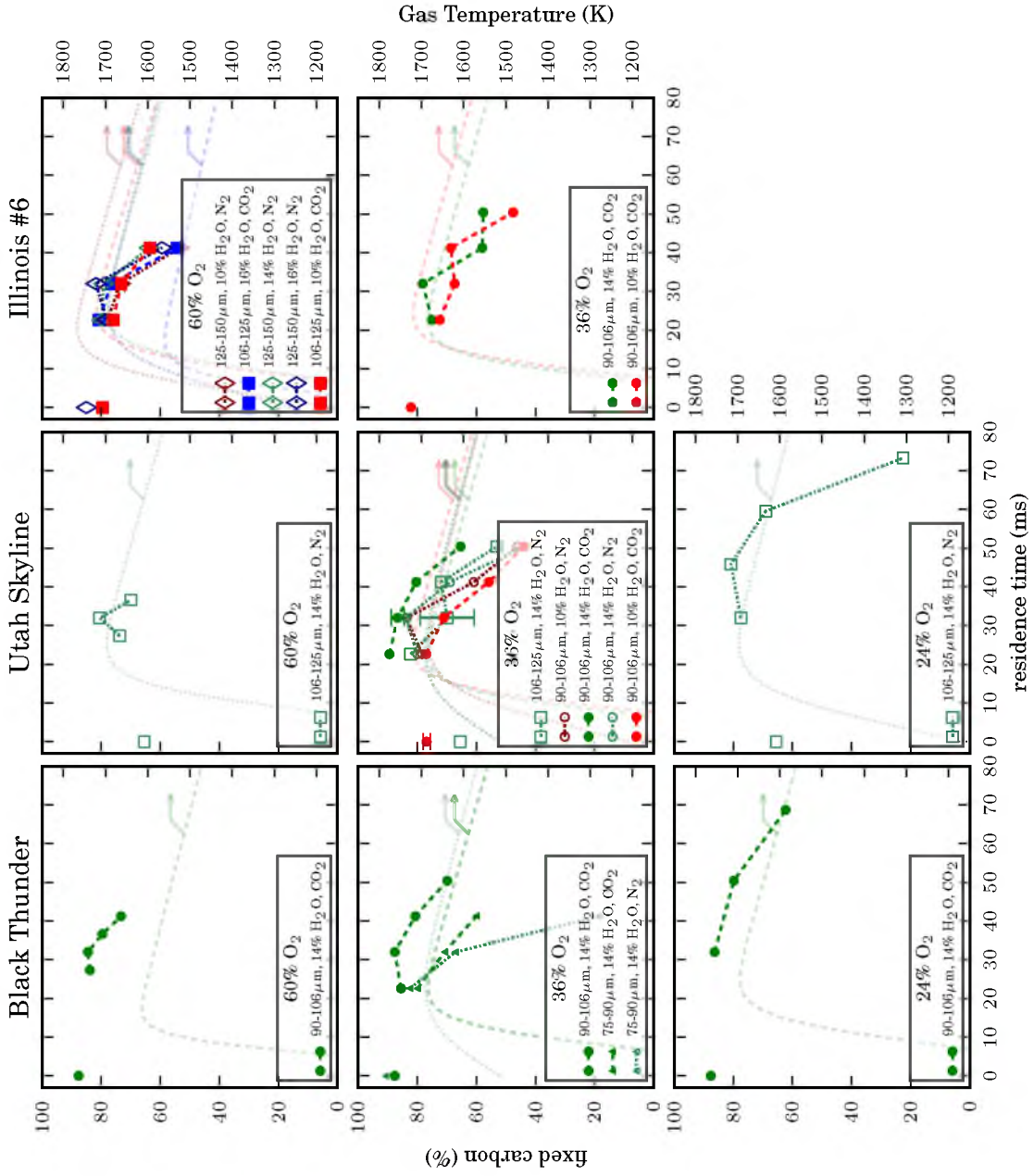
Black Thunder
Utah Skyline
Illinois #6
Gas Temperature (K)
fixed carbon (%)
residence time (ms)
60% O2
90-106μm, 14% H2O, CO2
36% O2
90-106μm, 14% H2O, CO2
75-90μm, 14% H2O, CO2
75-90μm, 14% H2O, N2
24% O2
90-106μm, 14% H2O, CO2
60% O2
106-125μm, 14% H2O, N2
36% O2
106-125μm, 14% H2O, N2
90-106μm, 10% H2O, N2
90-106μm, 14% H2O, CO2
90-106μm, 14% H2O, N2
90-106μm, 10% H2O, CO2
24% O2
106-125μm, 14% H2O, N2
60% O2
125-150μm, 10% H2O, N2
106-125μm, 10% H2O, CO2
125-150μm, 14% H2O, N2
125-150μm, 16% H2O, N2
106-125μm, 10% H2O, CO2
36% O2
90-106μm, 14% H2O, CO2
90-106μm, 10% H2O, CO2

is a lot of scatter in the burnout data, as confirmed by the large error bars on the data when experiments were repeated. There are many sources of error in these experiments. As the chars were being reacted in the EFR, especially in the 60% $O_2$ environment, the hypodermic fuel tubes were oxidizing and clogging, causing changes in the gas temperatures and velocity profiles seen by the particles. The potential for particle-particle interactions (such as radiative heat transfer, disrupted boundary layer, etc.) in the EFR is also increased during collection, since the feed rate is increased during the collection experiments. During collection, variations in suction could cause non-iso-kinetic measurements to be made, effectively changing the residence time of the collected particles. The TGA measurements require the operator to tare the crucible, remove it from the balance, fill it with sample, and replace it on the balance. As the balance is a lever-arm, any slight discrepancies in crucible placement can cause significant errors in mass measurements. Finally, the collected samples may not be homogeneous, and the selected sample for burnout measurement on the TGA may not be representative of the collected sample.

Nonetheless, there are several noteworthy points shown in Fig. 6.5. First, the particles do not seem to lose mass until at least 20 ms have elapsed. As shown by the gas temperatures, the initial time is required to heat the char particles to a high enough temperature that the reactions begin to proceed at a relevant rate. The particle temperatures will lag the gas temperatures, due to thermal inertia, but eventually, the exothermic oxidation reaction will add energy to the thermal energy balance, and the char burning will be sustained. Secondly, the slopes of the remaining fixed carbon, after the particles begin to lose mass, is steepest in 60% $O_2$, followed by the 36 and then the 24% $O_2$ in the bulk gas. The particle temperatures in Fig. 6.4, images in Fig. 6.2, and slopes of this burnout data all confirm that the burning rate of carbon is fastest in the highest oxygen concentration environments. Finally, we again note that variations in steam concentration have very little effect on the burning rate of the chars. The slopes of the fixed carbon fractions are roughly equal, regardless of the steam concentration.

Measurements of surface areas, corresponding particle temperatures, and fixed carbon are shown in Fig. 6.6. Attempted measurements on the initial chars resulted in negligible values of surface area. As the char heats up, significant surface area is developed, and that surface area rapidly decreases as burnout progresses. The sub-bituminous Black Thunder PRB char has the maximum measured surface area, at 500 $m^2/g$, which is significantly higher than the 10 $m^2/g$ surface area assumed in modeling performed in Chapters 3 and 4, but still a reasonable value. The $CO_2$ adsorption measurements give values of micropore

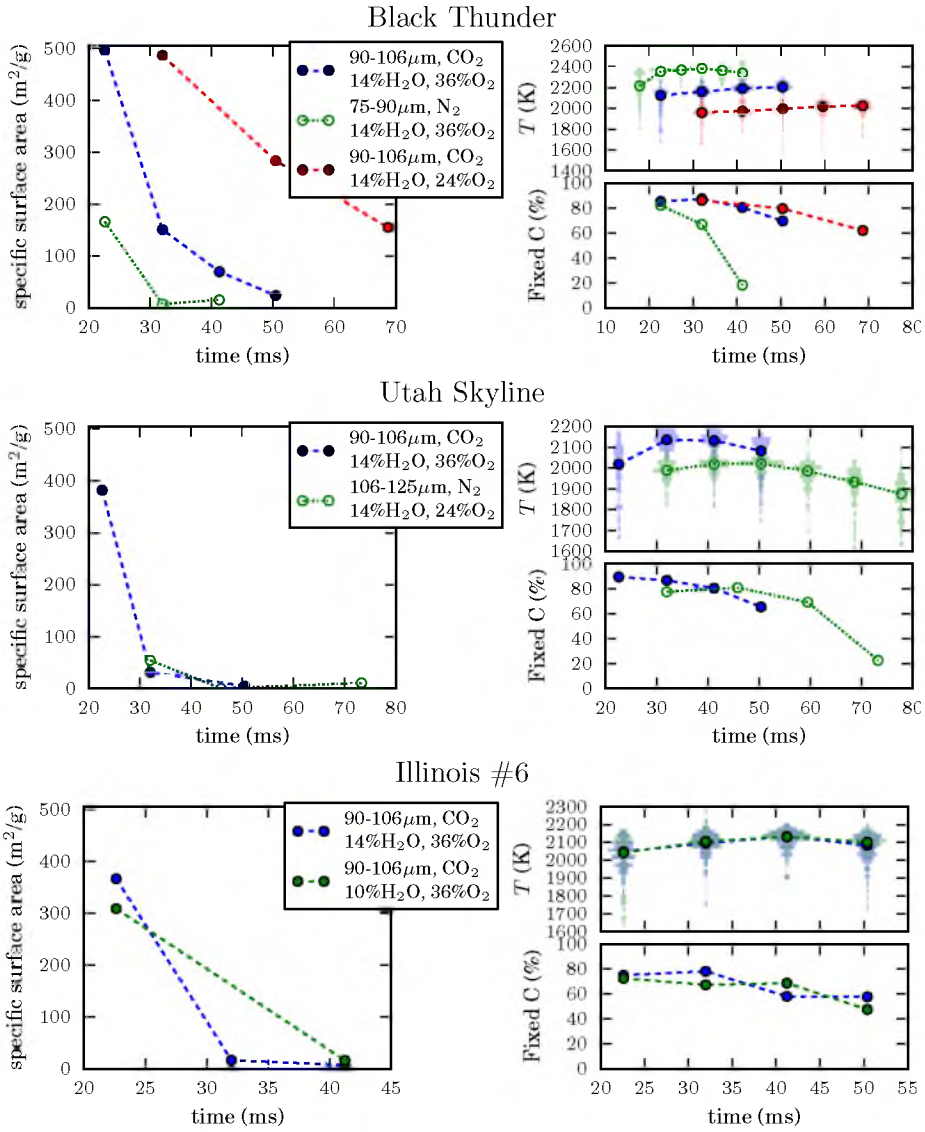


**Figure 6.6**. Measured surface areas as a function of residence time in the reactor (left), and corresponding fixed carbon and measured particle temperatures (right), with mean temperatures shown by the symbols, and histograms of the measured particles in 20 K increments shown by the light shading in the background.

surface area, while the modeling requires surface are that is accessible to the gases, which is likely the macropore surface area, with a characteristic dimension greater than 50 nm. The two bituminous chars show very similar initial surface areas and surface area decreases as burnout progresses. As with the burnout measurements, there are large errors associated with the surface area measurements. These measurements once again rely on the taring procedure of the TGA, and need to be even more sensitive to mass loss than the burnout measurements, as only a few percent of the initial weight is changing as the $CO_2$ is adsorbed

onto the surface of the chars.

Scanning electron microscope (SEM) images were also taken on several of the chars to see if the porosity was visible. Shown in Fig. 6.7 are both the starting chars, and the partially reacted chars. The chars fed into the EFR show very little porosity. It appears that after devolatilization, the chars plasticized (at least externally), sealing off the pores from gas penetration [90]. The partially reacted chars do show significant porosity, as the external layer, and interior of the char, were consumed during reactions. In 36%$O_2$, the particles collected at 32 ms appear intact, but with significant porosity, and gas penetration. The Illiniois #6 char, however, that was reacting in 60% $O_2$ for the same amount of time appears to be mostly fragments. This is likely not due to breakup in the EFR, but rather from the subsequent collection and sample transfer process. There is probably not enough structural carbon in these samples to keep them intact during these mechanical actions, while the less burned out Black Thunder and Utah Skyline chars are more structurally sound. The pores in the bituminous chars also appear fairly round, while the pores in the sub-bituminous Black Thunder char have a much larger aspect ratio and appear to be grouped in layers.

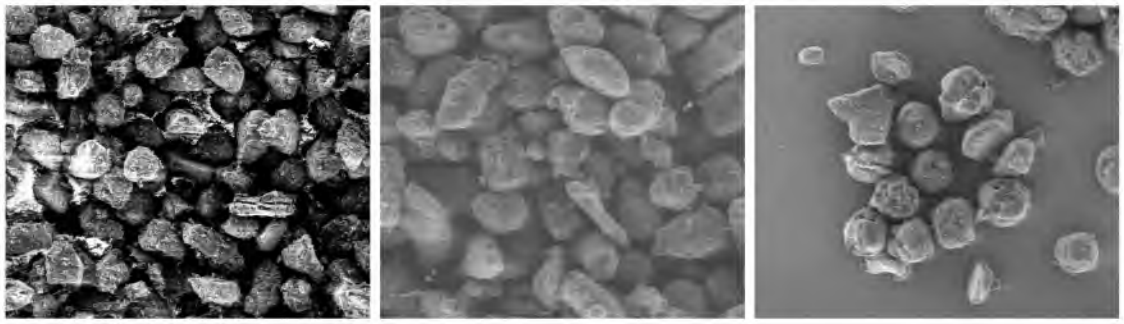

(a) Black Thunder char, 75-90 $\mu$m (b) Utah Skyline char, 90-106 $\mu$m (c) Illinois #6, 90-106 $\mu$m

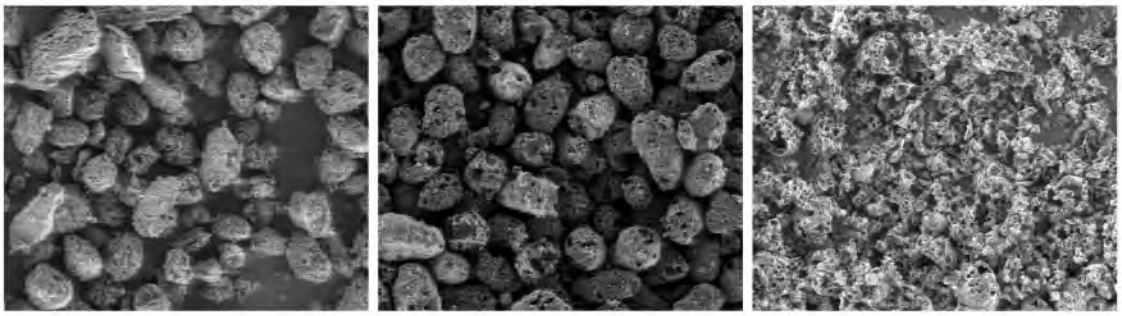

(d) Black Thunder char, 90-106 $\mu$m, 32ms in 36% $O_2$, 14% $H_2O$, $CO_2$ diluent (e) Utah Skyline char, 90-106 $\mu$m, 32ms in 36% $O_2$, 14% $H_2O$, $CO_2$ diluent (f) Illinois #6 char, 106-125 $\mu$m, 32ms in 60%$O_2$, 10%$H_2O$, $CO_2$ diluent

**Figure 6.7**. SEM images of the starting chars (top) and partially reacted chars (bottom).

### 6.3.3 Kinetic Fits

Optically measured temperatures were used to find kinetic fits for each of the chars, as described in Section 6.2. The slope of the error field is not very steep, and the solutions found are sensitive to the initial guess. For this reason, the solutions were found starting from the 'best-guess' parameters determined in Chapters 3 and 4. After convergence, the optimization routine was restarted from the last solution, until a stable set of kinetic parameters was found. Optimized parameters are shown in Table 6.2. For the oxidation reactions, the activation energy found for the two bituminous chars is near the lower bound of 150 kJ/mol for oxidation to CO and significantly lower than the activation energy found for the sub-bituminous char. The lower activation energy is a lower barrier for a reaction to occur, 'turning on' the reaction at a lower temperature. However, pre-exponential factors for the oxidation reaction of the bituminous chars are also an order of magnitude lower than the pre-exponential factors for the sub-bituminous char, meaning the reaction proceeds at a lower rate at higher temperatures.

To visualize the rate coefficients, they are plotted as a function of temperature in Fig. 6.8. At low temperatures (below 1000 K), the oxidation rate coefficients (Rxns. 4.1 and 4.2) are slightly higher for the bituminous chars than the sub-bituminous chars. At more relevant combustion temperatures, however, the sub-bituminous char has a rate coefficient that is nearly an order of magnitude higher than the bituminous char rate coefficients. The $CO_2$ gasification rate coefficient (Rxn. 4.3) is highest for the sub-bituminous char at all temperatures, but this rate coefficient is also more than an order of magnitude lower than the rate coefficient for oxidation to CO (Rxn. 4.1) for each of the chars. The steam gasification reaction rate coefficient (Rxn. 4.4) is fairly similar for the three chars at relevant combustion temperatures and is higher than the $CO_2$ gasification rate coefficient for all of the chars. For the two bituminous chars, the steam gasification rate coefficient is at least two orders

**Table 6.2**. Best fit kinetic parameters for the three project chars. Units of $A$ are m/s, and units of $E$ are kJ/mol.

| | Black Thunder sub-bituminous: | | Utah Skyline bituminous: | | Illinois # 6 bituminous: | |
|---|---|---|---|---|---|---|
| Reaction | A | E | A | E | A | E |
| $2C + O_2 \rightarrow 2CO$ | $2.22 \times 10^4$ | 169 | $1.92 \times 10^3$ | 152 | $1.46 \times 10^3$ | 150 |
| $C + O_2 \rightarrow CO_2$ | $4.44 \times 10^2$ | 144 | $3.84 \times 10^1$ | 126 | $2.93 \times 10^1$ | 124 |
| $C + CO_2 \rightarrow 2CO$ | $2.58 \times 10^4$ | 251 | $5.81 \times 10^2$ | 255 | $1.12 \times 10^2$ | 268 |
| $C + H_2O \rightarrow CO + H_2$ | $2.39 \times 10^4$ | 217 | $4.83 \times 10^3$ | 192 | $4.83 \times 10^4$ | 238 |

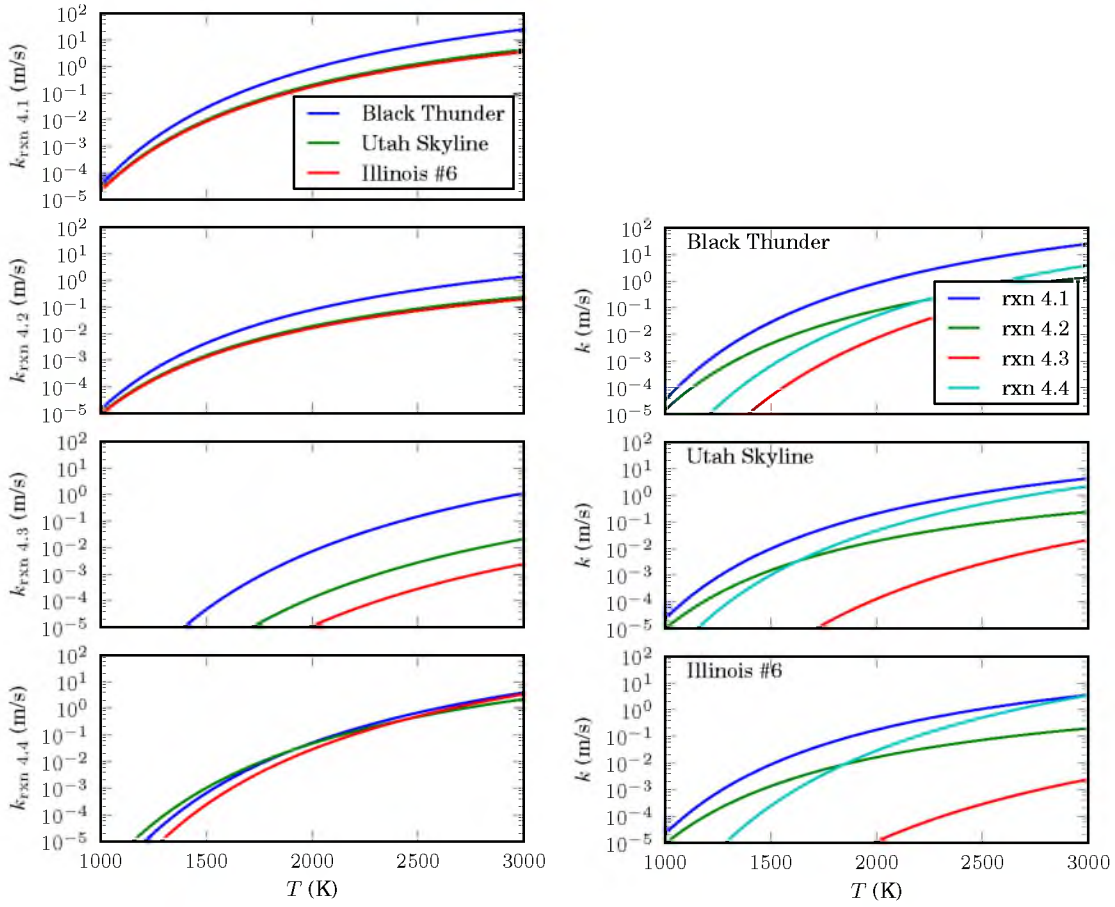


**Figure 6.8**. Reaction rate coefficients using the fit kinetic parameters shown in Table 6.2. The left-hand frames show the rate coefficients grouped by reaction, and the right-hand frames displays the rate coefficients grouped by char.

of magnitude higher than the $CO_2$ gasification rate coefficient at all of the temperatures shown.

For the Black Thunder char at 800 °C, the relative rate coefficient for gasification by $CO_2$ is $9 \times 10^{-5}$ times the rate coefficient for oxidation, and the rate coefficient for $H_2O$ is $3 \times 10^{-2}$ times the rate coefficient for $O_2$. The Utah Skyline char has rate coefficients that are $2 \times 10^{-6}$ and $2 \times 10^{-2}$, for $CO_2$ and steam gasification, respectively, times the rate coefficient for oxidation. The Illinois # 6 char has rate coefficients that are $1 \times 10^{-7}$ and $1 \times 10^{-2}$, for $CO_2$ and steam gasification, respectively, times the rate coefficient for oxidation. For $CO_2$ gasification reactions, the relative rates are near the expected value determined in Chapter 3 of $6.2 \times 10^{-5}$, although the relative rates for the bituminous chars are a little low. However, the relative steam gasification reaction rate coefficients are about two orders of magnitude above the best guess value of $2.0 \times 10^{-4}$, and at least an order

of magnitude higher than the maximum relative rate coefficient found in the literature of $1.0 \times 10^{-3}$.

The value in these kinetic parameters is to see if the experimental data can be recreated. Using the parameters in Table 6.2, the burnout model described in Section 6.2 was run for each of the chars. Like Fig. 6.4, the maximum simulated temperatures at any residence time as a function of fed particle diameter is plotted in Fig. 6.9. The simulated temperatures are much lower than the experimentally measured temperatures for the bituminous chars in 24 and 36% $O_2$, and for the Black Thunder char in 24% $O_2$. In the 60% $O_2$ environments, the

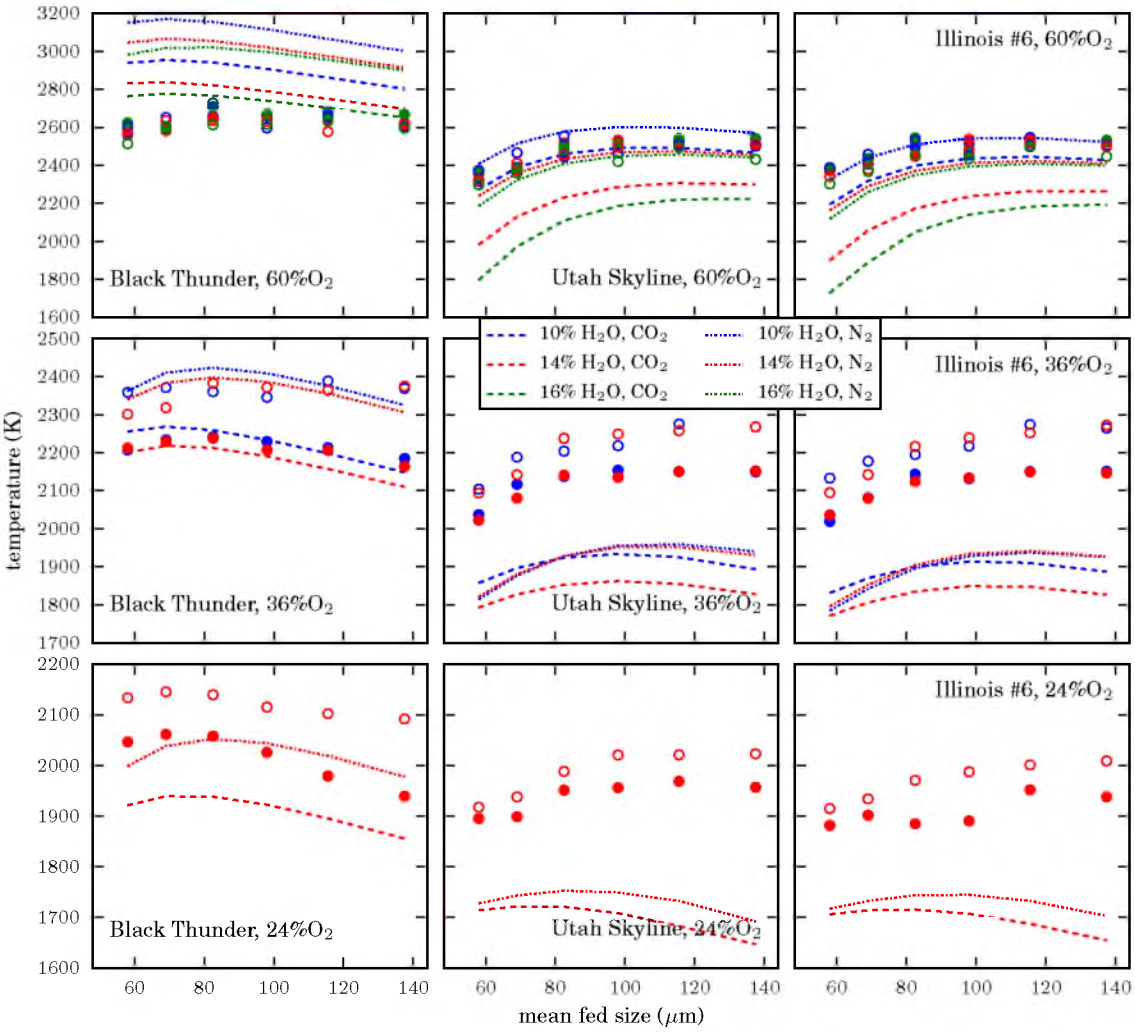


**Figure 6.9**. Simulated and experimentally measured char temperatures as a function of fed char diameter. Simulations using the kinetics given in Table 6.2 are shown by the lines, while the data of Fig. 6.4 are plotted as the symbols for comparison. Symbol styles and colors are the same as Fig. 6.4.

bituminous chars both agree fairly well with the experimentally measured temperatures, while the Black Thunder char temperatures are lower than the simulated values.

Many of the experimentally observed trends in temperature also occur during the simulations, although the magnitudes of the temperatures do not agree. All of the char particles react at higher temperatures when $N_2$ is the diluent as compared to $CO_2$, and the differences in temperatures between the two diluents are similar, perhaps with the exception of the reactions in 60% $O_2$. Secondly, the maximum measured temperatures peak at a similar size in the simulations and the measured data. Finally, the predicted temperatures for the sub-bituminous char are much higher than the predicted temperatures of the bituminous chars, and the bituminous char temperatures are predicted to be very similar in magnitude.

However, while the temperature predictions for the Black Thunder char are reasonable, albeit a somewhat low under in 24% $O_2$ and slightly high for 60% $O_2$, the bituminous char temperature predictions are significantly lower than the measured values, especially in the 24 and 36% $O_2$ conditions. As mentioned, the optimization was not very robust, and the solution for the kinetic parameters was likely a local minimum rather than the global minimum. Since the two bituminous chars react at similar temperatures, the best-fit activation energies for the Utah Skyline char were set, and the pre-exponential factors were manually adjusted to achieve better temperature predictions. Reasonable agreement was found using the kinetic parameters shown in Table 6.3. Reaction rate coefficients for the Black Thunder and bituminous chars are plotted as a function of temperature in Fig. 6.10. The oxidation kinetics now have less than an order of magnitude difference, even at 3000 K, and are the same value around 1200 K. The bituminous chars have an order of magnitude lower $CO_2$ gasification rate coefficient than the sub-bituminous char, and very similar $H_2O$ gasification rate coefficients. Although the rates appear similar in Fig. 6.10 (other than the $CO_2$ gasification rate), the temperature predictions are different.

Maximum combustion temperatures using the manual fit for the bituminous chars are shown in Fig. 6.11. The agreement for the bituminous chars is much better than the

**Table 6.3**. Manually adjusted kinetic parameters for the bituminous chars. Units of $A$ are m/s, and units of $E$ are kJ/mol.

| Reaction | A | E |
|---|---|---|
| $2C + O_2 \rightarrow 2CO$ | 5000 | 152 |
| $C + O_2 \rightarrow CO_2$ | 100 | 126 |
| $C + CO_2 \rightarrow 2CO$ | 1000 | 255 |
| $C + H_2O \rightarrow CO + H_2$ | 5000 | 192 |

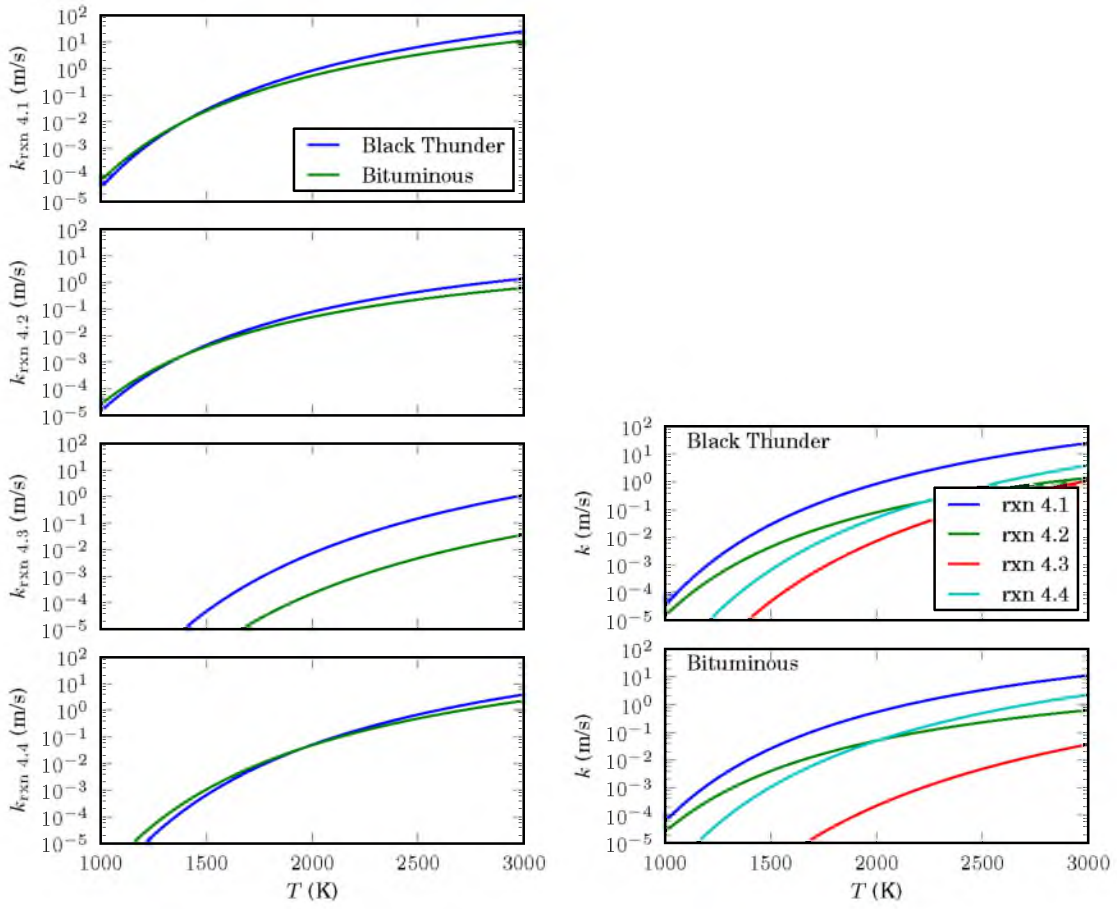


**Figure 6.10**. Reaction rate coefficients using the computer optimized kinetic parameters shown in Table 6.2 for the Black Thunder char, and the manually adjusted rate parameters shown in Table 6.3 for the bituminous chars.

agreement in Fig. 6.9. Predictions for temperatures in 60% $O_2$ are high, and for 24% $O_2$ are low, but overall, these kinetics capture the experimentally observed trends. Further manual adjustment of the kinetic fits could be made, but manual trial and error is a tedious process. The original least-squared optimization procedure was comparing steady-state temperatures to the experimentally measured median temperatures as a function of time. A more appropriate data set for optimization may have been the maximum median temperatures as a function of fed particle size. Rather than the steady-state model, the transient model may also be more appropriate for making data comparisons. However, running on a PC, the iteration time of the transient model for each particle is around 3-5 minutes, and an optimization procedure requiring transient model results as a function of kinetic parameters would take an unreasonable amount of time.

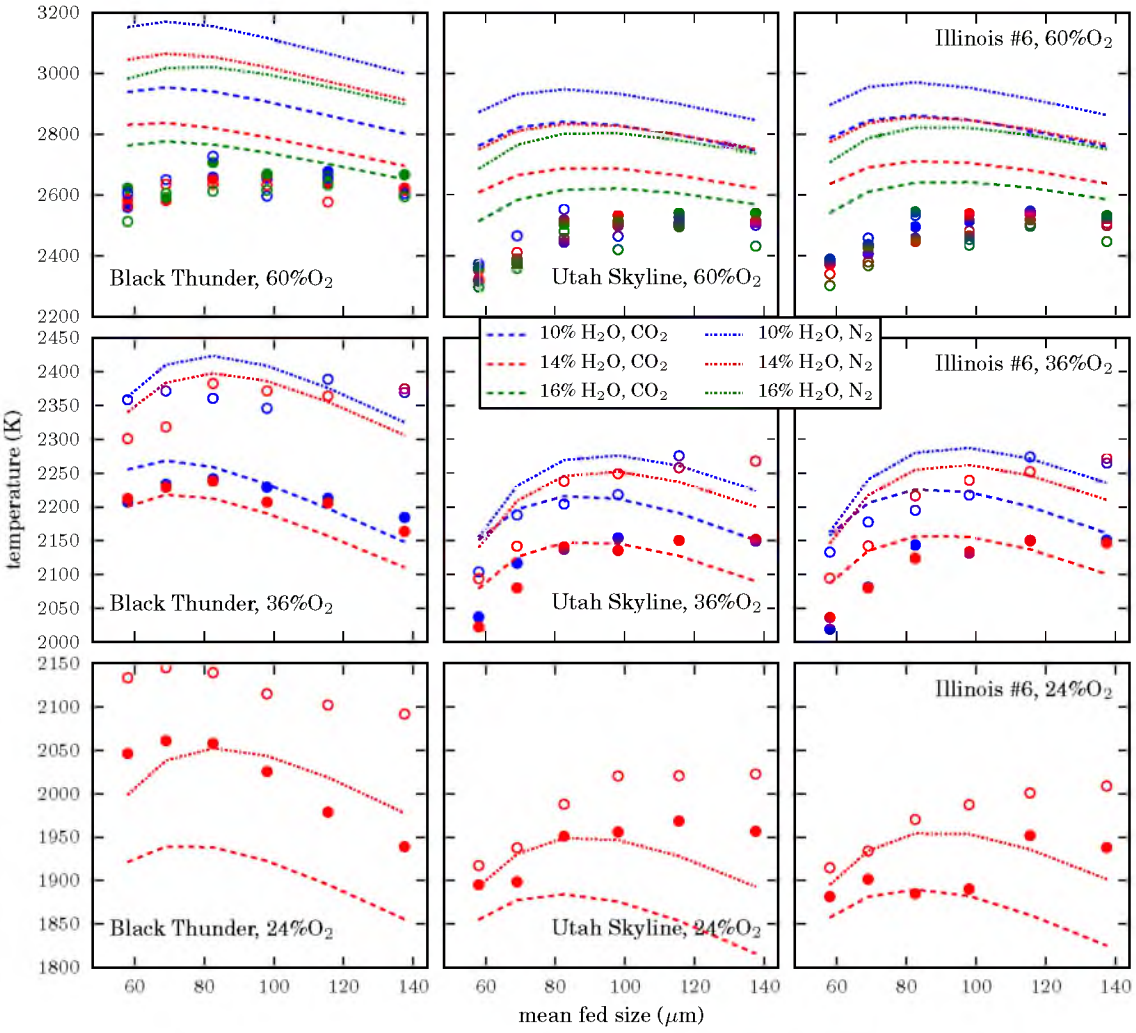


**Figure 6.11**. Simulated and experimentally measured char temperatures as a function of fed char diameter. Black Thunder char kinetics are given in Table 6.2, while bituminous char kinetics (both Utah Skyline and Illinois #6) are given in Table 6.3. Simulations are shown by the lines, while the data of Fig. 6.4 are plotted as the symbols for comparison. Symbol styles and colors are the same as Fig. 6.4.

### 6.3.4 Parametric Analyses

With the kinetics in hand, comparisons can be made between the temperatures and burnout characteristics across the parameters varied in these studies. First, experimental and simulated burnout trends and temperatures for the three chars are shown in Fig. 6.12. As expected due to their ranks, the sub-bituminous Black Thunder char reacts at the highest temperatures and burns out in the shortest residence time. With the same kinetic parameters, the simulated temperatures and burnout characteristics of the Utah Skyline and

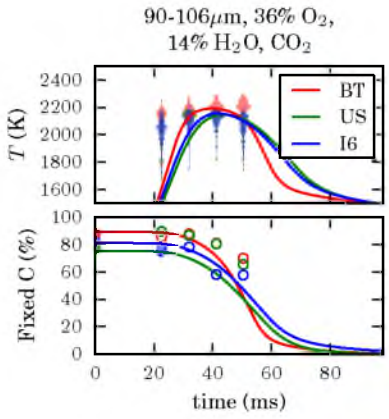


**Figure 6.12**. Temperature and burnout characteristics of the three chars used in this study. Symbols/density plots are experimental data, and lines are simulations. The fed size and environment were held constant at the conditions shown above the plot. BT is Black Thunder, US is Utah Skyline, and I6 is Illinois #6.

Illinois #6 chars are very similar. The chars all start with a different percentage of fixed carbon, due to different ash contents of the chars, as listed in Table 6.1. Black Thunder has the lowest (moisture free) ash content, followed by the Illinois #6, and the Utah Skyline has the highest ash content. Fairly good agreement between the experiments and simulations are shown. The particles take more time to heat up in the simulations than experimentally; this is likely due to the large uncertainty in the heat capacity of the chars, and the fixed value of this parameter. There is evidence that the heat capacity is a function of char type, temperature and ash content [91, 92], which is not taken into consideration in this analysis. Also, as will be discussed later, the size of the particle has an impact on both the time required to heat up, and the length of time the particles react. These simulations are only for the mean fed particle size, but by modeling both the smallest sized particles in the bin and the largest, the times the particles are at the high temperatures would shift to both longer and shoter residence times. As discussed earlier, there is large uncertainty in the burnout measurements, making comparisons to the model challenging.

Figure 6.13 shows the temperature and burnout results for two chars where the only parameter varied was the oxygen concentration in the bulk gas. Both of the chars react at the highest temperature and burnout in the shortest time with the highest oxygen concentration in the bulk gas. The increased concentration of oxygen in the bulk gas causes a larger flux of oxygen to the particle surface, and higher oxidation rates. The oxidation reactions release heat, causing high particle temperatures. High temperatures cause the gasification reactions to proceed at faster rates (in addition to the oxidation rate), consuming

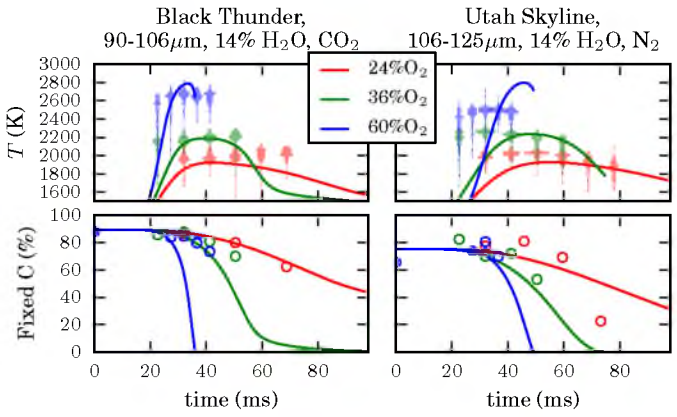


**Figure 6.13**. Temperature and burnout characteristics of two chars used while holding all but the oxygen concentration constant. Symbols/density plots are experimental data, and lines are simulations.

carbon at a higher rate and reducing the time required for burnout. Longer burnout times are shown both experimentally and in the simulations, as the oxygen concentration in the bulk gas decreases.

For two chars, simulated and experimental temperature and burnout measurements are shown for two size bins while all other parameters are held constant in Fig. 6.14. Both the experimental measurements and the simulations show only a small effect of size on the peak temperatures reached. There is some dependence of temperature on size, as shown by the slopes in Fig. 6.11, but within a size bin, with a maximum variation in size of 25 $\mu$m, the effect on temperature is fairly minimal. However, even over the variation in initial particle sizes simulated here (around 16 $\mu$m), the smaller particles heat up significantly faster,

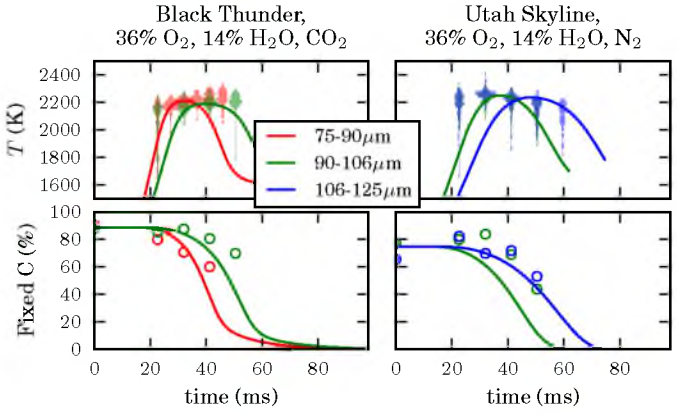


**Figure 6.14**. Temperature and burnout characteristics of two chars used while holding all but the fed particle size constant. Symbols/density plots are experimental data, and lines are simulations.

and the larger particles sustain the high temperatures for longer, which would account for the larger spread in time of the experimentally measured high temperatures than is predicted by the simulations. The experimental range in fed size also accounts for the greater spread in the measured particle temperatures towards the edges of the hot zone. Towards the beginning of the high temperature reaction zone, the larger particles are still heating up, and at the longer residence times, the smaller particles are already cooling. Detection of the cooler particles on the tail edge is somewhat suppressed due to a bias in the experimentally measured temperature to trigger off of larger particles. As expected, larger particles have a longer burnout time, as there is more mass to consume. This trend is observed experimentally and predicted by the simulations.

Effect of the diluent on the combustion characteristics is shown in Fig. 6.15. The substitution of $CO_2$ for nitrogen suppresses the heat-up of the particle, reaction temperature, and delays burnout. As discussed in Chapter 3, this effect is partially attributed to the lower rate of diffusion of oxygen through $CO_2$ as compared to $N_2$, and partially attributed to the endothermic $CO_2$ gasification reaction. Both effects must be considered to properly model char combustion in both air-fired and oxy-fired conditions. The level of agreement in both predicted char temperatures and burnout characteristics between the model and simulations is quite good for the six conditions shown in this figure. At both higher and lower oxygen concentrations, there is more disagreement between the model and experiments with the kinetic parameters used in this analysis, as can be seen in Figs. 6.11 and 6.13.

Finally, Fig. 6.16 shows the effect of the steam concentration in the bulk gas on the temperature and burnout characteristics. While there was too much scatter experimentally, the simulations can provide insight into the effects of $H_2O$ concentration. In Chapter 3, the

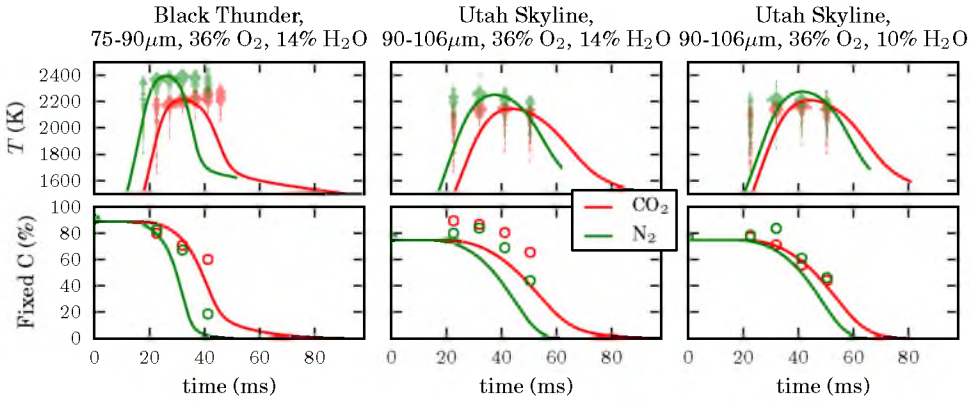


**Figure 6.15**. Temperature and burnout characteristics while holding all but the diluent constant. Symbols/density plots are experimental data, and lines are simulations.

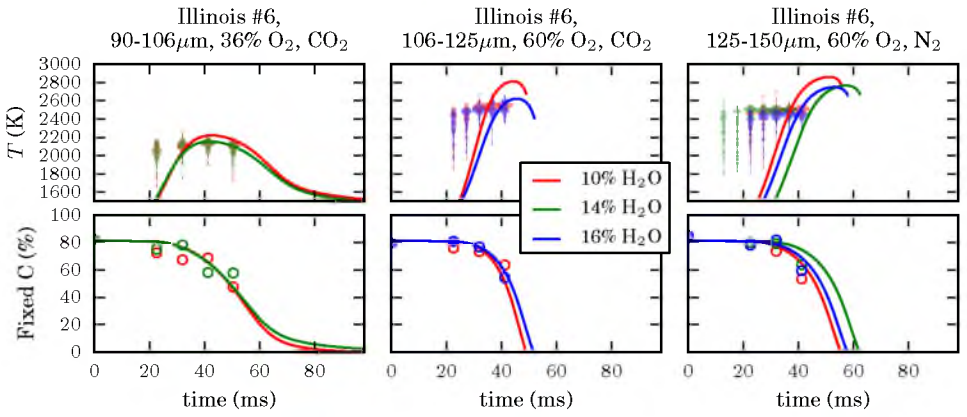


**Figure 6.16**. Temperature and burnout characteristics while holding all but the bulk steam concentration constant. Symbols/density plots are experimental data, and lines are simulations.

differences between wet recycle (25% $O_2$ in the bulk gas) and dry recycle (14% $O_2$ in the bulk gas) conditions were simulated. The predicted particle temperature and combustion rate were both slightly higher when the steam concentration was increased. With the unrealistically high steam gasification rates found in these kinetic fits, however, the opposite trend is observed. Increasing the concentration of steam in the bulk gas suppresses the particle temperatures and lengthens the burnout time. In the $CO_2$ diluent, increasing the steam concentration decreases the $CO_2$ concentration, so the effect is to substitute one gasification reaction for the other. The diffusion rate of $O_2$ through $H_2O$ is significantly higher than the diffusion of $O_2$ through $CO_2$, as shown in Fig. 1.2, which could increase the oxidation reaction under wet-recycle oxy-combustion conditions. With $N_2$ as a diluent, there are also competing effects of the improved diffusion of oxygen through steam, and the increased steam gasification rate. In the experimental photographs, the burnout time appeared to decrease slightly as the steam concentration increased, contrary to what this kinetic analysis is predicting. Improved kinetic fits to the data could change this trend.

## 6.4 Conclusions

Coals from the Illinois #6 seam, Utah Skyline, and Black Thunder mines were devolatilized to form chars. These chars were sieved into six narrow size bins, and fed into Sanda's optical entrained flow reactor. Twelve gaseous environments were chosen for study, spanning a wide range of conditions, from 24-60 vol-% $O_2$, 10-16 vol-% $H_2O$, with $CO_2$

and $N_2$ diluents. In all environments, the sub-bituminous PRB char burns at the highest temperature, with 80 $\mu$m particles burning at the highest temperature. Both bituminous chars increase in combustion temperature up to the largest mean fed char size of 140 $\mu$m. The substitution of $CO_2$ for $N_2$ lowers the combustion temperature in the 24 and 36 vol-%$O_2$ environments, due to the lower diffusivity of oxygen through $CO_2$ as compared to $N_2$, and the effect of the $CO_2$ gasification reaction. At 60 vol-%$O_2$, there was no discernible influence of combustion environment on combustion temperature, which may by a sign of improved kinetic control under highly oxygen-enriched combustion conditions. In all cases, there was no meaningful influence of steam concentration on temperature. Qualitative photos suggest that burnout occurs in less time as the steam concentration is increased, which could indicate that a higher steam concentration and the improved diffusion of oxygen through steam causes both exothermic oxidation reactions and endothermic steam gasification reactions to proceed at faster rates, but have little effect on temperature.

Burnout measurements on the chars had a large degree of uncertainty, due to experimental errors. Nonetheless, faster burnout occurred as the oxygen concentration increased, and for the Black Thunder char over the two bituminous chars. The steam concentration also showed little effect on the experimentally measured burnout characteristics. An initial heat-up time of around 25-30 ms for the chars was apparent in the burnout measurements (as well as the optical measurements).

Measured surface areas of the initial chars were negligible, probably due to plasticization of the char sealing the surface during devolatilization. At early reaction times, significant surface area developed, up to 500 $m^2/g$ for the Black thunder char, and nearly 400 $m^2/g$ for the bituminous chars. This surface area rapidly decreased, however, as burnout progressed. SEM images of the chars and partially reacted chars confirmed the lack of porosity initially, and significant porosity for the collected chars.

A transient burnout model was used to simulate the chars reacting in the EFR. Kinetic fits to the temperature data were found. An initial computer optimization generated kinetic fits that predicted low particle temperatures for the bituminous chars. Several iterations of a hand fit yielded better results for the bituminous char temperatures. The computer optimization must have discovered a local minimum rather than a global minimum. Due to the similarities in temperatures for the bituminous chars, only one set of kinetic parameters was generated for both the Utah Skyline and Illinois #6 chars. Both the activation energies and pre-exponentials determined for the oxidation and steam gasification reactions were much lower for the bituminous char than those parameters for the sub-bituminous char.

The activation energy for the $CO_2$ gasification reaction was similar for both the bituminous and sub-bituminous chars, but the pre-exponential to the $CO_2$ gasification reaction was much lower for the bituminous char than the pre-exponential for the sub-bituminous char.

Simulated temperatures showed similar characteristics as the measured temperatures. There was a peak temperature for the Black Thunder char around 80 $\mu$m that is shifted to a slightly higher particle size for the bituminous chars. The bituminous chars also react at lower temperatures than the sub-bituminous char, and each of the chars react at higher temperatures in the $N_2$ diluent as compared to $CO_2$. The simulations do show a temperature dependence on steam concentration that was not discernible experimentally. The temperature is predicted to decrease as the steam concentration increases, possibly due to the effect of the steam gasification reaction.

Finally, simulations were run holding all but one parameter constant. As the char was varied, the Black Thunder reacted at higher temperature and burned out in less time than the two bituminous chars, which had similar characteristics. The reaction temperatures increased and burnout times decreased as the oxygen concentration increased. Heat-up and burnout time were shorter for smaller chars, while peak temperature was not affected greatly by fed particle size. Char particles react at higher temperatures and have shorter burnout times when $N_2$ is the diluent than when $CO_2$ is the diluent. The reaction temperature and burnout times decrease as the steam concentration increases.

A transient model for char reaction provides insight into the combustion processes. The kinetic parameters and model described in this analysis can be used as a submodel in a CFD code to predict the combustion behavior of these coal chars over a wide range of environments. This is useful for designing new-build oxy-combustion boilers, or in retrofitting conventional boilers for oxy-combustion. These insights can also aid in burner design (such as oxygen concentrations desired in the primary and secondary "air" feeds, and the use of oxygen lances), recycle considerations (whether to dry the recycle gas), and even which fuel to use (or the design requirements for a given fuel). The insight into burnout characteristics can help size boilers, or determine solutions to tune the burnout characteristics to their desired values.

# CHAPTER 7

# CONCLUSIONS

During oxy-combustion, nitrogen is separated from oxygen before the introduction of oxygen and fuel into a coal boiler. Often, recycled flue gas dilutes the oxygen to moderate combustion temperatures and prevent excessive slagging. The mixture of oxygen and recycled flue-gas (consisting of mostly $CO_2$ and some moisture) reacts with the pulverized coal, and the effluent is a highly concentrated stream of $CO_2$. This $CO_2$ can be captured through condensation, and then utilized or stored, preventing the climate changing impacts of this greenhouse gas. Although oxy-combustion has been considered and studied for over a decade, there are still misunderstood aspects of the science.

During air-fired combustion, where 80% of the bulk gas is $N_2$, and the concentrations of $CO_2$ and $H_2O$ in the bulk gas are low, the gasification reactions are often neglected. However, these reactions have the potential to impact the combustion characteristics during oxy-combustion where higher concentrations of $CO_2$ and potentially higher concentrations of $H_2O$ exist in the bulk gas, depending on the extent to which the flue-gas is dried before recycle. In addition, the transport and heat transfer properties of $N_2$, $CO_2$, and $H_2O$ are different, which also affects the combustion characteristics. Modeling and experimental studies of the oxy-combustion behavior of pulverized coal chars are detailed in this work to elucidate differences, and provide insight into the processes occurring.

Chapter 2 describes a detailed model of a single porous char particle, known as SKIPPY. This model includes a mathematical description of gas-phase transport, porous-media transport, homogeneous gas-phase reactions, and heterogeneous gas-solid reactions. The particle is assumed to be spherical, at steady-state in a quiescent atmosphere. The porous particle and boundary layer are discretized, and the thermal energy balance and species continuity equations are solved to find the temperatures and species concentrations throughout the particle and boundary layer.

In Chapter 3, the SKIPPY code is employed to asses the impact of $CO_2$ and steam gasification reactions on the oxy-combustion of coal chars. A literature review guided the determination of the relative rates of gasification reactions to oxidation. The detailed model indicates that for a 100 $\mu$m char particle, gasification reactions reduce the predicted char particle temperature significantly (because of the reaction endothermicity). Lower temperatures reduce the radiant emission and rate of char oxidation, but the char carbon consumption rate actually increases by approximately 10%, since the gasification reactions are consuming carbon (in addition to the oxidation reaction). In highly oxygen enriched environments, the gasification reactions have a greater influence on char combustion, due to the high char combustion temperatures in these environments. Gasification reactions account for about 20% of the carbon consumption in low oxygen conditions, and about 30% of the carbon consumption under oxygen enriched conditions. The gasification reactions are also found to influence the carbon consumption rate and particle temperatures during air-blown combustion conditions, despite the lower concentration of gasification agents in the bulk gas.

While SKIPPY provides an accurate description of coal char combustion, inclusion of the detailed description of gas-phase kinetics is too complex for use in a CFD simulation of a pulverized coal boiler. Chapter 4 describes some common assumptions that are made during pulverized coal char combustion modeling and the errors associated with those assumptions are evaluated. Two simplified models are presented: a single-film model, wherein no gas-phase reactions occur, and a double-film model, where gas phase reactions converting the CO (generated by the carbon-oxygen and carbon-$CO_2$ reactions) to $CO_2$ and $H_2$ (generated from the steam gasification reaction) to $H_2O$ occur at a single-point in the otherwise reaction-free boundary layer. The single-film model is found to yield temperatures and carbon consumption rates that are closer to those predicted by SKIPPY. It is estimated that temperature predictions from the single-film model will be accurate to within 270 K, and carbon consumption rate predictions should be accurate to within 16%, for typical char particles reacting in environments from 12-60% $O_2$, in both $CO_2$ and $N_2$ diluents. A description of reactant penetration into the porous char particle in the single-film model yields more accurate results, but using apparent kinetics changes the predicted temperatures by no more than 55 K, and the carbon consumption rate by less than 22%.

Chapter 5 introduces and describes experiments intended to measure the parameters required for the single-film model. These include kinetic rate parameters for oxidation as well as steam and $CO_2$ gasification reactions. Chars were generated, and then reacted

in an entrained flow reactor with oxygen concentrations ranging from 24-60%, steam concentrations from 10-16%, and $N_2$ and $CO_2$ diluents. High oxygen concentrations were chosen to increase particle temperatures (from the exothermic oxidation reactions) and overcome the high activation energy barriers for the gasification reactions. Temperatures of individual particles were measured, and surface area and burnout measurements were made on collected chars.

Finally, in Chapter 6, the results of the experiments and kinetic fits of the single-film model are presented and discussed. There were three chars considered in this work: Black Thunder, which is sub-bituminous, Utah Skyline, and Illinois #6, both of which are bituminous. Each of the chars reacts at higher temperatures in higher oxygen concentrations, and burns out more rapidly. In a given environment, the Black Thunder char reacts at a higher temperature and burns faster than either of the other chars, and the two bituminous chars react at very similar temperatures. The micropore surface area of the Black Thunder char is also slightly higher than the bituminous char surface areas, at short residence times. The micropore surface area for all of the chars decreases rapidly as burnout progresses. The activation energy and pre-exponential factors for the oxidation and steam gasification reactions are determined to be higher for the Black Thunder char as compared to the bituminous chars. The activation energy for the $CO_2$ gasification reaction is similar for all of the chars, while the pre-exponential factor is lower for the bituminous chars than the sub-bituminous char. The simplified model effectively captures the experimentally observed trends, such as a higher temperature for the sub-bituminous char, the size dependence on peak temperature reached, and the differences between $CO_2$ and $N_2$ diluent atmospheres. The model does, however predict that a higher concentration of steam suppresses the reaction temperature and requires a longer time for burnout, a trend that was not observed experimentally.

An improved understanding of pulverized coal char combustion is realized through this work. During both conventional and oxy-combustion, the gasification reactions suppress the reaction temperatures, but consume carbon, having a minor impact on the carbon consumption rate. Especially in oxy-combustion environments, where the concentration of $CO_2$ is high in the bulk gas, gasification reactions must be incorporated into a combustion model so that accurate predictions of temperature and burning rates can be made. Accurate high temperature gasification rate data is still needed to improve oxy-combustion models. A single-film model is able to predict char particle burning rates and temperatures with reasonable accuracy. Using apparent kinetics (ignoring intraparticle diffusion), is also a

reasonable assumption in modeling char combustion.

The kinetic parameters found in this study for the Black Thunder, Utah Skyline, and Illinois #6 coal chars can be used in further modeling studies. A single-film model that considers oxidation and gasification kinetics would work well as a CFD submodel, and these kinetics can be used to predict the performance of these project coals in conventional and oxy-combustion environments. This information can be used to retrofit existing air-fired coal combustion boilers for oxy-combustion, or design new oxy-combustion boilers. Novel concepts for oxy-combustion burners and the use of pure oxygen lances can be considered, as these kinetics are valid in environments with up to 60% $O_2$ (and potentially beyond).

Oxy-combustion of pulverized coal with $CO_2$ capture has the potential to dramatically reduce the impact the energy generation sector is having on the environment. The improved understanding of the oxy-combustion process, how to model it, and data for three chars presented in this work will hopefully aid in the adoption and development of this technology.

# REFERENCES


[1] E. R. Caley, J. F. C. Richards, Theophrastus on stones: Introduction, Greek text, English translation, and commentary, The Ohio State University Press, 1956.

[2] Secure & reliable energy supplies - history of U.S. coal use, Accessed Feb. 2012. http://www.netl.doe.gov/keyissues/historyofcoaluse.html.

[3] 2010 Survey of Energy Resources, Technical Report, World Energy Council, 2010. http://www.worldenergy.org/documents/ser_2010_report_1.pdf.

[4] Key World Energy Statistics, Technical Report, International Energy Agency, 2011. http://www.iea.org/textbase/nppdf/free/2011/key_world_energy_stats.pdf.

[5] B. J. P. Buhre, L. K. Elliott, C. D. Sheng, R. P. Gupta, T. F. Wall, Prog. Energy Combust. Sci. 31 (2005) 283–307.

[6] L. Chen, S. Z. Yong, A. F. Ghoniem, Prog. Energy Combust. Sci. 38 (2012) 156–214.

[7] J. Hong, R. Field, M. Gazzino, A. F. Ghoniem, Energy 35 (2010) 5391–5399.

[8] C. R. Shaddix, A. Molina, Proc. Combust. Inst. 32 (2009) 2091–2098.

[9] I. W. Smith, Proc. Combust. Inst. 19 (1982) 1045–1065.

[10] R. Hurt, J.-K. Sun, M. Lunden, Combustion and Flame 113 (1998) 181–197.

[11] R. Hurt, R. Mitchell, Proc. Combust. Inst. 24 (1992) 1233 – 1241.

[12] R. E. Mitchell, Proc. Combust. Inst. 28 (2000) 2261 – 2270.

[13] J. J. Murphy, C. R. Shaddix, Combust. Flame 144 (2006) 710–729.

[14] P. Heil, D. Toporov, H. Stadler, S. Tschunko, M. Förster, R. Kneer, Fuel 88 (2009) 1269–1274.

[15] R. K. Rathnam, L. K. Elliott, T. F. Wall, Y. Liu, B. Moghtaderi, Fuel Process. Technol. 90 (2009) 797–802.

[16] D. Toporov, P. Bocian, P. Heil, A. Kellermann, H. Stadler, S. Tschunko, M. Förster, R. Kneer, Combust. Flame 155 (2008) 605–618.

[17] E. S. Hecht, C. R. Shaddix, A. Molina, B. S. Haynes, Proc. Combust. Inst. 33 (2011) 1699–1706.

[18] C. R. Shaddix, A. Molina, Proceedings of the 34th International Technical Conference on Coal Utilization and Fuel Systems.

[19] M. B. Toftegaard, J. Brix, P. A. Jensen, P. Glarborg, A. D. Jensen, Prog. Energy Combust. Sci. 36 (2010) 581–625.

[20] C. R. Shaddix, A. Molina, Oxy-fuel combustion for power generation and carbon dioxide ($CO_2$) capture, Woodhead Publishing, 2011, pp. 101–124.

[21] A. Molina, C. R. Shaddix, Proc. Combust. Inst. 31 (2007) 1905–1912.

[22] Y. Liu, M. Geier, A. Molina, C. R. Shaddix, Int. J. Greenh. Gas Con. 5, Supplement 1 (2011) S36–S46.

[23] T. Kiga, S. Takano, N. Kimura, K. Omata, M. Okawa, T. Mori, M. Kato, Energy Convers. Manage. 38, Supplement (1997) S129 – S134.

[24] S. R. Dhaneswar, S. V. Pisupati, Fuel Processing Technology 102 (2012) 156–165.

[25] S. Hu, D. Zeng, A. N. Sayre, H. Sarv, in: 2011 International Pittsburgh Coal Conference, Pittsburgh, PA.

[26] J. Brix, P. A. Jensen, A. D. Jensen, Fuel 89 (2010) 3373–3380.

[27] D. L. Marchisio, R. O. Fox, J. Aerosol Sci. 36 (2005) 43 – 73.

[28] E. S. Hecht, C. R. Shaddix, M. Geier, A. Molina, B. S. Haynes, Combust. Flame 159 (2012) 3437 – 3447.

[29] R. J. Kee, J. A. Miller, M. D. Smooke, J. F. Grcar, A FORTRAN program for modeling steady laminar one-dimensional premixed flames, Report No. SAND85-8240, Sandia National Laboratories, Livermore, CA, 1985.

[30] R. J. Kee, F. M. Rupley, J. A. Miller, CHEMKIN-II: A FORTRAN Chemical Kinetics Package for the Analysis of Gas-Phase Chemical Kinetics, Report No. SAND89-8009, Sandia National Laboratories, Livermore, CA, 1989.

[31] M. E. Coltrin, R. J. Kee, F. M. Rupley, Surface CHEMKIN (version 3.7) : a FORTRAN package for analyzing heterogeneous chemical kinetics at a solid surface - gas phase interface, Report No. SAND90-8003, Sandia National Laboratories, Livermore, CA, 1990.

[32] R. J. Kee, G. Dixon-Lewis, J. Warnatz, M. E. Coltrin, J. A. Miller, A FORTRAN computer code package for the evaluation of gas-phase multicomponent transport properties., Report No. SAND86-8246, Sandia National Laboratories, Livermore, CA, 1986.

[33] J. F. Grcar, The TWOPNT Program for Boundary Value Problems, Report No. SAND91-8230, Sandia National Laboratories, Livermore, CA, 1992.

[34] Eia - 2010 international energy outlook - coal, 2011. `http://www.eia.doe.gov/oiaf/ieo/coal.html`. Accessed May 2011.

[35] Eia - 2010 international energy outlook - energy-related carbon dioxide emissions, 2011. `http://www.eia.doe.gov/oiaf/ieo/emissions.html`. Accessed May 2011.

[36] Y. Tan, Oxy-fuel combustion for power generation and carbon dioxide ($CO_2$) capture, Woodhead Publishing, 2011, pp. 35–53.

[37] N. M. Laurendeau, Prog. Energy Combust. Sci. 4 (1978) 221–270.

[38] G.-S. Liu, S. Niksa, Prog. Energy Combust. Sci. 30 (2004) 679–717.

[39] M. F. Irfan, M. R. Usman, K. Kusakabe, Energy 36 (2011) 12–40.

[40] P. L. Walker Jr., F. Rusinko Jr., L. G. Austin, volume 11 of *Advances in Catalysis*, Academic Press, 1959, pp. 133–221.

[41] R. C. Everson, H. W. J. P. Neomagus, H. Kasaini, D. Njapha, Fuel 85 (2006) 1076–1082.

[42] Z. H. Zhu, J. Finnerty, G. Q. Lu, M. A. Wilson, R. T. Yang, Energy Fuels 16 (2002) 847–854.

[43] L. R. Radovic, K. Steczko, P. L. Walker Jr., R. G. Jenkins, P. L. W. Jr., Fuel Process. Technol. 10 (1985) 311–326.

[44] G. J. Goetz, N. Y. Nsakala, R. L. Patel, T. C. Lao, Combustion and Gasification Characteristics of Four Commercially Significant Coals of Different Rank, Report No. AP-261, EPRI, 1982.

[45] E. Hampartsoumian, P. L. Murdoch, M. Pourkashanian, D. T. Trangmar, A. Williams, Combust. Sci. Technol. 92 (1993) 105–121.

[46] W. F. DeGroot, G. N. Richards, Carbon 27 (1989) 247–252.

[47] D. J. Harris, I. W. Smith, Proc. Combust. Inst. 23 (1990) 1185–1190.

[48] D. G. Roberts, D. J. Harris, Energy Fuels 14 (2000) 483–489.

[49] M. D. Mann, R. Z. Knutson, J. Erjavec, J. P. Jacobsen, Fuel 83 (2004) 1643–1650.

[50] H. Liu, H. Zhu, M. Kaneko, S. Kato, T. Kojima, Energy Fuels 24 (2010) 68–75.

[51] R. Kee, M. Coltrin, P. Glarborg, Chemically Reacting Flow: Theory and Practice, John Wiley & Sons, 2003.

[52] G. P. Smith, S. D. Golden, M. Frenklach, N. W. Moriarty, B. Eitener, M. Goldenberg, C. T. Bowman, R. K. Hanson, S. Song, W. C. Gardiner, V. V. Lissianski, Z. Qin, GRI-MECH 3.0, 2001. `http://www.me.berkeley.edu/gri_mech`. Accessed Dec. 2010.

[53] A. Molina, A. F. Sarofim, W. Ren, J. Lu, G. Yue, J. M. Beér, B. S. Haynes, Combust. Sci. Technol. 174 (2002) 43–71.

[54] A. Molina, J. J. Murphy, F. Winter, B. S. Haynes, L. G. Blevins, C. R. Shaddix, Combust. Flame 156 (2009) 574–587.

[55] D. A. Aderibigbe, J. Szekely, Carbon 17 (1979) 431–433.

[56] M. Geier, C. R. Shaddix, K. A. Davis, H.-S. Shim, Applied Energy 93 (2012) 675 – 679.

[57] A. Molina, F. Mondragón, Fuel 77 (1998) 1831–1839.

[58] L. R. Radovic, P. L. Walker Jr., R. G. Jenkins, Fuel 62 (1983) 849 – 856.

[59] R. H. Hurt, A. F. Sarofim, J. P. Longwell, Fuel 70 (1991) 1079–1082.

[60] R. H. Hurt, A. F. Sarofim, J. P. Longwell, Energy Fuels 5 (1991) 290–299.

[61] I. Aarna, E. M. Suuberg, Proc. Combust. Inst. 27 (1998) 2933 – 2939.

[62] C. Brown, Unpublished data, 2003.

[63] R. J. Quann, A. F. Sarofim, Proc. Combust. Inst. 19 (1982) 1429–1440.

[64] A. Williams, R. Backreedy, R. Habib, J. Jones, M. Pourkashanian, Fuel 81 (2002) 605 – 618.

[65] E. Korytnyi, R. Saveliev, M. Perelman, B. Chudnovsky, E. Bar-Ziv, Fuel 88 (2009) 9 – 18.

[66] R. Barranco, A. Rojas, J. Barraza, E. Lester, Fuel 88 (2009) 2335 – 2339.

[67] L. Álvarez, M. Gharebaghi, M. Pourkashanian, A. Williams, J. Riaza, C. Pevida, J. Pis, F. Rubiera, Fuel Process. Technol. 92 (2011) 1489 – 1497.

[68] M. M. Baum, P. J. Street, Combust. Sci. Technol. 3 (1971) 231–243.

[69] C. Gonzalo-Tirado, S. Jiménez, J. Ballester, Combustion and Flame 159 (2012) 385–395.

[70] J. R. Arthur, Trans. Faraday Soc. 47 (1951) 164–178.

[71] L. Tognotti, J. P. Longwell, A. F. Sarofim, Proc. Combust. Inst. 23 (1991) 1207–1213.

[72] M. Geier, C. Shaddix, F. Holzleithner, Proc. Combust. Inst. 34 (2013) 2411–2418.

[73] M. Zhang, J. Yu, X. Xu, Combust. Flame 143 (2005) 150 – 158.

[74] J. Yu, M. C. Zhang, Energy Fuels 23 (2009) 2874–2885.

[75] J. Yu, M. C. Zhang, J. Zhang, Steel Res. Int. 80 (2009) 717–726.

[76] J. Zhang, M. Zhang, J. Yu, Energy Fuels 24 (2010) 871–879.

[77] E. W. Thiele, Ind. Eng. Chem. 31 (1939) 916–920.

[78] E. Jones, T. Oliphant, P. Peterson, et al., SciPy: Open source scientific tools for Python, 2001–. `http://www.scipy.org/`.

[79] J. J. Murphy, C. R. Shaddix, Combust. Flame 157 (2010) 535–539.

[80] R. Aris, Chem. Eng. Sci. 6 (1957) 262–268.

[81] R. Aris, Chem. Eng. Sci. 7 (1957) 8–14.

[82] M. Gil, J. Riaza, L. Álvarez, C. Pevida, J. Pis, F. Rubiera, Applied Energy 91 (2012) 67–74.

[83] ASTM, Standard Test Methods for Proximate Analysis of Coal and Coke by Macro Thermogravimetric Analysis, Technical Report D7582-10, 2010.

[84] S. Brunauer, P. H. Emmett, E. Teller, J. Am. Chem. Soc. 60 (1938) 309–319.

[85] H. Stoeckli, J. Houriet, Carbon 14 (1976) 253–256.

[86] H. Marsh, T. Siemieniewska, Fuel, Lond. 44 (1965) 355–367.

[87] A. F. Sarofim, J. S. Lighty, P. J. Smith, K. J. Whitty, E. Eyring, A. Sahir, M. Alvarez, M. Hradisky, C. Clayton, G. Konya, R. Baracki, K. Kelly, Chemical Looping Combustion Reactions and Systems Task 5 Topical Report, Utah Clean Coal Program, Technical Report Task 5 Topical Report, Utah Clean Coal Program, University of Utah, Salt Lake City, UT, 2011.

[88] R. E. Mitchell, R. Hurt, L. Baxter, D. Hardesty, Compilation of Sandia Coal Char Combustion Data and Kinetic Analyses, Technical Report, 1992.

[89] R. Hilpert, Forschung auf dem Gebiete des Ingenieurwesens 4 (1933) 215–224.

[90] D. Anthony, J. Howard, AIChE Journal 22 (2004) 625–656.

[91] F. Hanrot, D. Ablitzer, J. Houzelot, M. Dirand, Fuel 73 (1994) 305 – 309.

[92] J. Tomeczek, H. Palugniok, Fuel 75 (1996) 1089 – 1093.